2022-04-07

Time-lapse VSP monitoring of CO2 sequestration at the CaMI Field Research Station

Kolkman-Quinn, Brendan James

UNIVERSITY OF CALGARY

Time-lapse VSP monitoring of CO_2 sequestration at the CaMI Field Research Station

by

Brendan James Kolkman-Quinn

A THESIS

SUBMITTED TO THE FACULTY OF GRADUATE STUDIES

IN PARTIAL FULFILMENT OF THE REQUIREMENTS FOR THE

DEGREE OF MASTER OF SCIENCE

GRADUATE PROGRAM IN GEOLOGY AND GEOPHYSICS

CALGARY, ALBERTA

APRIL, 2022

ABSTRACT

The Containment and Monitoring Institute Field Research Station (CaMI.FRS) is a carbon sequestration field experiment near Brooks, Alberta. CO_2 is injected into a saline aquifer in the 6 m thick, 10% porosity Basal Belly River Sandstone at 300 m depth. This CO_2 plume simulates a shallow leak scenario from an industrial scale CO_2 storage reservoir. Vertical Seismic Profiles (VSP) were collected between 2017 and 2021 to determine a detection threshold and delineate the plume. These data had high repeatability, with permanent borehole sensors and identical source coordinates. Seasonal variations in surface and near-surface conditions were the main source of dissimilarity between baseline and monitor data. A time-lapse compliant processing workflow was developed for the 10 Hz – 150 Hz shallow data. This workflow produced directly comparable amplitudes between baseline and monitor data, except at higher frequency bands affected by variable near-surface filtering. Spectral differences were eliminated with high-cut filters designed for each source location. Avoiding the use of shaping filters preserved the subtle amplitude response of the CO_2 plume in the remaining bandwidth. After 33 t of injection, the CO_2 plume produced an observable time-lapse amplitude anomaly on multiple geophone datasets on two monitoring lines. The interpreted CO_2 plume matched forward modeling expectations of approximately 50 m lateral extent, but with an asymmetric distribution around the injection well. Equivalent DAS datasets possessed lower signal strength than geophone data, with instrument noise interfering with the CO_2 amplitude response. A weak seismic anomaly was observed on only one DAS monitoring line. The high-confidence geophone results establish a leak detection threshold at 33 t of CO_2 for this geological setting. The ability to detect a 33 t CO_2 plume with VSP field data lends confidence to Measurement, Monitoring, and Verification capabilities at industrial operations with injection rates of kilotonnes or megatonnes per year. The time-lapse compliant VSP workflow will help inform shallow monitoring procedures, while the CO_2 delineation will contribute to future multi-disciplinary studies at CaMI.FRS.

ACKNOWLEDGEMENTS

My sincere thanks to my thesis supervisor Don Lawton, director of CaMI. Don's vision and hard work have created a frontier CCS research operation at CaMI.FRS which is generating valuable research outcomes and expertise. I also thank Kris Innanen, director of CREWES, for his work in directing a world-class seismic research organization that provides so many research opportunities for students such as myself.

Thank you to Daniel Trad for offering me rewarding teaching opportunities throughout my degree. These were a source of balance and enriched my experience, making me both a better teacher and a better geophysicist.

Thank you to friends and colleagues in CREWES, CaMI, and Geovectra for their hard work operating the Field Research Station, acquiring geophysical data, and for sharing their expertise and experience: Greg Maidment, Franki Race, Kirk Osadetz, Kevin Hall, Kevin Bertram, Malcolm Bertram, Yichuan Wang, Jorge Monsegny-Parra, Ninoska Amundaray Nieto, Matt Eaid, Scott Keating, Mike Hall, and Mingyu Zhang.

A special thanks goes to Marie Macquet, manager of Subsurface Research and Project Delivery at CaMI. Marie's dedication and broad expertise was an inspiration. Her willingness to collaborate and to bounce ideas off each other provided a much-appreciated sense of teamwork and collegial atmosphere during an era of remote-work.

Finally, I would like to thank the sponsors of CREWES and CaMI for their continued support. This work was funded by CREWES industrial sponsors and NSERC (Natural Science and Engineering Research Council of Canada) through the grant CRDPJ 543578-19. The data were acquired through a collaboration with the Containment and Monitoring Institute (CaMI) of Carbon Management Canada (CMC). Research at the CaMI field site is supported by the Canada First Research Excellence Fund, through the Global Research Initiative at the University of Calgary.

TABLE OF CONTENTS

LIST OF TABLES

LIST OF FIGURES

LIST OF SYMBOLS, ABBREVIATIONS AND NOMENCLATURE

1-C	One component
3-C	Three component
3D	Three dimensional
AVO	Amplitude variation with offset
BBRS	Basal Belly River Sandstone
CaMI	Containment and Monitoring Institute
CCS	Carbon Capture and Storage
CREWES	Consortium for Research in Elastic Wave Exploration Seismology
CO_2	Carbon Dioxide
DAS	Distributed Acoustic Sensing
EOR	Enhanced Oil Recovery
f	Frequency (Hz)
f-k	Frequency-Wavenumber
FB	First Break
FRS	Field Research Station
Hz	Hertz (s^{-1})
Inj	CO_2 Injection well
IPCC	Intergovernmental Panel on Climate Change
m	Meter
m/s	Meters per second
MMV	Measurement, Monitoring, and Verification
MD	Measured Depth
ms	Millisecond
NMO	Normal Move-Out
NRMS	Normalized Root-Mean-Square
Obs1	Geochemistry observation well
Obs2	Geophysics observation well
P-wave	Compressional seismic wave
RMS	Root-Mean-Square
S-wave	Shear seismic wave
SNR	Signal-to-Noise Ratio

t	time
-tt	Minus first break times
+tt	Plus first break times (equivalent to two-way travel time)
TWT	Two-way travel time
V_P	P-wave velocity
V_S	S-wave velocity
VSP	Vertical Seismic Profile

Do nothing in haste; look well to each step; and from the beginning think what may be the end.

Edward Whymper, Scrambles Among the Alps

CHAPTER 1 - INTRODUCTION

1.1 Carbon Capture and Storage

In order to meet nationally defined commitments to the COP21 Paris agreement, Canada and other countries must take a multi-pronged approach to reduce greenhouse gas emissions. Carbon Capture and Storage (CCS) is one of many essential strategies for reducing global CO_2 emissions (IPCC, 2005, 2014). In 2020, 33.3 Gt of CO_2 emissions were emitted globally (Zhu et al., 2022), while only 40 Mt of CO_2 were captured and stored by industrial CCS projects (IEA, 2021). Increasing annual storage rates to the gigatonne range will require a rapid expansion of the CCS industry (IEA, 2021). Saline aquifers in sedimentary basins represent much of the potential for geological sequestration of CO_2, if permanent storage can be assured (Bachu, 2003, IPCC, 2005). Effective geophysical monitoring of geological CO_2 sequestration provides important Measurement, Monitoring, and Verification (MMV) capabilities at a CCS site. The ability to monitor reservoir conditions and reliably detect leaks will help determine the feasibility of permanent storage of CO_2 in geologic formations on a global scale. Demonstrating the ability to detect small CO_2 leaks with geophysical field data aids reservoir monitoring by verifying the absence of CO_2 outside of the intended injection interval. Carbon Management Canada's (CMC) Containment and Monitoring Institute (CaMI) operates a CO_2 sequestration experiment in Newell County near Brooks, Alberta, in western Canada (Figure 1.1). The ongoing CO_2 injection simulates a shallow leak scenario relevant to industrial-scale CO_2 sequestration and Enhanced Oil Recovery (EOR) operations.

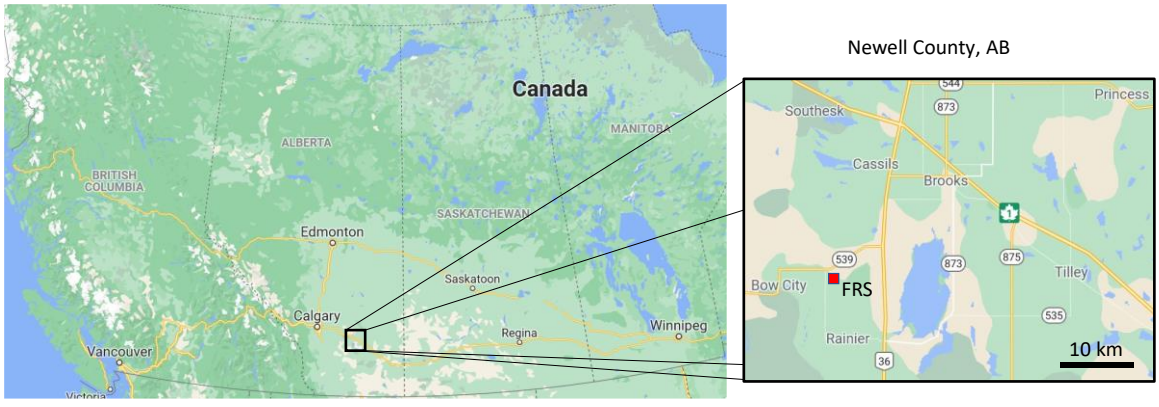

Figure 1.1 Map of western Canada showing the location of the CaMI Field Research Station (red square) in Newell County, southern Alberta. (Google Maps 2022).

1.2 CaMI Field Research Station

The Containment and Monitoring Institute Field Research Station (CaMI.FRS) is a shallow CO_2 sequestration experiment for which the primary research objective is testing MMV capabilities for geological CO_2 sequestration. Multiple geophysical and geochemical monitoring technologies are employed at the FRS, including Time-lapse Vertical Seismic Profiles (VSP). The injection interval at the FRS is the Basal Belly River Sandstone (BBRS), a brine-saturated reservoir of 10% porosity at the base of the Foremost Fm (Dongas, 2016, Macquet and Lawton, 2017). A strong positive seismic reflection is produced by the velocity and density contrasts at the interface between the BBRS and the overlying McKay member's coals and shales (Figure 1.2). This high-amplitude seismic reflection allows for easy identification of the reservoir interval in a seismic section. This marker is typically indicated as BBRS in the figures throughout this document. Fluid substitution modeling indicates that the partial saturation of injected gas-phase CO_2 in the reservoir causes a decrease in the BBRS seismic reflection amplitude (Macquet et al., 2019). This decrease in reflectivity is driven primarily by a decrease in P-wave velocity, with a lower magnitude decrease in density. This effect produces a negative amplitude anomaly in a time-lapse difference at the BBRS interval.

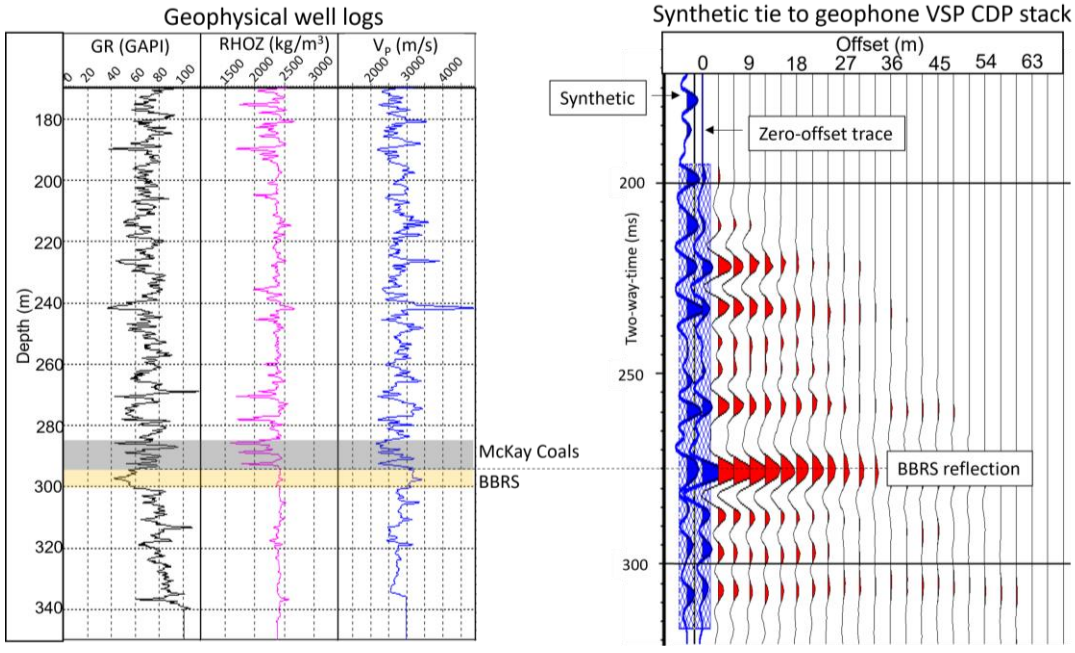

Figure 1.2 Sonic, gamma ray, and density well logs with the Basal Belly River Sandstone (BBRS) highlighted in beige, and the McKay coals and shales of the Foremost Fm highlighted in grey. On the right, a synthetic seismogram is tied to a geophone VSP CDP stacked section.

1.3 Time-lapse VSP monitoring

1.3.1 Vertical Seismic Profiles

Vertical Seismic Profiles (VSP) are a form of active seismic survey for which the seismic sensors are installed in a wellbore. At CaMI.FRS, these sensors are cemented outside the casing. This allows the recording of seismic waves within the subsurface (Figure 1.3), as opposed to placing receivers on the surface. Seismic waves experience significant amplitude and frequency attenuation in the unconsolidated, heterogenous sediments of the near-surface, compounded by seasonal variability (Al Jabri, 2011). For seismic sources on the surface, an initial pass of near-surface filtering of the downgoing seismic waves is unavoidable. This near-surface filtering is variable between baseline and monitor surveys, mainly due to seasonal effects such as water saturation and freeze-thaw cycles. These near-surface effects can be partially mitigated in VSP data, as the downgoing arrivals are recorded by the borehole sensors. By recording reflected seismic waves downhole, VSPs avoid the second pass of variable near-surface filtering for upgoing seismic reflections. This increases the repeatability of time-lapse VSP surveys for reservoir monitoring, by preserving frequency content and reducing signal loss.

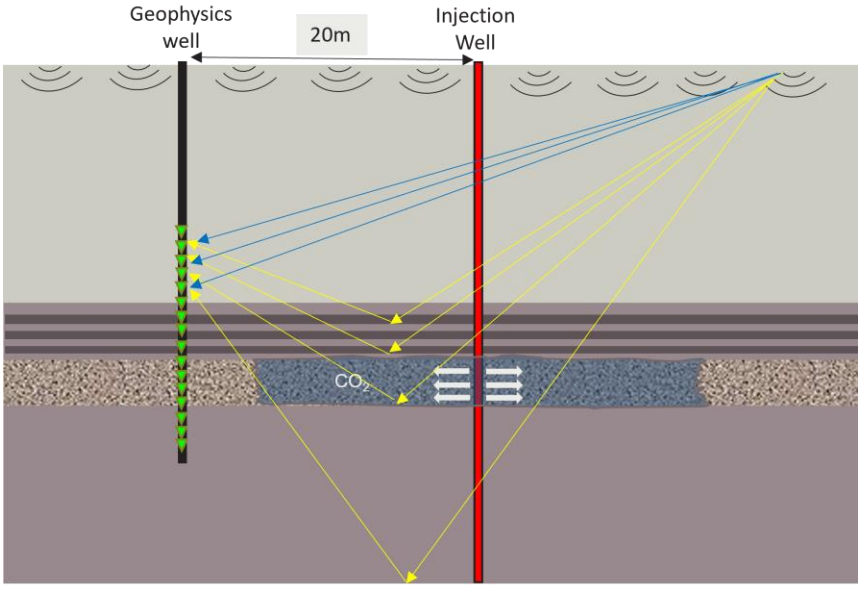

Figure 1.3 Schematic of VSP acquisition at CaMI.FRS (section view). Seismic sensors (green) in the geophysics observation well detect direct (blue) and reflected (yellow) arrivals of seismic waves generated at the surface. This allows for seismic monitoring of the injected CO_2 plume.

By recording downgoing arrivals, VSPs obtain information about the seismic wavelet and both shallow and deep subsurface velocity and attenuation information. In comparison

with surface receivers, recording with borehole receivers yields higher-resolution seismic images with a higher signal-to-noise ratio (SNR), albeit with more limited coverage (Figure 1.4). Repeated VSP surveys are therefore more likely than surface seismic to detect small changes in a reservoir, and to detect those change early. Time-lapse VSPs are a key contribution to the fulfilment of MMV requirements for geological CO_2 sequestration operations.

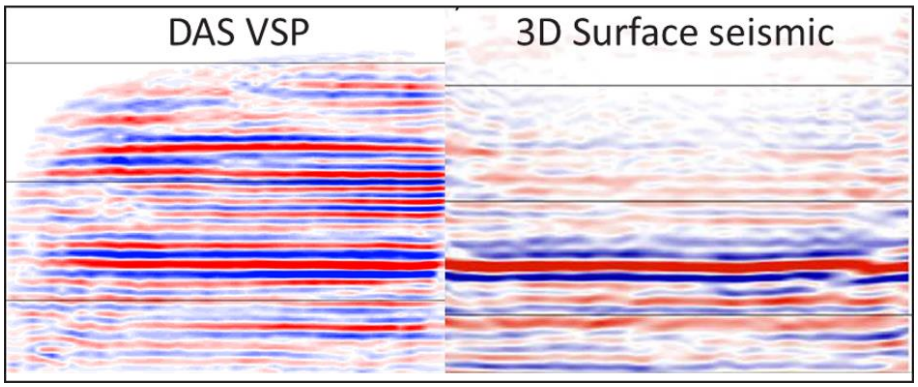

Figure 1.4 Comparison of reflection seismic data from VSP (DAS) and surface seismic from CaMI.FRS. Though acquisition parameters were not equivalent, this figure illustrates the higher frequency content, resolution, and SNR available with VSP data.

1.3.2 Time-lapse VSP monitoring

For time-lapse monitoring, baseline surveys record the initial conditions in the subsurface, prior to CO_2 injection. Subsequent monitor surveys record snapshots of the subsurface at the time of acquisition. Ideally, the differences between baseline and monitor datasets are solely caused by the elastic effects of increasing CO_2 saturation in the pore space of the reservoir. Using data from well logs and core samples at CaMI.FRS, the effects of CO_2 saturation on elastic reservoir properties had been previously modeled by Macquet et al. (2019). Partial gas saturation results in a decrease of P-wave velocity, a consequence of changes in the bulk elastic properties of the reservoir (Gassmann, 1951). The relationship between CO_2 saturation and the decrease in P-wave velocity is highly dependent on porosity and can be modeled with Biot-Gassmann fluid substitution (Brie et al., 1995; Gutierrez et al., 2012). Due to the sensitivity of P-wave velocity to gas saturation, time-lapse seismic is a reliable monitoring technology for geological CO_2 sequestration. Numerous field experiments, pilot projects, and industrial-scale operations have clearly demonstrated time-lapse VSP detection of gas-phase and supercritical CO_2 plumes, at

depths ranging from 400 m to 2000 m (Al Hosni et al., 2016; Bacci et al., 2017; Michael et al., 2020; Pevzner et al., 2021). Those pilot and industrial projects involved injection of CO_2 into relatively high porosity reservoirs (25%-30%), with correspondingly high-amplitude seismic anomalies from the CO_2. The challenge at CaMI.FRS has been to detect a comparatively lower CO_2 response in the seismic data, from a small injection volume of 33 t in a reservoir of significantly lower porosity (10%). A custom processing workflow was developed to optimize time-lapse VSP monitoring with the CaMI.FRS datasets.

1.3.3 Geophones and DAS overview

A detailed evaluation and comparison of geophone and Distributed Acoustic Sensing (DAS) field data from the CaMI.FRS is given by Gordon (2019). What follows is a condensed overview of geophone and DAS concepts relevant to time-lapse monitoring. Geophones are individual seismic sensors, typically used in arrays with multiple units separated by a consistent spacing. Geophones record seismic waves through oscillations of a magnet. 1-C geophones refer to a single component oriented vertically, while 3-C geophones contain three orthogonal components. 3-C geophones are thus able to record the full vector wavefield.

DAS employs a continuous fiber-optic cable, through which single or dual pulses of laser light are transmitted by a DAS interrogator unit (Daley et al., 2016; Hartog et al., 2017; Lindsey et al., 2020). Rayleigh diffractions occur within the fiber, resulting in back-scattered optical signals being recorded at the interrogator. As the seismic wave passes, the fiber experiences elastic strain, producing variable phase-alterations in the back-scattered light. The Rayleigh scattering and associated phase differences occur across a gauge length in the fiber, determined by the duration and spatial extent of the laser pulse. The gauge length determines the spatial resolution of the DAS data as well as the SNR (Dean et al., 2017), with a shorter laser pulse improving spatial resolution but reducing SNR. While gauge lengths are typically on the order of 10 m, trace spacing from DAS interrogator outputs can be finer by sampling within the gauge length (Lindsey et al., 2020), such as 0.25 m or 1 m in the DAS data presented in Chapter 6. The DAS interrogator records either the phase difference (radians) or rate of phase change (radian/s) in the backscattered light, outputting seismic traces proportional to strain or strain rate (Hartog, 2017; Lindsey et al., 2020).

When comparing geophone and DAS arrays for seismic monitoring, each presents advantages and disadvantages. In terms of longevity, the moving parts and electrical components of permanently installed geophones can malfunction over time, while the fiber optic cables used for DAS are static with no moving parts. Individual geophones record seismic traces with high SNR compared to individual DAS traces. The DAS fiber is also less sensitive than geophones to higher angles of incidence of seismic waves (Mateeva et al., 2014). DAS fibers necessarily extend from the surface, while borehole geophone arrays typically cover more limited depth ranges, as is the case at CaMI.FRS. Recording seismic data across a greater depth range and with finer trace spacing allows DAS data to achieve higher fold than geophone data during VSP CDP stacking (Daley et al., 2016). This mitigates much of the SNR disparity between the two data types. Permanently installed geophone arrays and DAS fibers at CaMI.FRS allows for the comparison of DAS and geophone data quality and time-lapse monitoring capability. Geophone data from the FRS acts as a ground-truth or benchmark against which the DAS data can be compared.

1.3.4 Other monitoring technologies

In addition to active seismic monitoring with VSPs and surface arrays, a suite of active and passive reservoir monitoring technologies has been employed at CaMI.FRS (Macquet et al., 2022). These include Electrical Resistivity Tomography (ERT), crosswell seismic and electromagnetic surveys, passive seismic monitoring, Distributed Temperature Sensing (DTS) with optical fiber in the injection well, temperature and pressure gauges in the injection and geochemistry observation well (Obs 1), and gas and fluid sampling the Obs 1 well. The variety of independent datasets will allow for integrated geological, geophysical, and geochemical interpretations, and the assessment of each technology's monitoring capabilities.

Confident detection of the CO_2 plume with time-lapse VSPs is a research priority at CaMI.FRS. The relatively extensive coverage of seismic data can act as a bridge between more localized borehole monitoring data, while those other data can validate seismic imaging and analysis. Geochemical sampling of reservoir fluids at Obs 1 is expected to provide insight into the VSP data's ability to image the diffuse edge of the CO_2 plume. Pressure gauge data will aid in de-coupling the gas saturation and pore pressure effects on P-wave velocity. ERT surveys performed with permanently installed surface and borehole

electrodes compliment VSP data by monitoring changes in the reservoir's electrical properties caused by resistive CO_2 displacing conductive brine in the pore space of the BBRS reservoir. Joint inversion of ERT and VSP data may help constrain reservoir models by independently measuring CO_2 saturation, if differences in spatial resolution and coverage can be addressed.

1.4 CO_2 detection threshold

In the context of informing expectations of leak-detection capabilities, the simulated-leak at CaMI.FRS provides a scenario in which CO_2 injected at a deeper interval has migrated to a shallower aquifer at 300 m depth. Examples of leak migration pathways that could cause such a leak include: a weakness in the cement annulus around an injection or observation wellbore, a pre-existing or pressure-induced fault or fracture, or a permeable zone in the caprock. Within the 6 m thick BBRS reservoir of 10% porosity, a small CO_2 injection amount produces a subtle seismic response most easily detected by time-lapse analysis. By 2021, CO_2 injection at the FRS allowed for a time-lapse VSP detection threshold to be established for a small CO_2 leak on the order of 10^1 t – 10^2 t, far below the kilotonne/year to megatonne/year injection rates typical of industrial scale CCS projects. In the case of the CaMI.FRS results shown this study, surpassing the detection threshold refers to the CO_2 plume reaching sufficient saturation and lateral extent that an unambiguous seismic amplitude anomaly can be observed visually by a seismic interpreter in the presence of background noise.

Though seismic response to CO_2 and corresponding detection thresholds are dependent on local geology and survey parameters, broad conclusions can be drawn from existing modeling and field data. Based on data from the Sleipner CO_2 sequestration operation in Norway, Chadwick et al. (2014) predicted 3D surface seismic may be capable of detecting leaks as small as: 315 t at 490 m depth, 950 t at 590 m depth, and 2100 t at 3000 m depth. VSP monitoring should be expected to have an even smaller detection threshold, due to its higher resolution. Pevzner et al. (2020) provide a VSP field data example of a kilotonne-scale detection threshold being achieved at 1500 m depth at the CO2CRC project in Australia. The South West Hub In-Situ Laboratory Project (SW Hub) in Australia provides a shallower CO_2 detection scenario of 40 t of CO_2 at 400 m depth in a 28% porosity reservoir (Michael et al., 2020). Given the clear seismic response obtained in individual

DAS shot gathers at the SW Hub, it is plausible to expect that an even smaller volume of CO_2 could have been detected in that high porosity setting. The SW hub experiment was approximately 100 m deeper than the 300 m deep BBRS reservoir at CaMI.FRS. Achieving a similar or smaller detection threshold in a lower porosity reservoir at CaMI.FRS provides additional, independent data about leak-detection and MMV capabilities. These findings can inform both shallow and deep permanent CO_2 sequestration and Enhanced Oil Recovery (EOR) operations.

1.5 Summary of research objectives

Using geophone and DAS data from 2017, 2018, 2019, and 2021, the objectives of this thesis work were to:

- Determine ideal time-lapse baseline and monitor surveys from the myriad datasets available from CaMI.FRS (Chapter 2).
- Set expectations of the plume's effects on pre- and post-stack VSP data using 1D and 2D forward modeling (Chapter 3).
- Develop a reliable time-lapse compliant processing workflow for geophone VSP data from the FRS (Chapters 4 and 5).
- Apply the workflow to DAS monitoring data (Chapter 6).
- Address the time-lapse repeatability challenges posed by variable near-surface filtering (Chapters 5 and 7).
- Establish a detection threshold and interpret the CO_2 plume (Chapter 8, Discussion).

CHAPTER 2 - DATASETS

2.1 Field data overview

Figure 2.1 shows a map view of the well and acquisition geometry at the FRS. VSPs were recorded in the geophysics observation well (Obs 2). The injection well (Inj) is offset from the geophysics well by approximately 20 m to north-east, with a geochemical observation well (Obs 1) located a further 30 m to the north-east. Monitoring surveys have been conducted periodically on a variety of walk-away and walk-around survey lines since injection began in 2017. Lines 7, 13, & 15 are centered on the Obs 2 well and avoid the buildings and infrastructure on site, allowing for repeatable shot locations from survey to survey. Although other walk-away and walk-around VSP surveys have been collected at CaMI.FRS, those shown in Figure 2.1 were most ideal for time-lapse. The University of Calgary's IVI Envirovibe truck was used as a source, with a sweep of 10 Hz – 150 Hz.

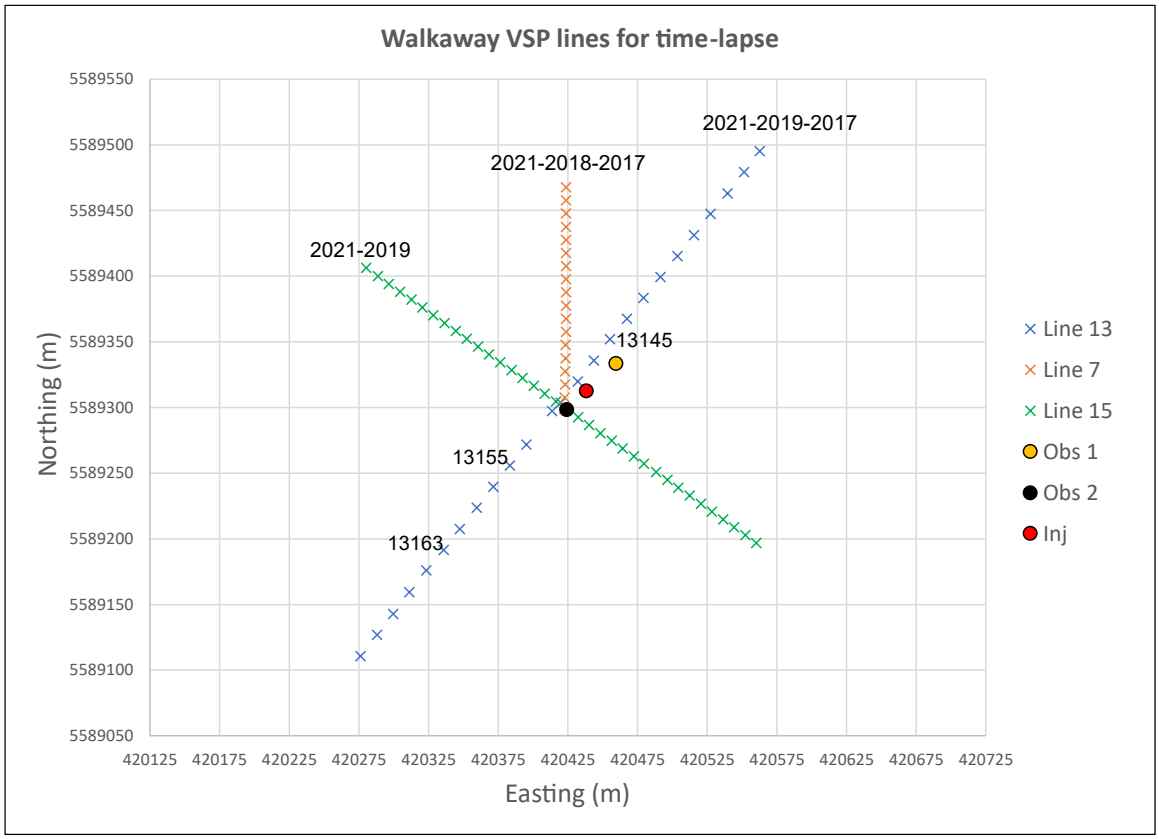

Figure 2.1 Map showing the positions of the injection well (red), geophysics well Obs 2 (black), geochemistry well Obs 1 (yellow). Walk-away VSP Line 13 was used to design the time-lapse compliant processing workflow. Lines 7 and 15 helped delineate the CO_2 plume. The three shots marked 13145, 13155, 13163 are referred to throughout the report.

Table 1 lists the time-lapse datasets used in this study. For brevity, survey dates are condensed to 'YearMonth' or 'YearMonthDay' format in Table 1 and throughout the rest of this document. Although baseline shot offsets extend to 500 m on Line 13, monitor surveys had reduced offset ranges due to the limited extent of the CO_2 plume. As the plume continues to grow, farther offsets could be acquired for future monitor surveys. Line 13 runs parallel to the three wells (Figure 2.1) and was expected to be the first to show the CO_2 anomaly in a time-lapse difference. The Line 13 geophone data was the most logical test dataset for developing a standard time-lapse compliant workflow (Chapter 4).

Table 1. Time-lapse VSP survey information

Line #	Orientation	Survey Date	Available shot offsets (m)	Shot spacing (m)
13	SW-NE	2017May	+/-500	20
13	SW-NE	2019Aug	+/-180	10
13	SW-NE	2021Mar1	+/-250	10
13	SW-NE	2021Mar25	+/-250	10
7	S-N	2017Jul	+/-250	10
7	S-N	2018Sep	+/-250	10
7	S-N	2021Mar1	250 North only	10
15	NW-SE	2019Aug	+/-180	10
15	NW-SE	2021Mar1	+/-250	10
13 (DAS)	SW-NE	2017May	+/-250	20
13 (DAS)	SW-NE	2021Mar1	+/-250	10
7 (DAS)	N	2017Oct	+/- 160	10
7 (DAS)	N	2021Mar1	250 North only	10

Observation well 2 (Obs 2) hosts 24 permanent 3-component geophones spanning 190 m to 305 m depth, at 5 m intervals. Shot spacing along Line 13 was initially 20 m in 2017. This was reduced to 10 m for the other monitoring lines and subsequent Line 13 monitor surveys. To avoid introducing dissimilarity in the time-lapse, only the shot locations that existed for each baseline-monitor pair of datasets were used. Available shot offsets typically spanned +/- 180 m to +/- 250 m depending on survey year. Shot locations were repeated each time, with only minor variations within +/- 1.5 m. Typically these variations were perpendicular to the survey line, and differences in shot offset were smaller still, within +/- 0.5 m. In order to avoid fold-imbalances in Common Depth Point (CDP) binning between baseline & monitor reflection data, minor differences in shot locations were treated as having identical source coordinates during processing.

2.2 Mass of CO_2 injected

Line 13 was used to develop the time-lapse compliant processing workflow. Line 13 datasets from May 2017, August 2019, and both March 1st and March 25th, 2021 were processed. These are referred to as 2017May, 2019Aug, 2021Mar1, and 2021Mar25. Table 2 shows the total mass of CO_2 injected between the baseline and monitor surveys. Initial expectations were for a higher rate of injection at the FRS, resulting in rapid detection of the CO_2 plume (Macquet and Lawton, 2017). However, the relatively small amounts of 15 tonnes and 33 tonnes of CO_2 at the time of the monitor surveys provides a valuable opportunity to establish a detection threshold for time-lapse VSPs in a shallow leak scenario. The limited plume extent also allowed for better calibration of the processing workflow, as individual datasets covered portions of the reservoir both with and without CO_2 saturation. The ability to detect a discrete CO_2 plume amid background residual noise increased confidence in the time-lapse VSP results.

Table 2. Total injected CO_2 by time monitor surveys

Monitor Survey	Total injected CO2 (t)
2019 August	15
2021 March	33

CHAPTER 3 - VSP FORWARD MODELING

3.1 VSP model description

A VSP forward model was used to assist with trouble-shooting the time-lapse processing workflow and aid with interpretation of the field data. This finite-difference model used the CREWES Matlab® Toolbox and generated baseline and monitor shot gathers using acquisition geometry equivalent to the field data. The elastic properties of the reservoir and a 29 t CO_2 plume were modeled based on fluid substitution and reservoir modeling work performed by Macquet et al. (2019), using semi-patchy saturation model based on Brie et al. (1995). Only the CO_2 plume's saturation effects were included for the VSP forward model. Pore pressure effects were excluded, to allow for the scenario of pore pressure declining towards initial reservoir pressure between injection periods and monitor surveys. The model therefore represents the minimum possible effect of the CO_2 plume on the seismic data. This 29 t modeled plume is comparable to the 33 t total injection amount at the time of the March 2021 monitor surveys. The reservoir model is a well-log based 1D model, expanded into 2 dimensions. Figure 3.1 shows the CO_2 saturation and P-wave velocity reduction in a percent-difference display. The reservoir modeling predicts CO_2 saturation to be vertically consistent throughout the reservoir, with saturation decreasing laterally out to a 25 m radius. The corresponding decrease in P-wave velocity is more vertically variable, due to mineralogy and porosity heterogeneity throughout the reservoir

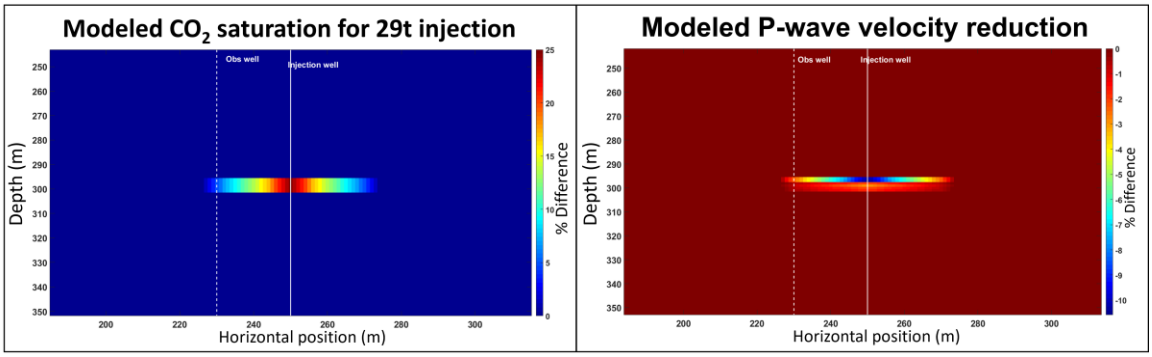

Figure 3.1 Modeled differences in CO_2 saturation and P-wave velocity from 29 t of CO_2. The CO_2 is contained in the 6 m thick BBRS reservoir and the plume has a lateral extent of ~ 50 m.

column. Due to the comparatively smaller effects of CO_2 saturation on density and S-wave velocity in the BBRS reservoir (Macquet et al., 2019), an acoustic model was deemed sufficient for the goals of this forward modeling exercise. This can be converted to an

elastic model in the future if the need arises. The magnitudes of P-wave velocity reductions in the model are plotted in Figure 3.2. Increasing CO_2 saturation gradually reduces the bulk modulus, causing 1%-10% reductions in P-wave velocity for saturations up to 25%.

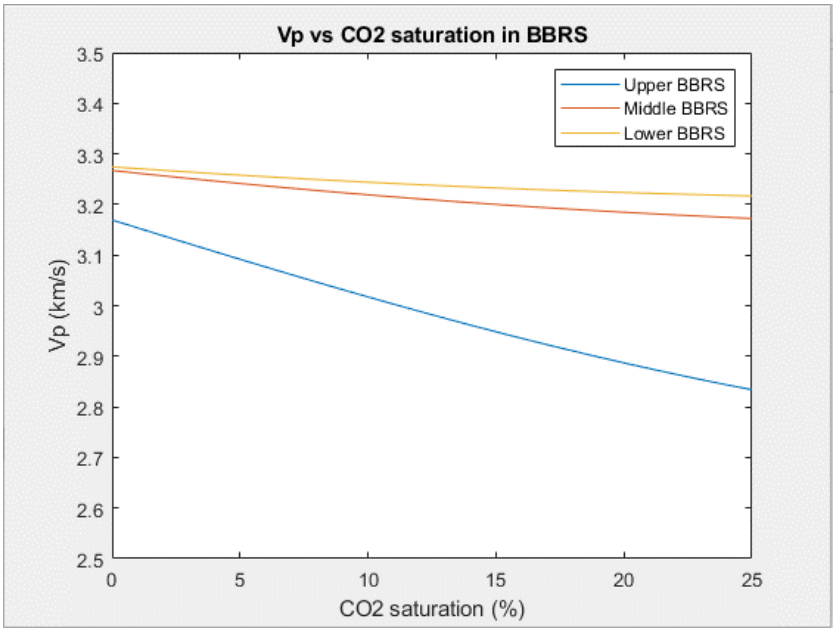

Figure 3.2 Modeled P-wave velocity changes for the BBRS reservoir with a semi-patchy saturation model from Macquet et al. (2019). CO_2 saturation varied from 0% to 25% for the modeled 29 t plume. P-wave velocity decreases gradually with saturation.

Figure 3.3 shows a 1D version of the P-wave velocity model and a synthetic seismogram showing CO_2 saturation affecting V_P and reflection amplitudes. Panels (a) and (b) show V_P reduced by 1%-10% within the BBRS reservoir. Panels (c) and (d) show the corresponding synthetic seismograms and time-lapse difference. The synthetic time-lapse anomaly manifests as a trough-peak with side-lobe energy, followed by travel-time delay residuals.

The 2D model in Figure 3.1 was used to generate synthetic VSP shot gathers in field-recorded time, using a ricker wavelet of 75 Hz dominant frequency to approximate the frequency content of the processed VSP data. No random noise was introduced, as the goal was to evaluate the effects of processing-related errors on the CO_2 amplitude anomaly. The gathers were processed in a simplified version of a walk-away VSP processing workflow, with no need for static corrections or deconvolution. This yielded a synthetic VSP CDP stack and time-lapse difference showing the synthetic CO_2 anomaly (Figure 3.4).

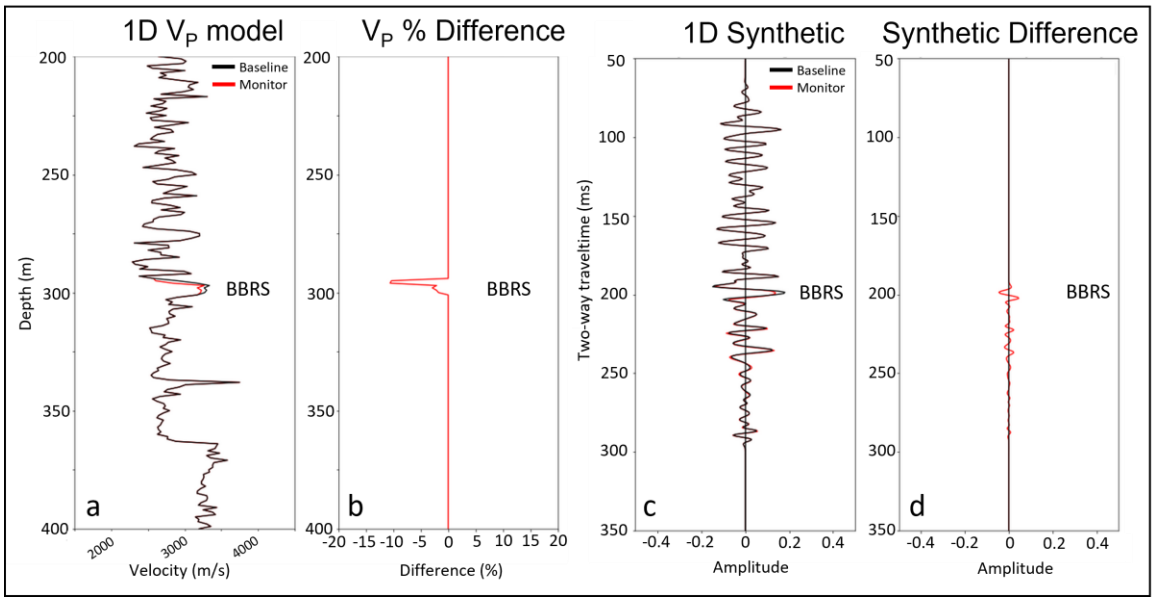

Figure 3.3 1D V_P model (a) and percent difference (b) caused by 0% and 25% CO_2 saturation. A synthetic seismogram (c) shows the seismic response. The time-lapse residual (d) is a trough-peak succession with side-lobe energy and a subsequent residual tail caused by travel-time delay.

As the observation well is offset by 20 m from the injection well, the symmetric CO_2 plume model manifests as an asymmetric anomaly in the VSP CDP stack. While the modeled plume was symmetrically distributed around the injection well, the asymmetric appearance is caused by the offset-dependent fold distribution of the CDP bins. In field data, the asymmetry would be further enhanced by differential attenuation for farther offset CDPs. As with the 1D model in Figure 3.3, the synthetic time-lapse VSP

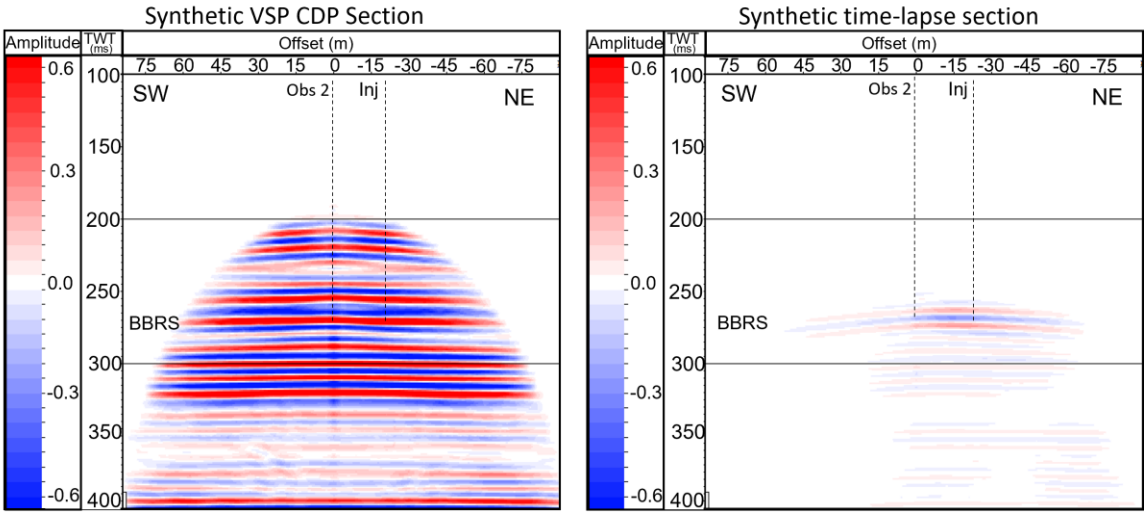

Figure 3.4 Synthetic VSP CDP stack and time-lapse difference from 29 t of CO_2. Reservoir interval indicated as BBRS. The reflection anomaly is in the form of a trough-peak succession with side-lobes, followed by a lower-magnitude residual tail from travel-time delay through the CO_2 plume.

anomaly is characterized by a reflectivity change and travel-time delay effect. The reduced acoustic impedance of the BBRS interval serves to decrease the amplitude of the strong positive and negative reflections at the top and bottom interfaces of the BBRS reservoir. This produces a trough-peak seismic anomaly with side-lobe energy. A two-way travel-time delay of ~0.2ms is caused by the CO_2 plume, producing a lower amplitude 'tail' below the reflection anomaly. Sampling the delayed reflection arrivals, which are effectively out-of-phase with the baseline arrivals, produces an amplitude difference in the time-lapse despite the travel-time delay of 0.2 ms being smaller than the sample rate of 1 ms. This lower amplitude travel-time delay residual is expected to increase in prominence with greater vertical permeation of the CO_2 plume.

3.2 Synthetic time-lapse tests

Previous time-lapse attempts with the VSP field data from CaMI.FRS had yielded high amplitude, coherent background time-lapse residuals which threatened to obscure the time-lapse anomaly and impede its early detection (Kolkman-Quinn and Lawton, 2020). Near-surface water-saturation and freeze-thaw effects introduced dissimilarity in the source signature between monitor and baseline field data. Differences in near-surface statics, frequency content, and attenuation had been observed. Exacerbated by the broadband nature of these shallow VSP datasets (10 Hz – 150 Hz), these near-surface effects were expected to be the main source of problematic coherent time-lapse residuals in the otherwise highly-repeatable time-lapse data. A cross-equalization step using a shaping filter was intended to mitigate these discrepancies (Al Mutlaq and Margrave, 2011). However, there was concern that the shaping filter would also diminish the amplitudes of both the reservoir reflection and travel-time delay anomalies between baseline and monitor surveys. The VSP forward model allowed for testing the relative impacts of static errors, bandwidth differences, and the shaping filter on the CO_2 plume time-lapse anomaly.

Comparison of static-corrected First Break (FB) times, between baseline and monitor geophone field data, yielded average FB pick differences within +/-0.25 ms. The first break times factor into normal move-out (NMO) corrections, two-way-time conversion, and VSP CDP mapping. Given the expected 0.2 ms travel-time delay effect, the minor differences in FB pick times led to concerns of negatively affecting the time-lapse anomaly. Random static errors with various ranges (+/- 0.1 ms, 0.25 ms, 0.5 ms, 1 ms, & 2 ms) were applied

to the synthetic monitor shot gathers to evaluate the impact on the time-lapse difference. It was determined that at +/- 0.5 ms and greater, progressively worse coherent time-lapse residuals manifested in the stacked synthetic time-lapse difference. At +/- 0.25 ms, the time-lapse residuals from static errors were not as damaging to the noiseless synthetic time lapse. Bandwidth differences of 5 Hz –10 Hz were also introduced between baseline and monitor synthetic gathers in order to generate high frequency time-lapse residuals in the synthetic difference. These tests indicated that unresolved amplitude and bandwidth differences in baseline and monitor amplitude spectra were expected to be the more significant contributor of unwanted time-lapse residuals in the field data. These effects could be compounded by static errors from inconsistent first break picks on poorly-matched or noisy time-lapse shot pairs. Care was therefore taken to ensure stable first break picks in the geophone and DAS field data (Chapters 4 & 6), while processing was tailored to avoid unnecessary amplitude alterations (Chapter 4) and reliable cross-equalizaton (Chapter 5).

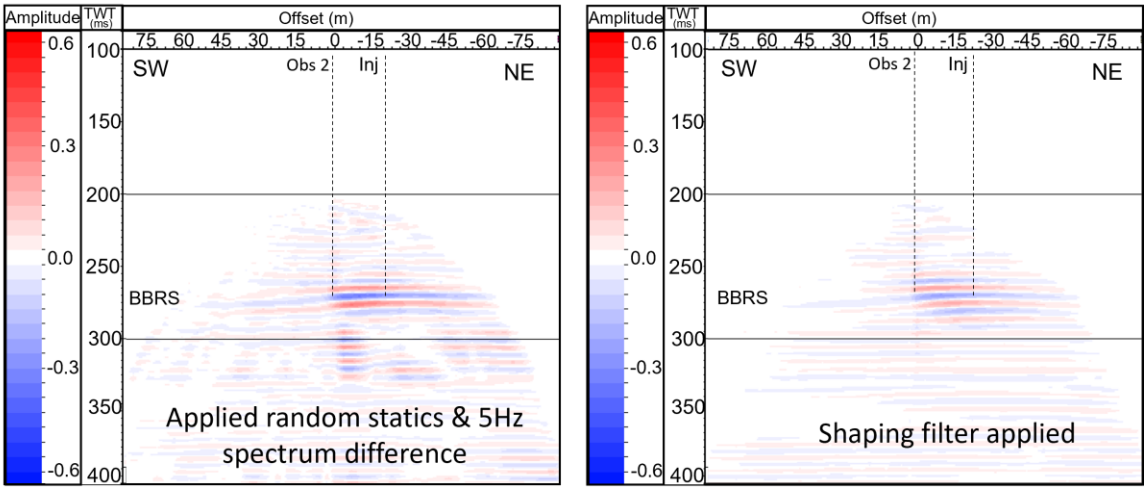

Figure 3.5 Synthetic time-lapse anomaly from a modeled 29 t CO_2 plume, with additional time-lapse residuals caused by filtering 5 Hz from the high end of monitor gathers' spectrum, and applying random shifts within +/-0.5 ms to pre-stack gathers. The application of a pre-stack shaping filter eliminated most of the residuals but weakened the CO_2 anomaly.

The left panel of Figure 3.5 shows the result of introducing a random static error of up to +/- 0.5 ms to the synthetic shot gathers, coupled with a 5 Hz frequency spectrum difference introduced by a bandpass filter. This artificial spectrum difference and subsequent time-lapse residuals are relatively minor when compared to the differences seen in the field data. These alterations produced high amplitude, semi-coherent and incoherent

residuals in synthetic time-lapse difference. A shaping filter, designed from the synthetic reflection data, eliminated much of the unwanted time-lapse residuals in the right panel of Figure 3.5. However, it also reduced the amplitude of the CO_2 anomaly, and the travel-time delay anomaly was rendered indistinguishable from the background time-lapse residuals. The shaping filter in this case was attempting to balance noiseless frequency spectra generated by a ricker wavelet and subsequently filtered by Ormsby bandpass filters. With additional sources of dissimilarity and noise in the field data, cross-equalization proved more challenging still. The forward modeling exercise provided valuable insight into the challenges of preserving the CO_2 amplitude difference during cross-equalization. This influenced the development of the time-lapse compliant workflow in terms of reducing sources of error and dissimilarity during processing between the baseline and monitor data, and seeking a satisfactory cross-equalization method to preserve the CO_2 anomaly.

CHAPTER 4 - FIELD DATA PROCESSING

4.1 Eliminating processing-related error

Initial time-lapse attempts were informed by Cheng et al. (2010) and Luo et al. (2018). This involved shaping filters and root-mean-square amplitude normalization to cross-equalize amplitudes and bandwidth. However, these initial attempts did not produce reliable, interpretable results with the CaMI.FRS data (Kolkman-Quinn and Lawton, 2020). To improve time-lapse compliance, the VSP processing workflow for FRS field data was further refined from those used by Gordon (2019) and Kolkman-Quinn and Lawton (2020), which had themselves been based on Hinds and Kuzmiski (1996) and the recommended workflows within Schlumberger's VISTA processing software help files.

The time-lapse compliant measures amounted to simplifying the existing workflows and removing as many amplitude scaling and filtering steps as possible. The objective was to avoid any processing steps that might unnecessarily introduce differences between baseline and monitor surveys. Simplifying the workflow also made it easier to assess the downstream effects of each processing step and iteratively improve the fine details of processing. What follows is a summary of the removed processing steps:

- 3-component data rotation was removed. Only the vertical components of the geophones were used, partly due to an increasing number of dead or sporadically malfunctioning horizontal components between 2017 and 2021. This eliminated error from trace interpolation, hodogram analysis, and 3-C data rotation, and allowed for a more direct comparison with straight fiber DAS data.
- Trace by trace mean-scaling steps (using first arrival amplitudes) were removed from the standard workflow. This step had been in place to remove spherical divergence effects from the downgoing arrivals. However, this amplitude scaling could instead be performed directly during deterministic deconvolution.
- An f-k filter and median filter were removed from the VSP CDP stack process. These were in the standard workflow to clean up pre-stack gathers, but caused unnecessary signal loss in the high SNR shallow data.
- RMS amplitude normalization was removed from the cross-equalization process. Amplitudes became directly comparable following the other changes, rendering this step unnecessary.

Following the removal of those processing steps, the testing of processing parameters and generation of time-lapse results became much more efficient and consistent. Figure 4.1 shows a flow-chart of the resulting processing workflow. What follows is a detailed description of the time-lapse compliant VSP processing, with emphasis on the steps that were key to ensuring maximum similarity between baseline and monitor shot gathers.

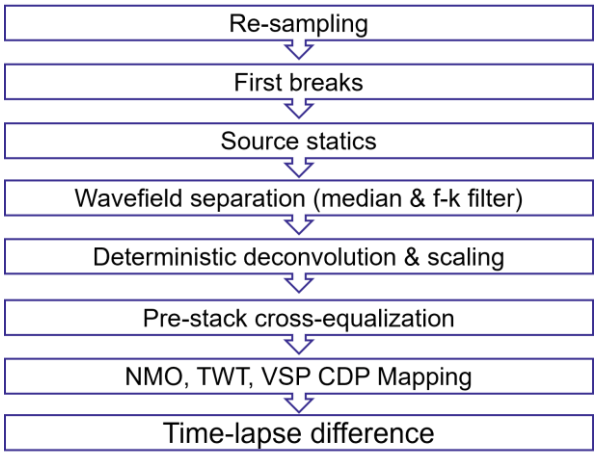

Figure 4.1 Flow-chart of time-lapse compliant VSP processing workflow for 1-C data.

4.2 Time-lapse compliant processing flow

4.2.1 Re-sampling

Most CaMI.FRS datasets were acquired with 1 ms sampling, though some 2 ms data exists. When necessary, data was re-sampled from 2 ms to 1 ms in the frequency domain using VISTA software. Re-sampling from 2 ms to 1 ms did not result in obvious errors, while providing a less visually-distracting display. This allowed for the same f-k filters to be used for baseline and monitor data. Spatial re-sampling was not necessary for the geophone data, as the borehole geophones are permanently installed at known intervals. However, spatial re-sampling is required for DAS time-lapse datasets, when different DAS interrogators produce different output trace spacing.

4.2.2 First breaks

First, raw data were phase rotated by -90^0 prior to picking first breaks. The first break picks are used throughout processing, crucially determining NMO corrections and two-way-travel time conversion. Any variability leads to artificial differences in the time-lapse comparison. In comparison with data from two different impulsive sources tested at the FRS, the vibe first arrivals superficially appeared phase-rotated by approximately -90^0

(Figure 4.2). This may be an artifact of the correlation of the physical vibe-sweep with a synthetic sweep. The vibe first arrivals in these datasets had previously been observed to contain high and low frequency artifacts, but as these are invariably removed by deterministic deconvolution, first-arrival waveform had not been a major source of concern. However, in comparing first break times after static corrections, it was determined that picking FBs on the phase-rotated data led to a closer match between baseline and monitor shot gather pairs. The first breaks were picked on a trough, equivalent to a downgoing compressional impulse recorded as a negative amplitude by the upward-oriented vertical geophone component. In the un-rotated data, the first breaks seemed to shift up or down with frequency content. Phase-rotating the data led to stable first break picks on the trough, regardless of frequency content. This phase rotation had no impact on the final deconvolved reflection amplitudes, as it applies to both the upgoing and downgoing wavefields in the raw data. The phase rotation is removed automatically during deterministic deconvolution, which is based off the phase-rotated downgoing wavefield. Four of the 24 vertical geophone components died after installation and were missing in each of the datasets. These traces were interpolated prior to picking first breaks.

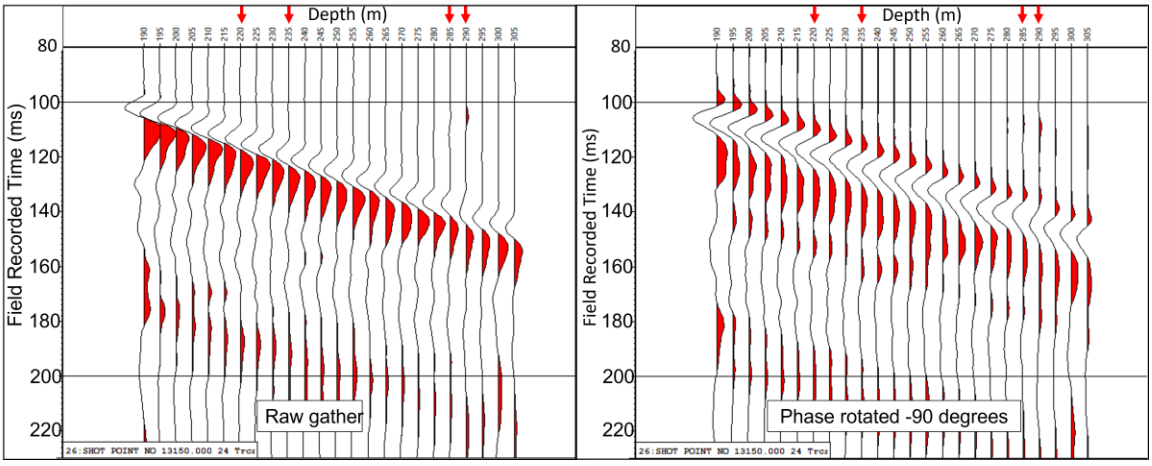

Figure 4.2 Example of a raw shot gather before and after a -90^0 phase rotation. Four dead traces were interpolated (red arrows). The phase rotation led to a zero-phase appearance. This resulted in stable 'trough' first break picks between baseline and monitor shot gathers despite differences in frequency content.

4.2.3 Source static corrections

Source-static corrections were applied to all datasets using the same velocity model for each, in a process described by Lawton et al. (2019). Briefly, the first break times were

modeled using VISTA software, by ray tracing with a 1D-based velocity model. Root-mean-square differences were determined between the actual and predicted first break times. Heterogeneity in the near-surface causes first-break times to vary between neighbouring shots. Figure 4.3 shows examples of this FB variability, such as between shots 7159 and 7160. Such differences are reconciled with the velocity model.

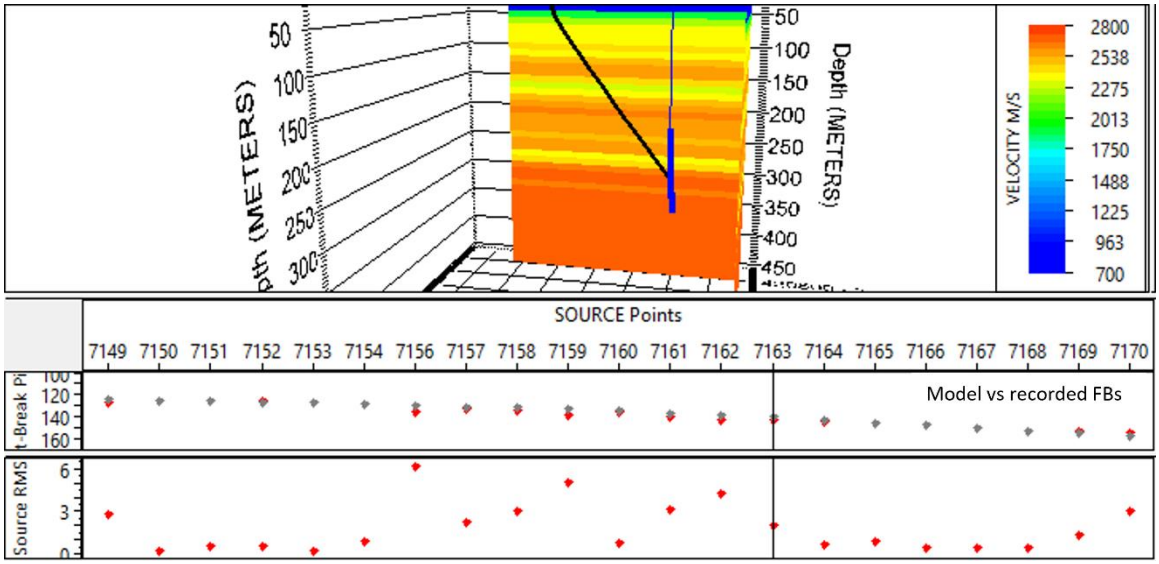

Figure 4.3 Example of source static corrections obtained from ray-tracing in VISTA software.

In addition to near-surface velocity variations between shot locations, seasonal variability in static errors were also present between the baseline and monitor data. Comparing 2019Aug and 2021Mar monitor data to the 2017May baseline, differences in first arrival times could be observed. Figure 4.4 shows the median-difference between baseline and monitor first break picks for geophone data from Line 13. Caused by changes in water saturation, ground water depth, and melt-freeze effects, this FB variability between baseline and monitor surveys was typically within 1 ms to 2 ms. Several shot locations showed first break time differences up to 4ms. Minor differences in shot location must also contribute to the variability in first arrival times, but these were not observed to correlate with Figure 4.4. Shot location differences were therefore considered to be a second order effect for most locations, compared to the seasonal variations at the surface and shallow subsurface. As expected, the 2021Mar1 survey, performed in frozen conditions, had the earliest first arrival times due to relatively high near-surface velocities.

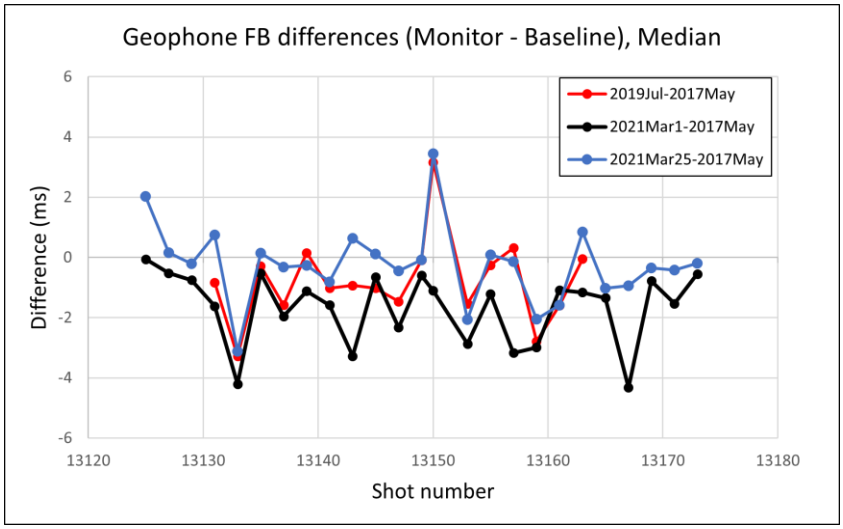

Figure 4.4 Differences between geophone monitor and baseline first arrival times by shot location. Seasonal variability in the near-surface caused travel time differences up to 4ms.

The source static corrections adequately minimized the relative differences in first break times between the time-lapse datasets. However, unrelated to time-lapse repeatability, a set of residual static corrections were also determined and applied further along the processing workflow. Due to the 1D nature of the velocity model, the model-based source static corrections fit an overly simplistic travel-time prediction. Inspection of processed, pre-stack shot gathers in two-way-time (TWT, +tt) showed reflections such as the BBRS marker shifted between neighbouring shots (Figure 4.5), with error increasing with offset.

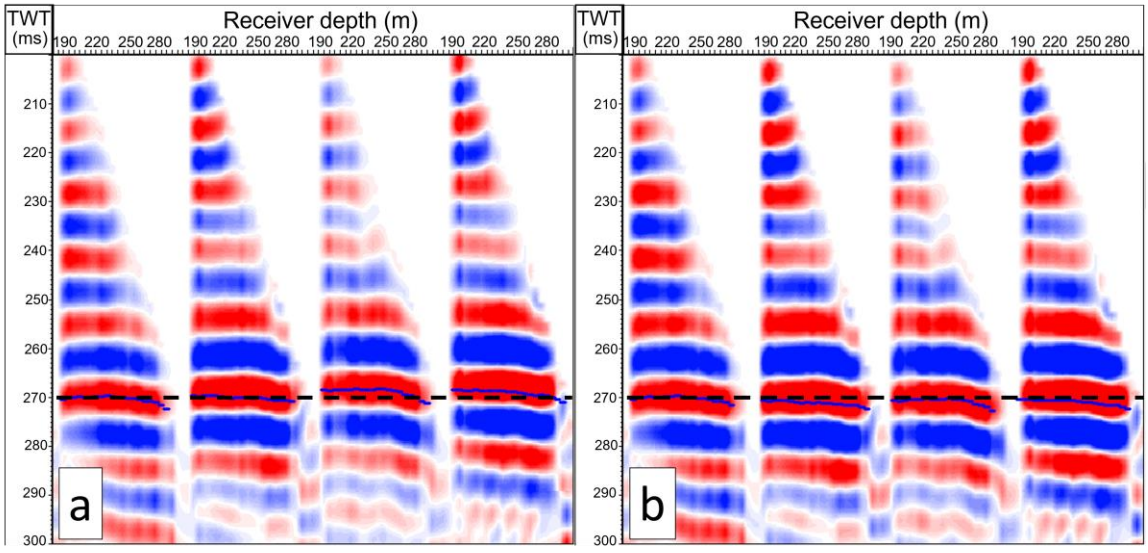

Figure 4.5 Minor residual static errors existed between neighbouring pre-stack shot gathers (a), despite earlier static corrections. These were corrected by minor bulk shifts (b) in TWT, improving the VSP CDP stack. The corrections were applied to both baseline and monitor data.

Testing of tomographic velocity model inversions did not produce satisfactory solutions, so a work-around was devised: Determining bulk shifts (0 ms - 4 ms) for each shot to shift the BBRS and reflection to a datum of 270 ms. This 270 ms datum was chosen as it was a round number representing the typical near-offset arrival time of BBRS reflections, in two-way-time. A bandpass filter applied prior to choosing the bulk shifts prevented frequency-related variations in the waveform from adding error to the bulk shift picks. Applying this manual residual static correction to the processed, pre-stack, TWT gathers prevented stacking-related artifacts from constructive and destructive interference in the VSP CDP stacks. As the processing assumed flat layering in the subsurface, any loss of structure in this process was deemed acceptable. This work-around solution was intended to be temporary and could be avoided in the future with a better 2D near-surface velocity model. As initial attempts to do so failed, and the issue was considered unimportant for time-lapse analysis, this work-around became a standard part of the processing workflow. With regards to time-lapse, the manual residual static corrections were determined for the baseline data and the same set of corrections was applied equally to the monitor data, introducing no relative difference between the two.

4.2.4 Wavefield separation

After FB picks and initial source static corrections, the data were flattened to a 100ms datum (-tt) and the downgoing wavefield was isolated using a 25 m (5-trace) spatial median filter (Gordon, 2019). The median filter was applied to the flattened (-tt) raw data without any mean-scaling of first arrival amplitudes. With these CaMI.FRS datasets, wavefield separation via median-filtering has reliably produced better final results than f-k filtering. This median filter does not appear to significantly alter the individual first arrival amplitudes for the geophone data. Any minor effects on trace amplitudes were presumed to be equivalent between time-lapse datasets. Due to the use of only vertical geophone components, wavefield separation was accomplished by simply subtracting the downgoing wavefield from the raw data, and then applying an f-k filter to isolate and de-noise the upgoing P-wave reflections. The wavefield separation process is illustrated in Figure 4.6. The downgoing wavefield subtraction sometimes produced high amplitude time-lapse residuals on the upgoing wavefield (Figure 4.6c). These subtraction errors are mainly due to the small alterations of the downgoing arrivals caused by the 5-trace median filter, as

well as to imperfections in the interpolated dead traces. However, these subtraction errors were minimized after f-k and bandpass filters were applied to the upgoing wavefield (Figure 4.6d).

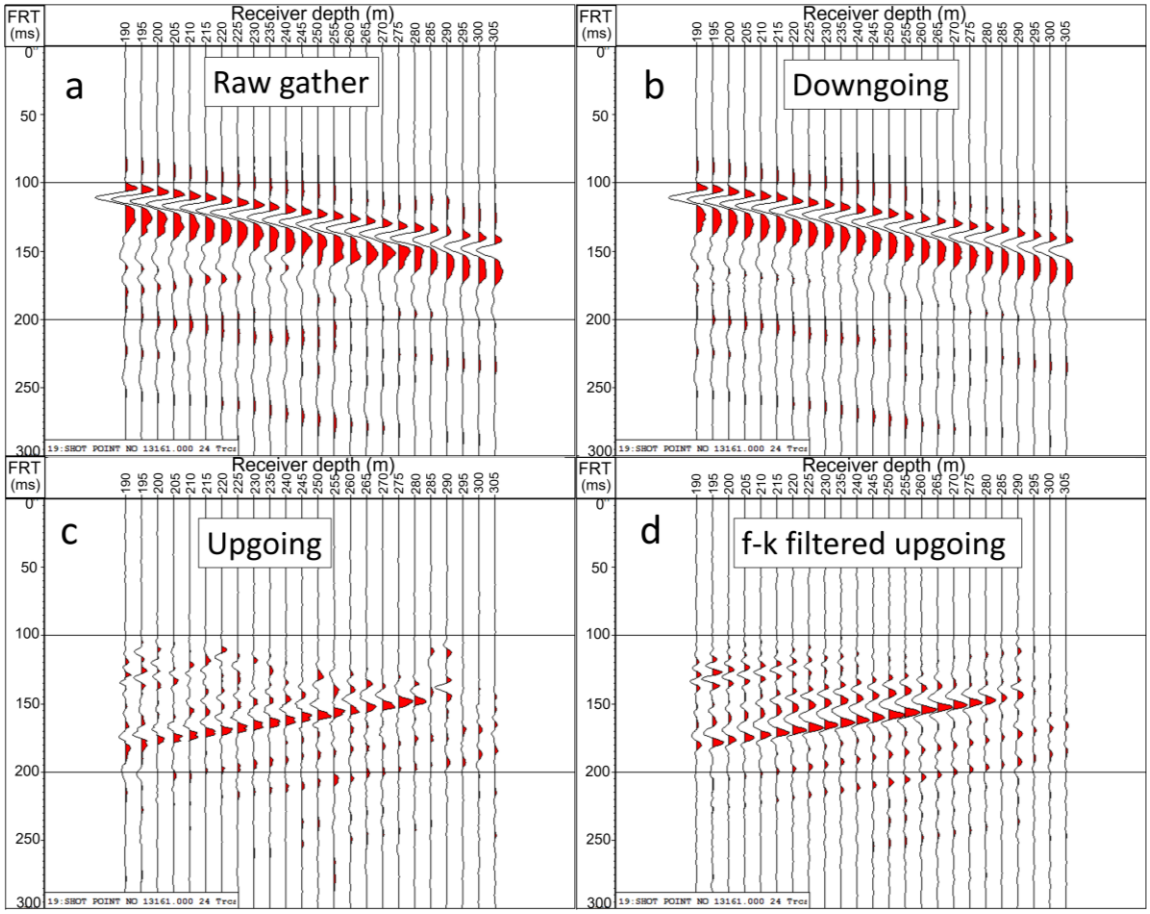

Figure 4.6 Wavefield separation starting with raw shot gather (a). The downgoing wavefield (b) is subtracted from the raw shot gather resulting in the upgoing wavefield (c) which is cleaned with an f-k and bandpass filter (d) prior to deconvolution. Amplitudes not equally scaled for diplay purposes.

4.2.5 Deconvolution and scaling

Deterministic deconvolution was performed using a window of -100 ms to +200 ms around the first break times. Trial and error testing with various CaMI.FRS field data had determined that a long design window for the deconvolution operator works best to remove the artifact-ridden first arrivals of the correlated vibe-sweep. Less consistent results were obtained when using a short, 40 ms-50 ms window around the first arrivals. Extending the window -100 ms before the first breaks helps capture the tails of the entire correlated waveform. As an aside, this -100 ms extension to the deconvolution design window was found to prevent the artificial time-shift discrepancy between DAS and geophone data

previously reported by Lawton et al. (2019). That time shift was apparently a deconvolution artifact and could be reproduced on numerous datasets by using an overly short design window. Following deterministic deconvolution, a noticeable improvement in frequency content was apparent in the VSP data (Figure 4.7).

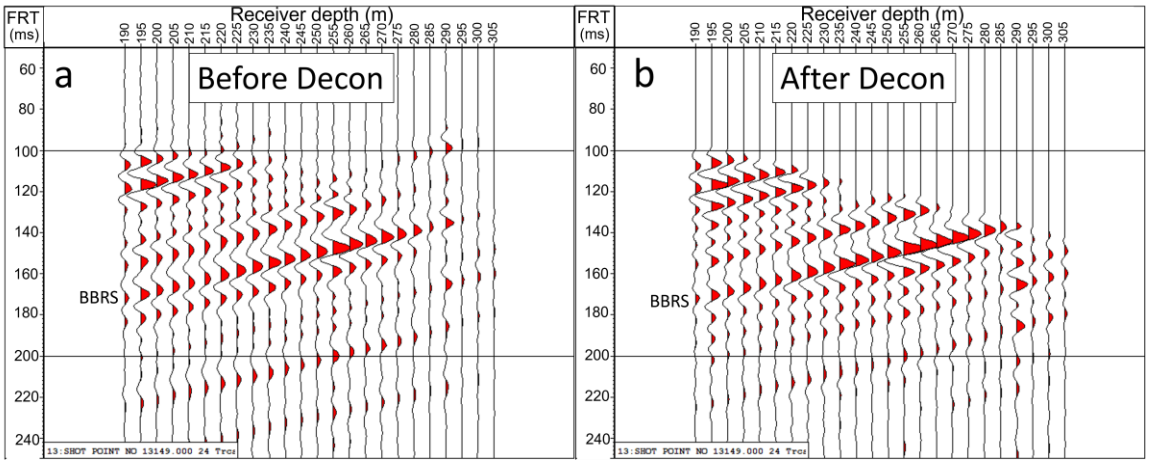

Figure 4.7 Reflection data from a shot gather before (a) and after (b) deconvolution. The spectral balancing effect of deconvolution is most evident in the higher frequency wavelets between 120ms and 180ms. A mute was also applied in the process. The BBRS marker is indicated.

It is important to note that no trace amplitude normalization was performed prior to deconvolution, unlike in standard workflows or in earlier processing attempts with these data (Gordon, 2019; Kolkman-Quinn and Lawton, 2020). Therefore, each trace's deconvolution operator contains amplitude and phase information on the cumulative effects of the source wavelet down to the time of the first arrival. These effects include: seasonally variable near-surface filtering, spherical divergence, attenuation, and

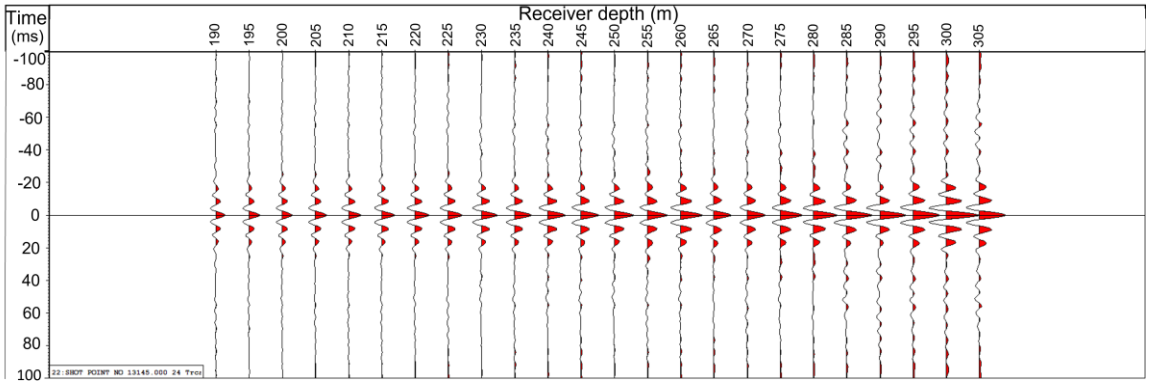

Figure 4.8 Deconvolution operators from the downgoing direct arrivals. This example is from shot 13145, offset 50m NE from Obs 2. No scaling has been applied. The shallower receivers (left-side) have the highest amplitude and least attenuated direct arrivals. This leads to lower-amplitude deconvolution operators and less high-frequency scaling than the deeper operators (right-side).

transmission loss. In a zero-offset shot gather, deconvolution effectively removes each of these effects from the reflection data in one step. Progressively deeper deconvolution operators therefore have progressively greater amplitudes and higher frequency scaling effects (Figure 4.8). In a sense, the deconvolution operator acts to normalize the reflection amplitudes by dividing out the downgoing wave amplitudes. This renders baseline and monitor amplitudes directly comparable across most of the amplitude spectrum without need of root-mean-square normalization or any other amplitude scaling step. While the deconvolution operator removes some of the seasonally-variable near-surface filtering effects, those effects aren't completely reversible. This causes the deconvolved spectra to match within a limited band of frequencies, rather than the full bandwidth (Figure 4.9).

For upgoing reflections, the additional spherical divergence (beyond the first arrival time) was corrected for by multiplying flattened (-tt) reflection amplitudes by travel-time (t^1). This is a zero-offset assumption that breaks down to some extent for farther offset shots, as the direct arrival does not share the same downgoing raypath as the reflected arrivals. In the CaMI.FRS setting, raypaths were relatively straight due to similar interval velocities above the reservoir (Figure 4.3). A t^1 spherical divergence correction seemed reasonable, although its effects were minimal. Additional attenuation also takes place for the upgoing reflection raypath. This was assumed to be equal between baseline and monitor data and was ignored to maintain the simplicity of the time-lapse processing workflow. Deconvolution and associated assumptions are discussed in more detail in Chapter 7.

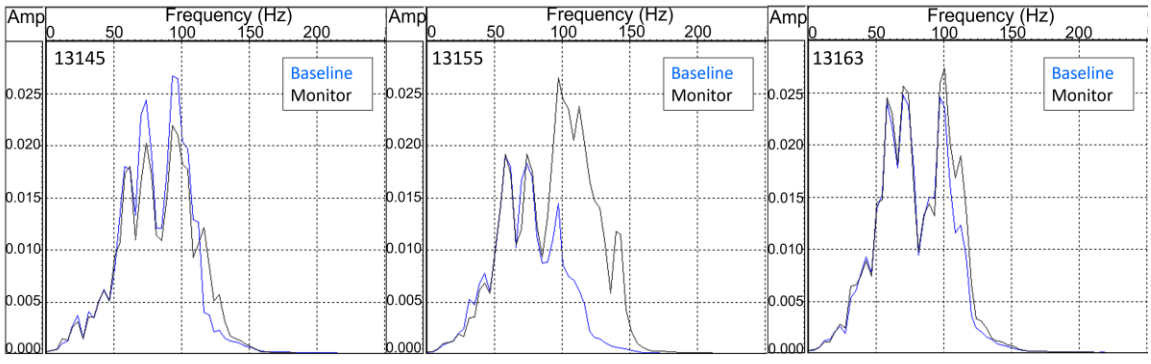

Figure 4.9 Amplitude spectra (identical scales) of pre-stack gathers for shots 13145, 13155, and 13164 from 2021Mar1 (black) & 2017May (blue). A 0ms-400ms window included the BBRS reflection. Shot 13145 reflects off the CO_2 plume and shows a decrease in overall amplitude caused by the strong BBRS reflectivity. 13155 and 13163 are SW of Obs 2 and do not reflect off the CO_2 plume. Deconvolved amplitudes match nearly exactly to 80Hz-100Hz, after which major (13155) and minor (13145, 13163) differences remain. These spectral and bandwidth differences are caused by seasonal variability in near-surface filtering.

The deconvolution-based scaling process led to the highest degree of similarity achieved so far with CaMI.FRS baseline and monitor shot gathers. This simple workflow reduced unwanted background time-lapse residuals and eliminated the need for further scaling during cross-equalization. The good match between baseline and monitor spectra in Figure 4.9 confirmed that amplitudes have been properly and independently scaled by each trace's deterministic deconvolution operators. Amplitudes were directly comparable, except beyond the frequency at which unresolved near-surface attenuation effects caused a divergence in the baseline and monitor spectra. Figure 4.9 shows examples of such differences, both minor and major. These spectra are from a 400ms window which includes the BBRS interval, containing the reflections seen previously in Figure 4.7.

Shot 13145 was on the opposite side of the injection well from the geophone array in Obs 2 (see Figure 1.3). This shot can be expected to include reflections from the CO_2 plume around the injection well. In Figure 4.9, shot 13145 has lower overall amplitude in the monitor data, indicating the presence of CO_2 which reduces amplitude of the strong BBRS reflection. Some shots have nearly identical baseline and monitor bandwidths (Figure 4.9 – shots 13145 & 13163), indicating near-surface filtering effects were approximately equal and have been mostly mitigated by deconvolution. However, in other shot gathers there remain significant differences in bandwidth and high frequency attenuation (Figure 4.9 – shot 13155). Since the differences caused by seasonal variability in near-surface filtering could not be entirely reversed by the deconvolution operator, high frequency residual amplitudes would result from direct subtraction of baseline and monitor data. If left unresolved, these residuals would obscure the CO_2 plume amplitude anomaly. With these high quality, high frequency shallow seismic data from CaMI.FRS, addressing the seasonal variability in the data was of critical importance to the time-lapse results. Two pre-stack cross-equalization methods were tested to minimize these time-lapse residuals prior to VSP CDP stacking, discussed in Chapter 5. An extended analysis of the relationship between near-surface filtering and deterministic deconvolution takes place in Chapter 7.

4.2.6 VSP CDP stack

Following wavefield separation and deconvolution, spherical divergence and Normal Move-Out (NMO) corrections were applied to all datasets using the same velocity model. Reflection data was then converted to two-way time equivalent (+tt). This flattens the

reflected arrivals, as seen earlier in Figure 4.5, albeit with severe vertical exaggeration in that display. At this stage, the processed pre-stack shot gathers were ready for cross-equalization prior to VSP CDP mapping and stacking. Following cross-equalization, reflection data were mapped and stacked into 3m CDP bins, the smallest practical bin size for these geophone data. Figure 4.10 shows VSP CDP mapped shot gathers for shots 13145, 13155, and 13163, as well as a full VSP CDP stacked section from the 2017May baseline survey. Panels a, b, and c show the footprint of the CDP mapped shot gathers prior to stacking. The coverage of each gather depends on shot location, receiver depths, and the deviation of the well.

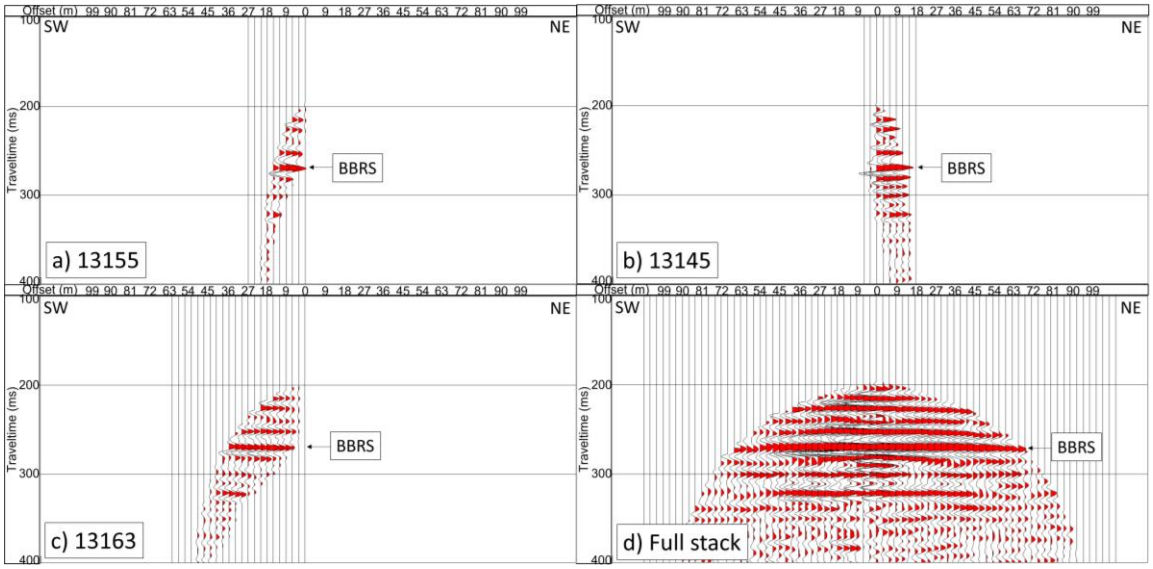

Figure 4.10 VSP CDP mapping of shot gathers 13155 (a) 13145 (b) 13163 (c) and a full walkaway VSP CDP stacked section (b) from the Line 13 2017May baseline geophone survey.

Corridor mutes were tested but were not applied prior to stacking, as multiples were not observed to be interfering with the geophone data. Migration was not performed pre- or post-stack. At the FRS location, the BBRS reservoir has a dip of approximately 0.5^0 (Dongas, 2016). With a nearly flat layering in the subsurface at the field location and an apparent lack of diffractions in the field data, neither pre-stack nor post-stack migration was considered a priority while developing the time-lapse compliant workflow. With successful results achieved, a migration step can be added in the future.

CHAPTER 5 - CROSS-EQUALIZATION AND TIME-LAPSE RESULTS

5.1 Frequency content assessment

The geophone array's limited coverage rendered post-stack shape-filtering impractical (Kolkman-Quinn and Lawton, 2020). Regardless, pre-stack cross-equalization was preferable with the high SNR data. Due to the high signal strength of the shallow geophone data (190m-305m) and the coherent appearance of the minimally-filtered reflection data, random noise and multiples were not a significant cause for concern. In the context of carefully processed highly-quality field data, the cross-equalization step was mainly needed to resolve the bandwidth and attenuation differences caused by seasonal variability in near-surface filtering. Cross-equalizing the near-surface effects before stacking was expected to result in greater similarity in the baseline and monitor data.

Although field observation notes did not include weather and surface conditions during acquisition, an appraisal of the relative frequency content of each survey shows a trend broadly consistent with seasonal and monthly weather expectations. The baseline survey, acquired in May 2017 (2017May), has a relatively low dominant frequency. By comparison, the 2019Aug monitor survey had generally broader frequency content and less near-surface attenuation. The 2021Mar1 data was the least attenuated, likely due to frozen ground conditions following prolonged cold weather in February 2021. Finally, the 2021Mar25 survey occurred after a particularly warm March with daytime highs consistently between 5^0C and 20^0C. This would have caused melting at and near the surface, reducing the amplitude and frequency content of the source wavelet. This qualitative relationship is summarized in Table 3.

Table 3. Relative frequency bandwidth of Line 13 baseline and monitor surveys

Survey	Relative Frequency Bandwidth
2017May	Low
2019Aug	Medium
2021Mar1	High
2021Mar25	Low

Coincidentally, the 2017May and 2021Mar25 surveys yielded similar frequency content overall, but with variability at each shot location. This made it easier for a shaping filter to balance amplitude spectra between 2017May and 2021Mar25 datasets. Conversely, the

2021Mar1 survey had the broadest and least-attenuated amplitude spectra. It was therefore most effective to apply high-cut filters to closely match the 2017May spectra. Both shaping filter and high-cut filter methods of cross-equalization were tested.

5.2 Normalized Root-Mean-Square

While developing a VSP workflow, Normalized Root-Mean-Square (NRMS) was the principal metric used to quantitatively assess similarity between datasets improvements in the workflow. The NRMS difference between two seismic traces a_t and b_t is given by Equation 1 (Kragh and Christie, 2002),

$$NRMS = \frac{200\text{x}RMS(a_{t-b_t})}{RMS(a_t)+RMS(b_t)}. \quad (1)$$

Expressed as a percentage from 0% to 200%, lower NRMS values indicate high similarity between data. NRMS is sensitive to amplitude and phase differences as well as random noise (Kragh and Christie, 2002). NRMS differences were calculated between shot gathers to inform cross-equalization, and between stacked sections to assess final results.

5.3 Shaping filter design: Reflected arrivals

Shaping filters minimize the differences between two datasets, and can be considered a least-squares solution to a matrix equation (Al Mutlaq and Margrave, 2011). Shaping filters were applied to the higher frequency monitor surveys in order to filter down towards the lower frequency baseline. Shaping filters designed from both downgoing arrivals and upgoing reflection data were tested. The upgoing filter was expected to be more sensitive to the higher frequency bands in the deconvolved data, further discussed in Chapter 5.4. The shaping filter designed from reflection data used a 400 ms design window and a 40 ms operator length. Due to limited shallow data above the BBRS interval, it was not possible to exclude the reservoir from the shaping filter design while also obtaining a stable result and retaining most of the traces (Kolkman-Quinn and Lawton, 2020). The design window was chosen to avoid overfitting the shaping filter to the high amplitude BBRS reflection in the window. Trial and error testing led to the design parameters, although the results were not highly sensitive to minor variations in the design window and operator length.

Figure 5.1 shows the effects of the shaping filter on the reflected amplitude spectra of shots 13145, 13155, and 13163. In shot 13145, the shaping filter equalized the already-

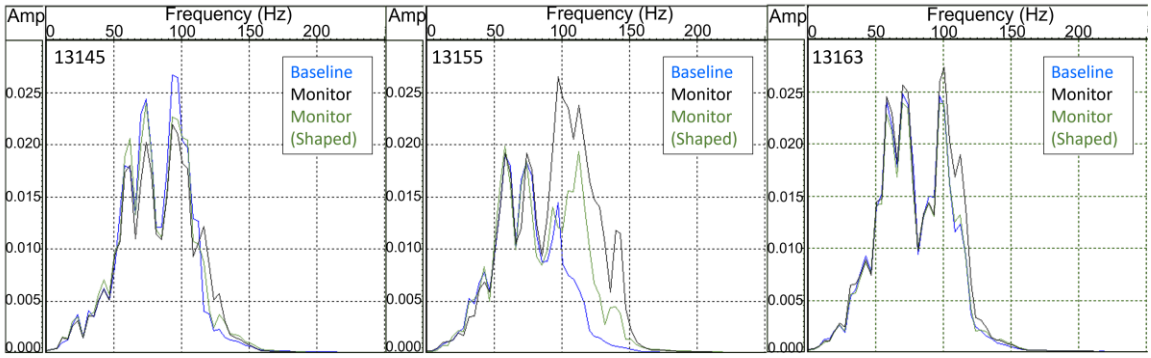

Figure 5.1 Amplitude spectra of pre-stack gathers for shots 13145, 13155, and 13164 from 2021Mar1 (black) & 2017May (blue). Upgoing-designed shape-filtered monitor data in green. In shot 13145, the shaping filter appears to negatively affect the interpreted reflection amplitude decrease from the CO_2 plume. The shaping filter adequately balances the very similar amplitudes in shot 13163, but fails to balance the extreme differences in shot 13155.

similar bandwidths. However, it also raised the 50 Hz-75 Hz amplitudes closer to baseline. Assuming the original monitor data amplitudes were correct, this alteration would imply a weakening of the time-lapse anomaly. In shot 13155, the extreme spectral differences were not eliminated by the shaping filter, leading to high frequency time-lapse residuals. Finally, shot 13163 began with a nearly identical spectrum, and the shaping filter successfully cross-equalized the minor differences. The results in Figure 5.1 indicate that the shaping filter is not universally reliable in the presence of variable near-surface filtering effects.

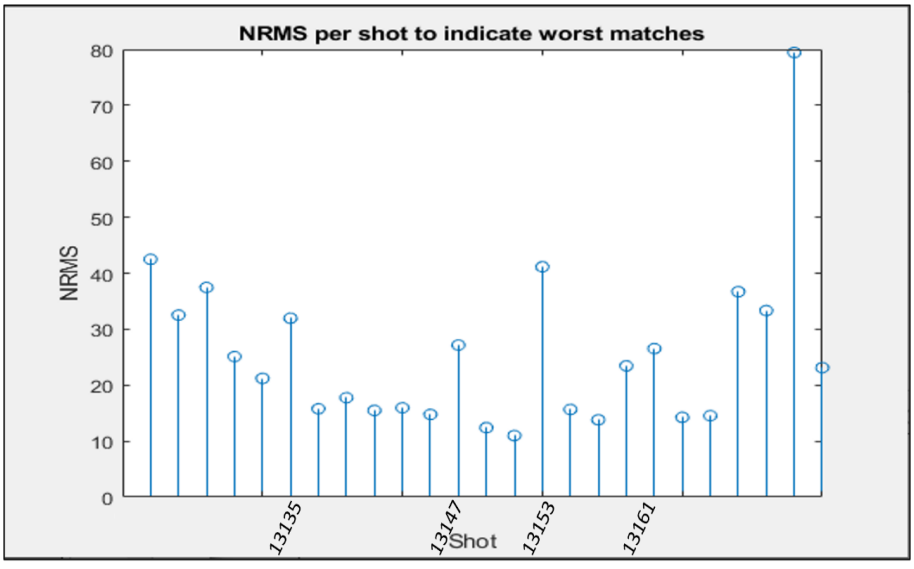

Figure 5.2. NRMS values calculated over a 0ms-400ms window for each baseline-monitor shot gather pair from the 2021Mar25 – 2017May time-lapse, prior to shape-filtering. The indicated shot numbers had anomalously high NRMS values above the trend, indicated particularly poorly matching shot gathers which remained unbalanced after shape-filtering. All shots were inspected pre- and post-stack, but only these 4 were discarded for the upgoing-designed shaping filter method of cross-equalization.

A significant improvement in the time-lapse result was obtained by inspecting the pre-stack gathers for high levels of dissimilarity. Previous analysis had determined that the footprints of individual shots often manifested in the stacked VSP time-lapse result, causing coherent time-lapse residual amplitudes (Kolkman-Quinn and Lawton, 2020). By calculating NRMS values for matching baseline-monitor shot pairs, highly dissimilar shots could be identified for inspection (Figure 5.2). After shape-filtering, these highly dissimilar shots typically caused the strongest background time-lapse residuals. Figure 5.3 shows the effect of the shaping filter trying to reconcile very dissimilar and very similar shot gathers,

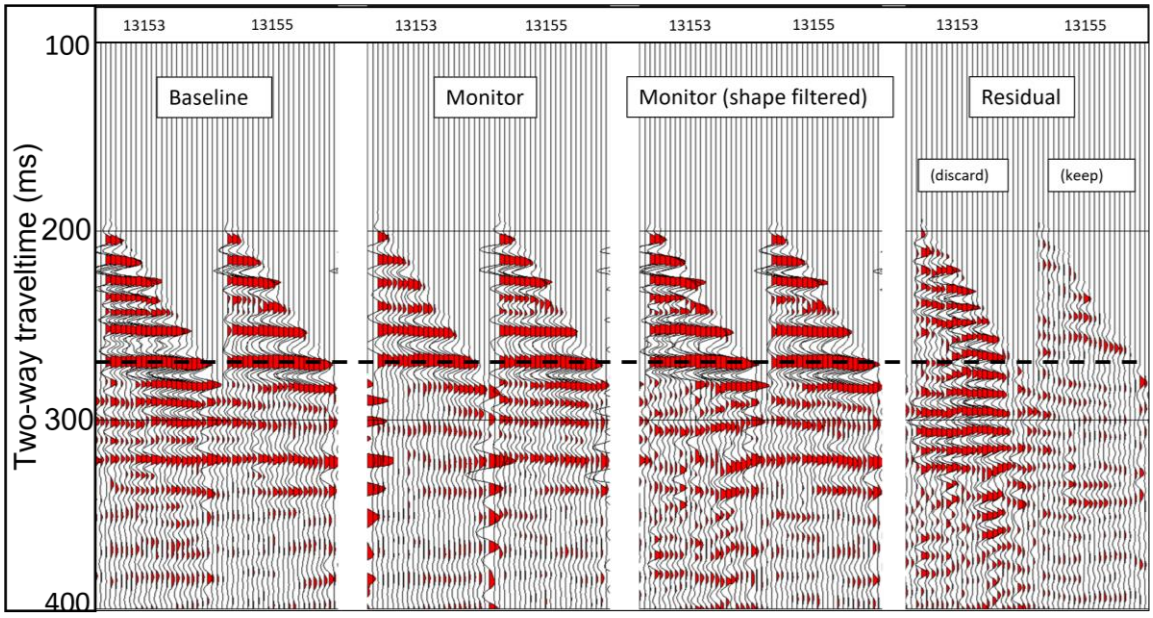

Figure 5.3 Comparison of two shot gathers from 2017May and 2021March25. After shape-filtering, Shot 13153 gathers remain much more dissimilar than Shot 13155, causing significant time-lapse residuals which also manifest post-stack. Dashed line indicates BBRS interval.

and the corresponding time-lapse residuals. In the case of Figure 5.3, the shaping filter is failing to raise up the frequency content of an anomalously low-frequency monitor gather. Anomalously high-frequency monitor gathers caused similar problems. In the 2021Mar25-2017May shaping-filtered time-lapse results, the following poorly matched shots were removed: 13135, 13147, 13153, 13161. The removal of these dissimilar shot gathers significantly improved the stacked result by reducing coherent time-lapse residuals. The removal of those four shots was supported by the NRMS calculation (Figure 5.2). However, the selective removal of shots risked introducing interpreter-bias, by curating the result towards the expected appearance. This method was therefore not satisfactory.

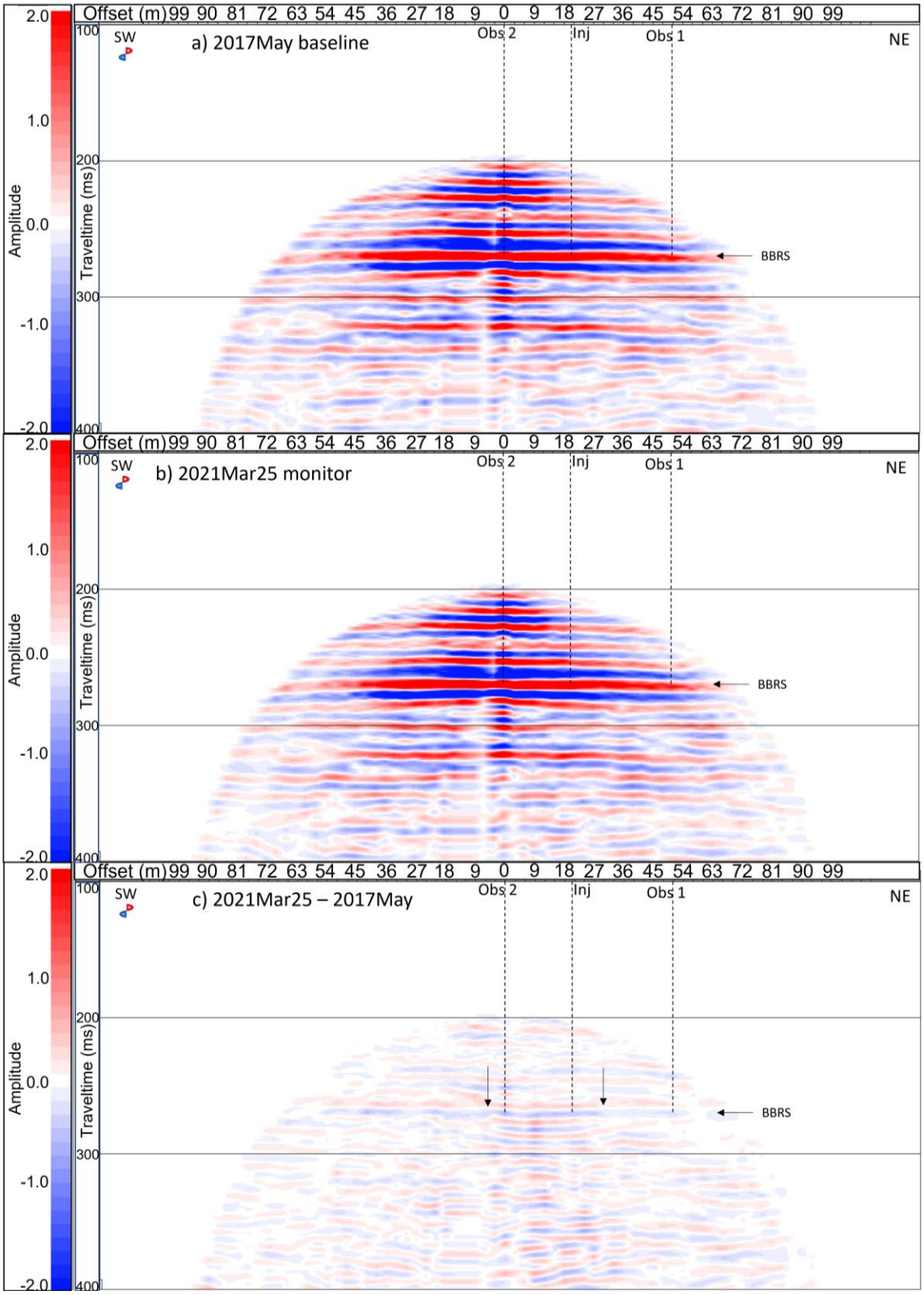

Figure 5.4 Baseline (a) monitor (b) and time-lapse difference (c) for 2021Mar25-2017May datasets, using a shaping filter designed from reflection data. An amplitude anomaly exists between Obs 2 and Injection wells. Interpreted edges of the CO_2 plume are indicated by arrows. The CO_2 anomaly appears weaker than expected due to the amplitude balancing effects of the upgoing shaping filter.

After QCing and removing the worst-matching shots, the shape-filtered shot gathers underwent VSP CDP stacking and subtraction. The best result, from 2021Mar25-2017May, is shown in Figure 5.4. An amplitude anomaly in the BBRS reservoir interval is apparent in Figure 5.4c, extending from the injection well to the Obs 2 geophysics well. As shown in Figures 3.4 & 5.1, it is likely that the CO_2 anomaly has been weakened by the shaping filter and does not stand out as clearly as it should from the background time-lapse residuals. At arrival times following the anomaly, there exist relatively high amplitude residuals where travel-time delay effects should manifest. However, based on forward modeling tests, the travel-time delay effect was expected to be relatively weak after shape-filtering. These later time-lapse residuals may instead be caused by poor cross-equalization. Although the result in Figure 5.4c likely does show amplitude effects from the CO_2 plume, there was enough cause for doubt in the upgoing-designed shaping filter method that more direct cross-equalization was attempted, described in the following sections.

5.4 Shaping filter design: Downgoing arrivals

As described in Chapter 4.2.5, the downgoing direct arrivals can be considered a record of the wavelet, prior to reflection. A shaping filter designed from the downgoing arrivals would therefore have the effect of converting the monitor wavelet to the baseline wavelet, producing very similar monitor and baseline data. Created after wavefield separation, this downgoing shaping filter is not influenced by reflection amplitudes. A downgoing shaping filter should therefore match the filtering effects present in the baseline data's downgoing wavelets, while preserving CO_2 related amplitude changes between baseline and monitor data.

Applying the downgoing shaping filter to the deconvolved upgoing reflection data caused unnecessary problems. Following deconvolution, the amplitudes of the baseline and monitor data were already normalized, as described in Chapter 4.5.2. The downgoing shaping filter however, retained any scalar differences present between the baseline and monitor data. Applying the shaping filter after deconvolution therefore re-scaled the monitor data, requiring a subsequent trace amplitude normalization step. Trace scaling steps were significant sources of error and had been removed from the time-lapse compliant processing workflow, as described in Chapter 4.1. To avoid introducing error with this a trace scaling step, the downgoing shaping filter was instead applied to the raw data.

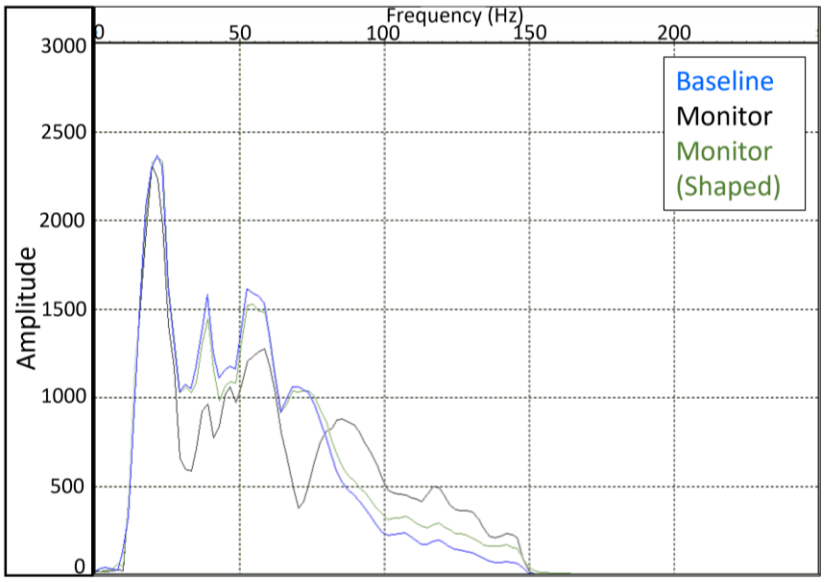

Figure 5.5 Raw shot gather spectra from shot location 13155. The baseline (blue) is more heavily filtered by the near-surface than the monitor (black). The monitor spectrum (black) has been scaled down for visual comparison. The downgoing shaping filter produced a good overall match between the two spectra. Significant amplitude differences remain, particularly above 85Hz.

Figure 5.5 shows the raw shot gather spectrum from shot 13155 from Line 13 2017May and 2021Mar1 datasets. This shot was previously observed in Figure 4.9 to be highly attenuated above 85 Hz in the baseline data, compared to the monitor data. The monitor spectrum was also much higher amplitude overall and was scaled down for the display in Figure 5.5, in order to better compare the amplitudes at different frequencies. The filtered monitor spectrum matches the baseline overall with some minor differences at low frequencies, but noticeably diverges above 85 Hz. This divergence indicates that the shaping filter was not able to adequately match the seasonal near-surface filtering effects in the raw baseline data.

The downgoing shaping filter that produced the result in Figure 5.5 used the same design window and operator length as the deconvolution operator in the main workflow. However, a very small pre-whitening term of 0.05%, rather than 1%, was used for the shaping filter, with the goal of closely fitting the baseline data. While overfitting had been a concern with the upgoing shaping filter due to the inclusion of the BBRS reflection, overfitting of the downgoing shaping filter was not a concern since a close match was being sought. Various pre-whitening terms, design window lengths, and operator lengths were tested for the downgoing shaping filter. No variation of the parameters produced an obvious improvement over the result seen in Figure 5.5. The failure to achieve a nearly perfect fit

between the shaped monitor data and the baseline data is likely a result of the limitations of the least-squares solution to the shaping filter. The least-squares solution is likely dominated by the high amplitudes of the lower frequency bands, and less sensitive to the higher frequency bands. This insensitivity had been expected and was the main motivation for attempting the upgoing shaping filter described in the previous section.

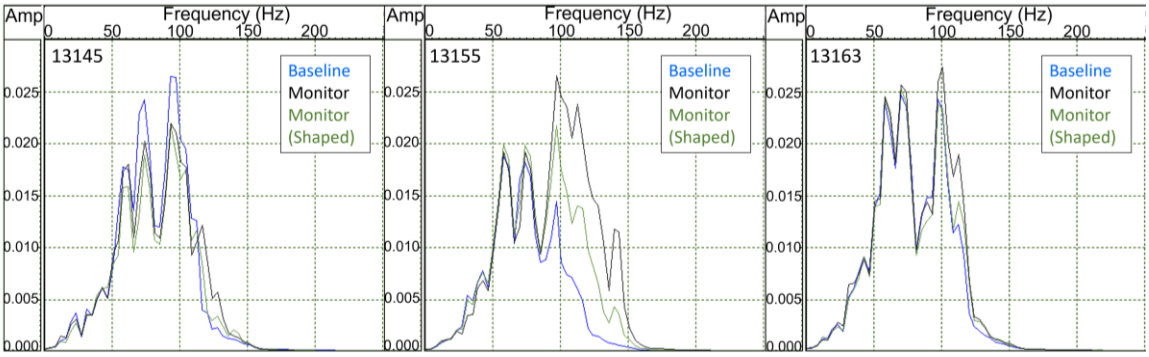

Figure 5.6 Pre-stack shot gather spectra for baseline (blue) monitor (black) and shaping filtered monitor data (green). The inadequate effects of the downgoing shaping filter can be seen in shot 13155 where the high frequency amplitudes remain mismatched.

Figure 5.6 shows spectra from the processed, pre-stack gathers for the same three reference shots seen in previous figures. Similar to Figure 5.1 and the upgoing shaping filter design, the downgoing shaping filter was not able to address the major disparity in bandwidth and amplitude for shot 13155. These spectral differences again caused high frequency residual amplitudes in the time-lapse difference. While disappointing, this result was not surprising. The shaping filter being invertible implies that its filtering effects were reversible during deconvolution. Although, since deconvolution is performed as a matrix operation, the shaping filter is not perfectly removed. Some of its effects remain, causing the partially scaled down amplitudes above 75Hz for shot 13155.

Figure 5.7 shows the 2021Mar1-2017May time-lapse for Line 13, using the downgoing shaping filter method. The CO_2 anomaly is markedly stronger than the upgoing shaping filter result seen in Figure 5.4. However, the display is plagued by high amplitude time-lapse residuals from the inadequate effects of the downgoing shaping filter. Removing the most mismatched shots could reduce these residuals, as described in Chapter 5.3. However, the removal of data and potential for interpretation bias was once again a concern. The goal of cross-equalization was to both preserve CO_2 related amplitude effects while eliminating seasonal differences in near-surface filtering between the baseline and monitor data. From

that perspective, it was concluded that neither the downgoing nor upgoing shaping filter design methods were capable of achieving both goals, and a third method of cross-equalization was devised using shot-dependent high-cut filters.

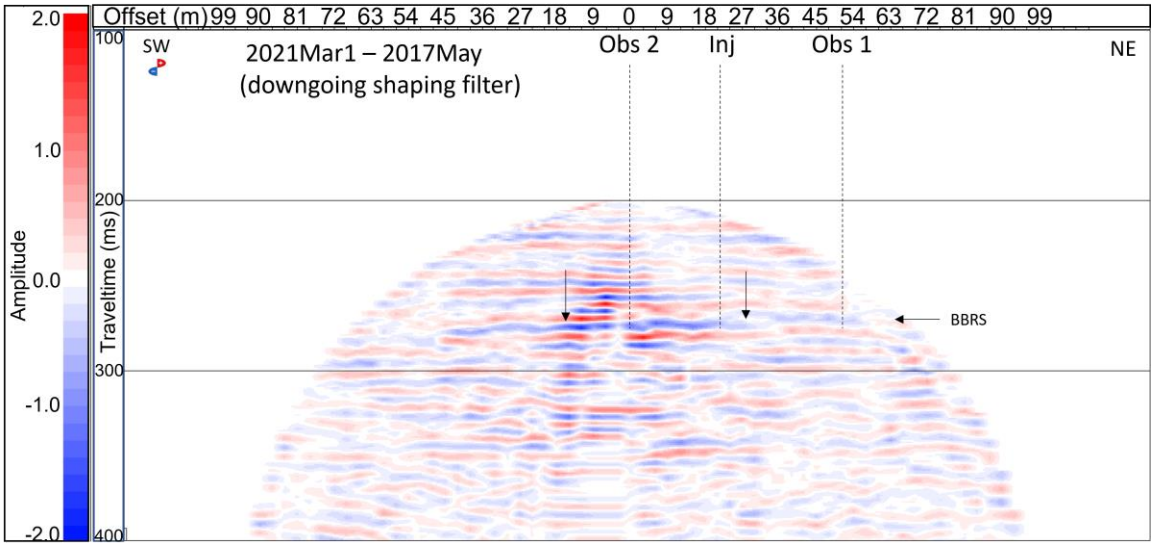

Figure 5.7 Time-lapse difference from the downgoing shaping filter method. Arrows indicate the interpreted edge of the CO_2 anomaly, which is uncertain due to background time-lapse residuals.

5.5 High-cut filtering to match bandwidths

The deleterious effects and inadequacies of the shaping filters led to the idea of simply high-cut filtering the data down to a common bandwidth instead. The 2021Mar1 monitor survey was chosen to first test this method, as none of its shot gathers had lower frequency content than the baseline 2017May, simplifying the filter design process. Shot gathers were inspected individually and high-cut frequencies were chosen. The goal was to trim the spectra at the point where they diverged significantly, leaving only the highest common frequency band where amplitudes appeared to match without obvious unresolved attenuation effects (Figure 5.8). This laborious, brute-force process decreased the overall available frequency content but avoided altering any relative amplitude differences in the remaining bandwidth (Figure 5.8 – 13145). Some shots required no filtering at all, whereas others were grouped into categories with High Pass - High Cut frequencies increasing in increments of 5 Hz or 10 Hz, with a 10 Hz taper. For example: cut-offs of 50 Hz-60 Hz, 60 Hz-70 Hz, 75 Hz-85 Hz, 85 Hz-95 Hz, and 100 Hz-110 Hz were the categories initially determined for the Line 13 2021Mar-2017May time-lapse. The application of a high-cut

filter to match the bandwidths, without otherwise altering the remaining amplitudes, was expected to preserve the CO_2 plume anomaly in the stacked time-lapse difference.

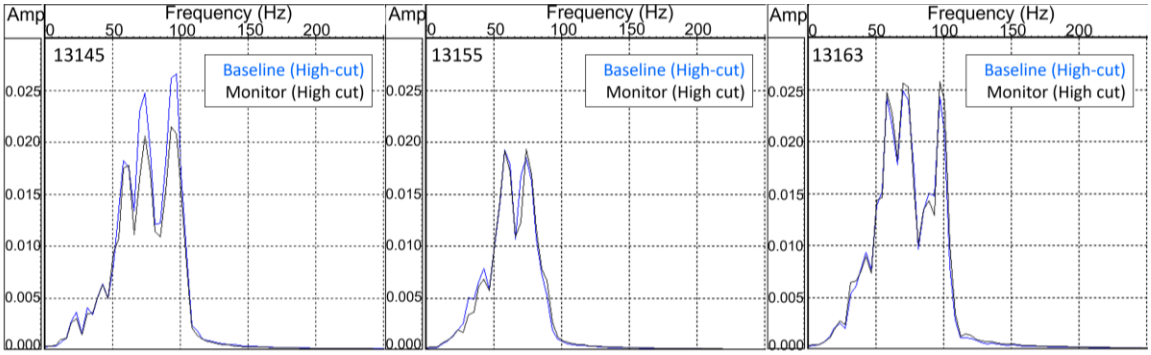

Figure 5.8 Amplitude spectra of shots 13145, 13155, and 13163 after a custom bandpass filter of 5Hz-10Hz-XHz-YHz was applied to each shot. The frequencies X and Y were determined after visual inspection of each shot gather. The result was a common bandwidth with unaltered amplitudes for each baseline & monitor shot gather pair. Identical scaling is applied in each display.

Figure 5.9 shows shot 13145's processed gathers (+tt) with high-cut filters applied. The left panel shows the baseline gather from 2017May. The right panel shows the monitor gather from 2021Mar1 in red, overlying the baseline 2017May gather in black. The two gathers match so closely that the black baseline gather can barely be seen below the red monitor traces. Small amplitude differences are visible at the BBRS interval, where the peak and trough are consistently lower amplitude on the red monitor traces. This pattern matches the expected response to CO_2 saturation seen in synthetic data (Figures 3.3 & 3.4). Other smaller scale differences exist on the display. These lead to time-lapse residuals in the difference between stacked monitor and baseline data.

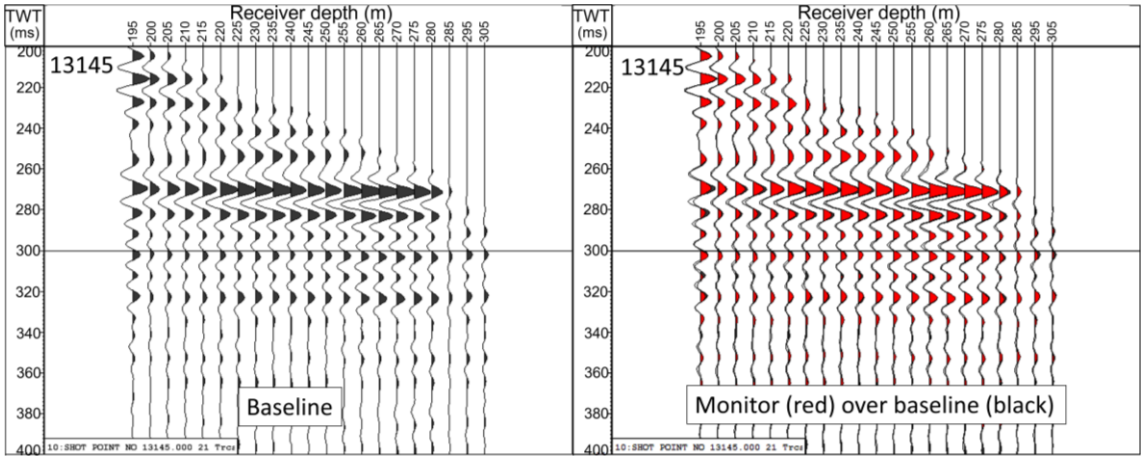

Figure 5.9 Processed gathers (+tt) from shot 13145 with high-cut filters applied. The monitor gather (red) is overlain on the baseline gather (black) on the right panel. Very little difference is evident overall. Consistently lower amplitudes exist in the monitor traces at the BBRS interval.

Shot gather pairs for shots 13155 and 13163 were also found to be highly similar after high-cut filtering. In Figure 5.10, the monitor gathers (red) are again overlain on the baseline gathers (black). Shot 13155 was lower frequency overall, due to the more severe 5-10-75-85 (Hz) filter reducing its high frequency bandwidth more drastically than for the other two example shot gathers. As with shot 13145 in Figure 5.9, the filtered gathers for shots 13155 and 13163 matched very closely. Small-scale differences unrelated to CO_2 saturation can be seen in Figure 5.10, for example: At 300ms on shot 13155, or on traces 295m and 305m for shot 13163. These remaining differences produced both coherent and incoherent time-lapse residuals in the time-lapse difference and are considered background noise. Note that on these displays, the 190m, 290m, and 300m traces have been removed due to noise from dead or malfunctioning traces between surveys.

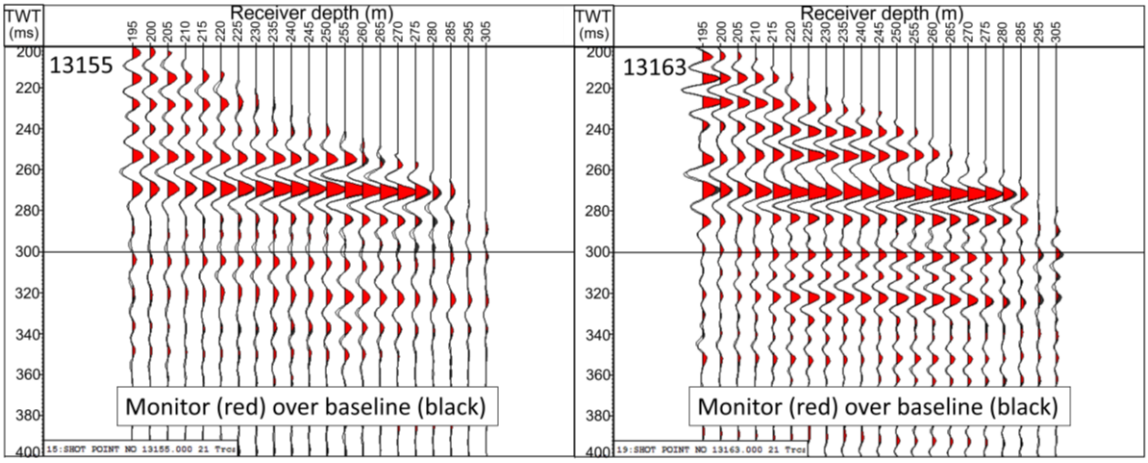

Figure 5.10 Processed gathers (+tt) from shots 13155 and 13163 showing high degrees of similarity after high-cut filtering. Baseline (red) traces are overlain on monitor traces (black). Minor amplitude differences still exist, resulting in time-lapse residuals after stacking and subtraction.

5.6 Time-lapse of stacked results

5.6.1 Line 13 SW-NE stacked results

It is worth noting the general characteristics of the VSP CDP stacks, prior to examining the time-lapse differences. Figure 5.11 shows examples of VSP CDP stacked results from Line 13. These stacked sections were generated with the time-lapse compliant processing workflow described in Chapter 4, with and without high-cut filters applied. The top panels show the 2017May baseline and 2021Mar1 monitor results without high-cut filtering (a & b), and with pre-stack high-cut filters applied (c & d). The unfiltered stacks (a & b) clearly show loss of resolution with increasing source offset from the observation well. Higher

frequency reflections at nearer CDP offsets appear pinched-out at father offsets. Away from the observation well, each CDP bin stacked reflected waves from progressively farther-offset shots with longer, more attenuated raypaths. This effect is worth noting, as it can lead to interpretation mistakes if not kept in mind by the interpreter. By comparison, surface seismic reflection bins tend to have a more balanced stack of near and far offset shots. This effect is still present, though less prominent, in the high-cut filtered results in Figure 5.11c & 5.8d. In addition to attenuation effects, reduced fold at far offset CDPs contributes to the uneven amplitude and frequency distribution. It should be noted that no f-k filter or median filter has been applied to clean up the appearance of the pre-stack data, in the interest of preserving amplitudes at the BBRS reservoir interval.

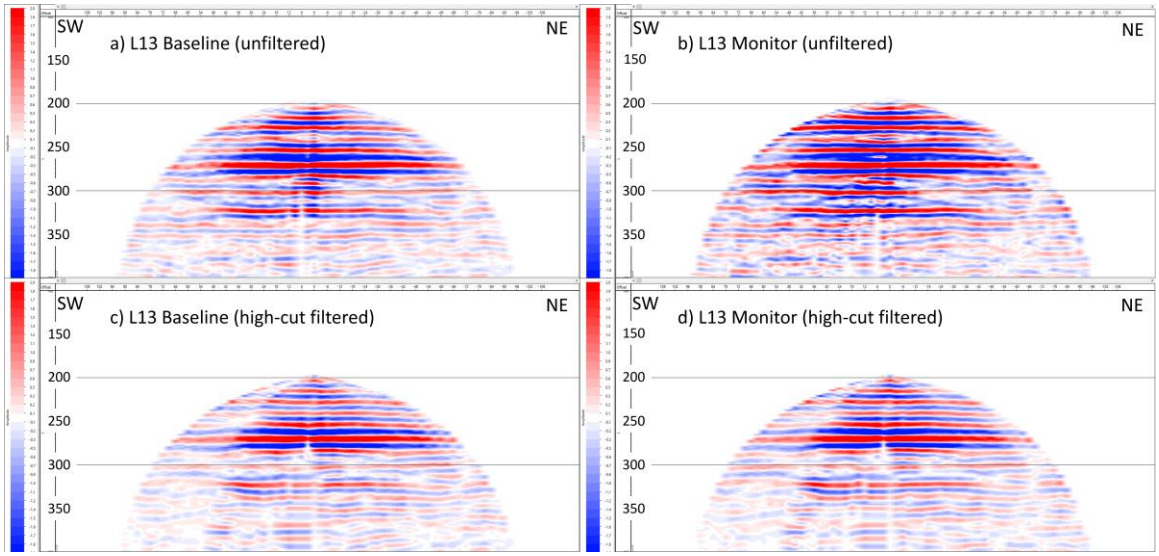

Figure 5.11 Geophone VSP CDP stacks of Line 13 baseline (2017May) and monitor (2021Mar1) following time-lapse compliant processing, with and without pre-stack high-cut filters applied. Vertical axes are two-way travel time, horizontal axes are CDP offset.

In Figure 5.11a, it is apparent that the south-west shots suffered greater attenuation than the north-east shots, particularly in the baseline survey. This is exacerbated in the high-cut filtered results, as the need for harsher filters caused a visible demarcation between low and medium frequency CDPs, outlining the edge of a less-filtered shot gather. Fortunately, the more severe attenuation in the south-west did not cause problems for these time-lapse results other than a visually distracting amplitude decrease within the VSP CDP stacked section. This could be partly mitigated in the future by substituting shots from the 2019Aug survey into the baseline. Such a hybrid baseline survey for line 13 will also allow for 10m shot spacing in the south-west, improving the signal strength.

5.6.2 Line 13 SW-NE time-lapse difference

The Line 13 time-lapse difference from VSP CDP stacked data are shown in Figure 5.12. Three time-lapse results are displayed using 2017May as a baseline for each of three monitor surveys: 2019Aug (panel a), 2021Mar1 (panel b), and 2021Mar25 (panel c). These results used the pre-stack high-cut filtering method to remove the seasonally variable near-surface filtering effects. A set of high-cut filters was designed shot-by-shot for each monitor survey by comparison with the baseline.

Figure 5.12a shows the 2019Aug-2017May time-lapse result. The three displays have identical horizontal scaling, the 2019Aug survey had reduced coverage due to more limited shot offsets (180 m instead of 250 m). There appears to be an anomaly standing out from the background time-lapse residuals between the Injection well (Inj) and geophysics observation well (Obs 2) in Figure 5.12a. Arrows indicate the interpreted plume edge. However, the weaker anomaly would have been difficult to identify with confidence without knowing where to expect it, and without having the 2021Mar1 and 2021Mar25 time-lapse results against which to compare it. Therefore, the 15 t CO_2 plume can be considered to have not unequivocally reached the detection threshold.

Compared to the uncertain results from shaping filter cross-equalization (Figure 5.4), an unequivocal amplitude anomaly exists in the high-cut filtered results in Figure 5.12b & c. This field data result matches very well with the modeled VSP time-lapse anomaly (Figure 3.4). The anomaly is a strong trough-peak succession with opposite side-lobe amplitudes at the BBRS interval. The travel-time delay anomaly may be visible but is not very strong amidst the background time-lapse residuals. Shot by shot inspection and a drop-out analysis of VSP CDP mapped gathers appeared to show contributions to the amplitude anomaly from most of the north-east shots. This increased confidence in the interpretation of the CO_2 plume. A conservative interpretation of the edges of the plume is shown with arrows in Figure 5.12. By March 2021, the 33 t plume appeared to extend at least 15m NE & 33m SW of the injection well. The plume likely extends beyond the arrows, but lateral resolution is limited by the 3m binning as well as the diminishing CO_2 saturation and velocity effects of the plume, away from the injection well. An interpreted lateral plume extent of 45 m – 51 m is in line with the 50 m expectations from reservoir modeling (Figure 3.4), except for its asymmetric spread towards the south-west.

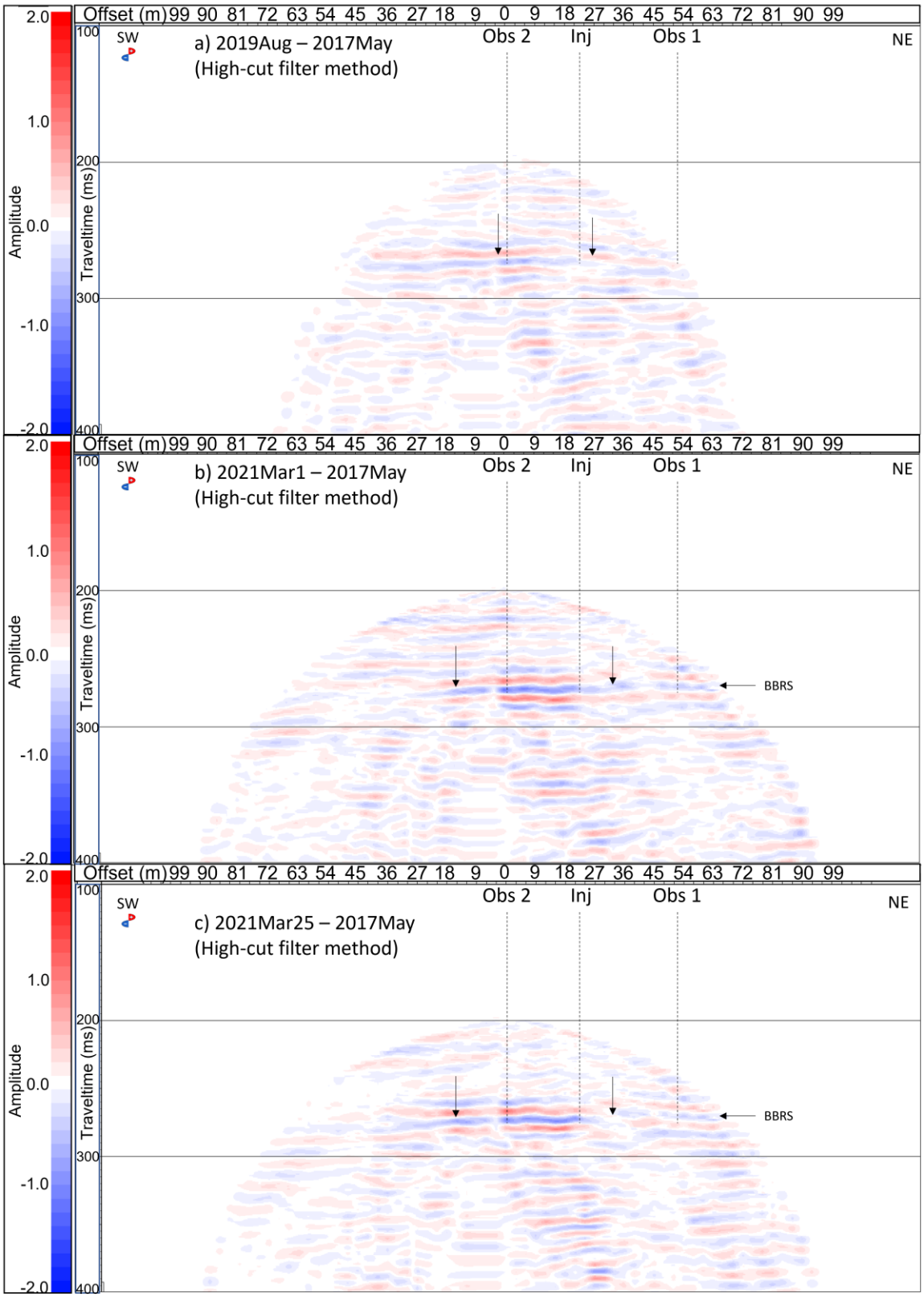

Figure 5.12 Line 13 VSP time-lapse results. The 15t CO_2 plume is not clearly above the detection threshold (a). Both 2021Mar monitor surveys (b & c) detect the plume. Arrows indicate plume edge.

From shot to shot, there was little spatial pattern to the pre-stack high-cut filtering. As a result, the frequency content and overall amplitude decreased erratically with shot offset rather than gradually, causing the wavy appearance of the anomaly in Figure 5.12b & c. The exception was the high levels of attenuation in the south-west far offset shots previously noted for the 2017May data (Figures 5.8c & d).

Despite major differences in surface conditions between 2021Mar1 and 2021Mar25 acquisition, the very similar appearance of the CO_2 anomalies, adds further confidence to the time-lapse compliant workflow and the bandwidth matching of the high-cut filtering method of cross-equalization. In the following sections, this process was successfully repeated for Lines 7 and 15.

5.6.3 Line 15 SE-NW

Line 15 runs south-east to north-west, perpendicular to Line 13, with 10 m shot spacing. Unfortunately, only data from August 2019 was available to act as a baseline with shot locations identical to the 2021 monitor data. With a smaller 18t difference in injected CO_2 and a smaller relative change in CO_2 saturation, the 2021Mar1-2019Aug time-lapse was therefore expected to show lower-magnitude effects than Lines 13 and 7.

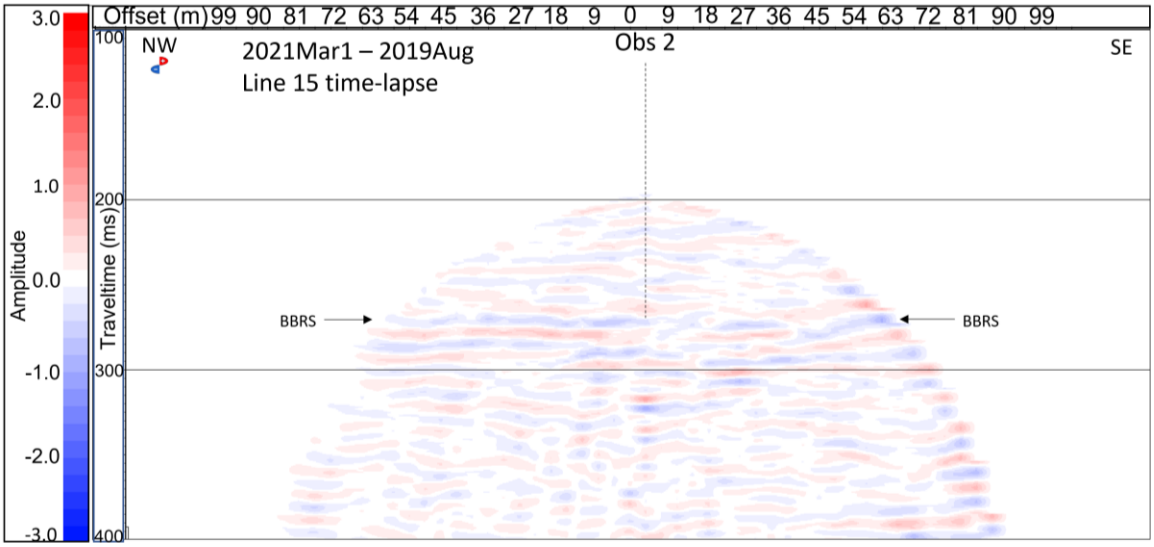

Figure 5.13 VSP CDP difference from a relatively short 1.5 year 2021Mar1-2019 time-lapse. Reservoir (BBRS) and observation well location (Obs2) indicated. No strong anomaly is present.

Figure 5.13 shows Line 15's shorter ~1.5 year time-lapse result, with no strong CO_2 anomalies evident. Based on the Line 13 results of Figure 5.12, CO_2 was expected to have crossed under Line 15 prior to the 2019Aug monitor survey. This was neither confirmed

nor disproven by the ambiguous result in Figure 5.13. Line 15 is expected to better show the plume in future monitor surveys after a sufficient increase in CO_2 saturation has occurred since 2019Aug. Compared to Figure 5.12, the amplitude range in the display was increased from 2.0 to 3.0 in Figure 5.13, due to higher overall fold from 10m shot spacing.

5.6.4 Line 7 North

Line 7 runs north-south from the Obs 2 well with 10 m shot spacing. Only the northern half of Line 7 was available for time-lapse for 2021Mar1 data. This north walk-away line was shot in July 2017 (2017Jul), September 2018 (2018Sep), and March 2021 (2021Mar1). The 2018 dataset allowed for validation of results by producing three time-lapse differences: 2018Sep-2017Jul, 2021Mar1-2017Jul, and 2021Mar1-2018Sep. As with Line 13, unique sets of high-cut filters were chosen for each of the Line 7 baseline-monitor pairs.

Figure 5.14a shows the 1 year time-lapse difference with no apparent seismic anomaly. This result was encouraging, as a 1 year, 7-tonne CO_2 plume would not have permeated far enough from the injection well to be detected on Line 7. Figure 5.14b shows the 33t CO_2 time-lapse result from 2021Mar1-2017Jul. A pronounced seismic anomaly is evident, possibly extending as far as 50m to the north. As with the Line 13 result, this anomaly is a trough-peak sequence at the BBRS interval, with side-lobe energy and a possible travel-time delay effect below. Figure 5.14c shows the 2021Mar1-2018Sep time-lapse difference, which is similar to the 2021Mar1-2017Jul result. Compared to the 2017Jul baseline, the 2018Sep survey was missing shots due to recording problems. In particular, a sequence of 5 missing mid-offset shots caused reduced fold and amplitude in the 30m-39m CDP bins. While 2018Sep was therefore a poorer baseline survey than 2017Jul, it allowed for validation of the results from the 2021Mar1-2017Jul time-lapse. As with the Line 15 display in Figure 5.13, the amplitude range in Figure 5.14 was set at -3.0 to 3.0 to account for higher overall fold from 10m shot spacing, while preserving a similarly bright display as Figure 5.12. The consistency between the 3 time-lapse results in Figure 5.14 was considered sufficient validation of the interpretation. The 2021Mar25 time-lapse analysis has not yet been performed, but is expected to yield an equivalent time-lapse difference. With a broader range of available shots, performing the Line 7 time-lapse for 2021Mar25-2017Jul should help delineate the CO_2 plume to the south of the Obs 2 well, in the future.

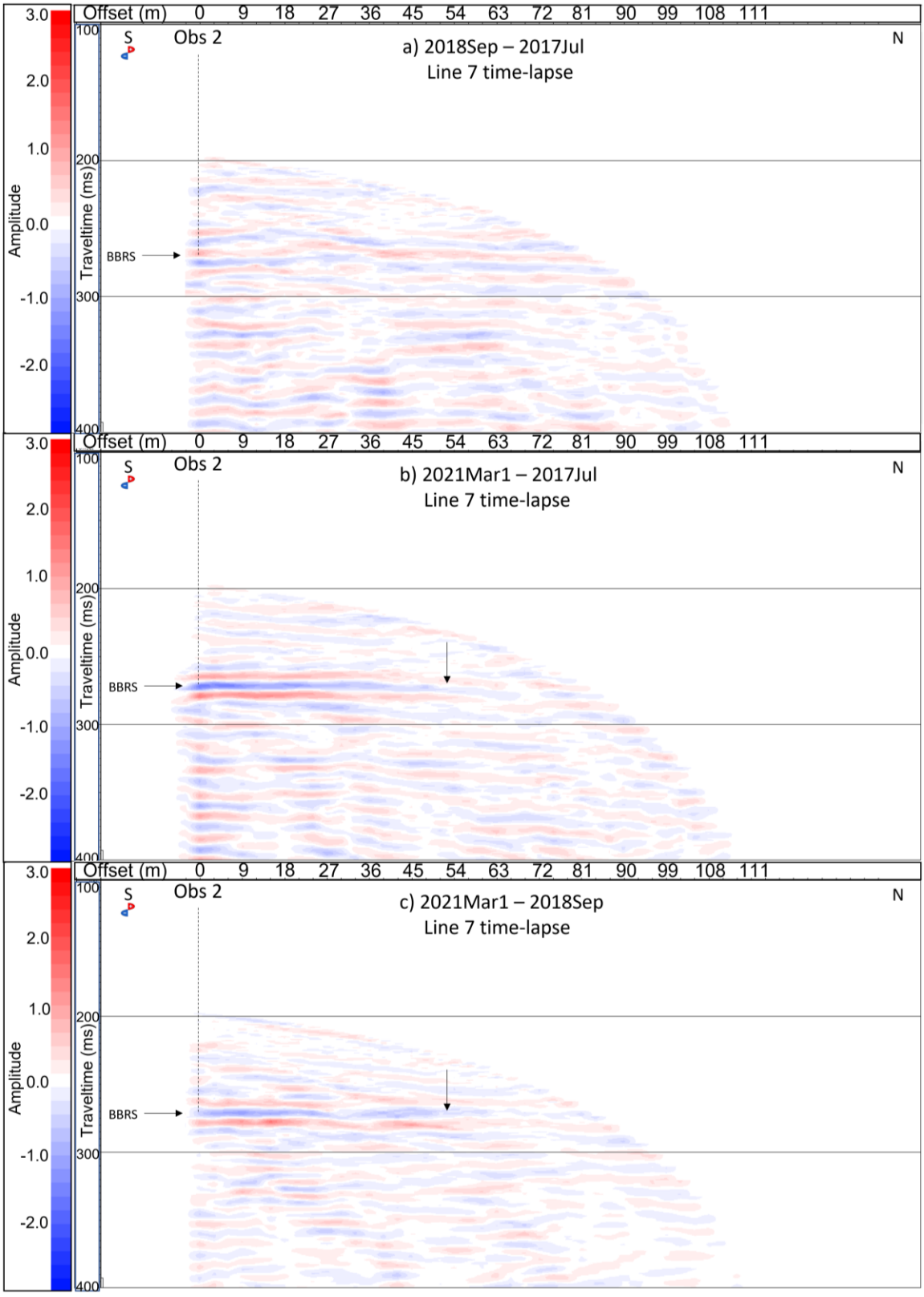

Figure 5.14 Line 7 VSP time-lapse results from a) 2018Sep-2017Jul, b) 2021Mar1-2017Jul, and c) 2021Mar1-2018Sep. Arrows indicate the reservoir and probable maximum extent of the plume.

5.7 Normalized root-mean-square results

Normalized Root-Mean-Square (NRMS) was again used as a diagnostic tool to quantify differences between time-lapse datasets. Table 4 lists the NRMS values for the various final time-lapse results obtained. NRMS was calculated over two time-windows: Long (150ms-400ms) and short (250ms-290ms). The NRMS for the noiseless VSP forward model was 8% over the long window. This increased to 13% over a shorter window, where the BBRS anomaly causes greater relative difference. The model NRMS values establish best-case-scenario NRMS values for the field data. The field data follow the opposite trend, with higher NRMS over the longer window due to cumulative effects of background time-lapse residuals. Consistently lower NRMS values were obtained for the datasets showing weak or undetected CO_2 anomalies. Higher NRMS values were obtained from the time-lapse results showing strong CO_2 anomalies. The exception to this trend was the Line 7 2018Sep-2017Jul result. In future time-lapse surveys, a trend of increasing NRMS in the 40ms window is expected, as the plume grows laterally and vertically. Although NRMS had been useful as a diagnostic tool during development the time-lapse compliant VSP workflow, it is not expected to be employed as a direct interpretation tool for the CO_2 plume itself.

Table 4. NRMS values from time-lapse VSPs.

Method	VSP line	Time-lapse	CO_2 effect	Window	NRMS
Forward model	13	4-year 29t plume	Strong (noise free)	150ms-400ms	8%
				250ms-290ms	13%
Shaping filter	13	2019Aug-2017May	Weak	150ms-400ms	14%
				250ms-290ms	9%
Shaping filter	13	2021Mar25-2017May	Weak	150ms-400ms	15%
				250ms-290ms	9%
High-cut filter	13	2019Aug-2017May	Weak	150ms-400ms	15%
				250ms-290ms	10%
High-cut filter	13	2021Mar1-2017May	Strong	150ms-400ms	20%
				250ms-290ms	15%
High-cut filter	13	2021Mar25-2017May	Strong	150ms-400ms	19%
				250ms-290ms	14%
High-cut filter	15	2021Mar1-2019Aug	Weak	150ms-400ms	15%
				250ms-290ms	10%
High-cut filter	7	2018Sep-2017Jul	None	150ms-400ms	21%
				250ms-290ms	13%
High-cut filter	7	2021Mar1-2017Jul	Strong	150ms-400ms	25%
				250ms-290ms	18%
High-cut filter	7	2021Mar1-2018Sep	Strong	150ms-400ms	22%
				250ms-290ms	18%

CHAPTER 6 - DAS TIME-LAPSE PROCESSING AND RESULTS

6.1 DAS data preparation

6.1.1 DAS layout at CaMI.FRS

CaMI.FRS hosts a permanently installed 5km loop for Distributed Acoustic Sensing (DAS), as shown in Figure 6.1. This loop consists of both straight and helically-wound fiber-optic cables (Lawton et al., 2017). As described by Gordon (2019), the DAS record

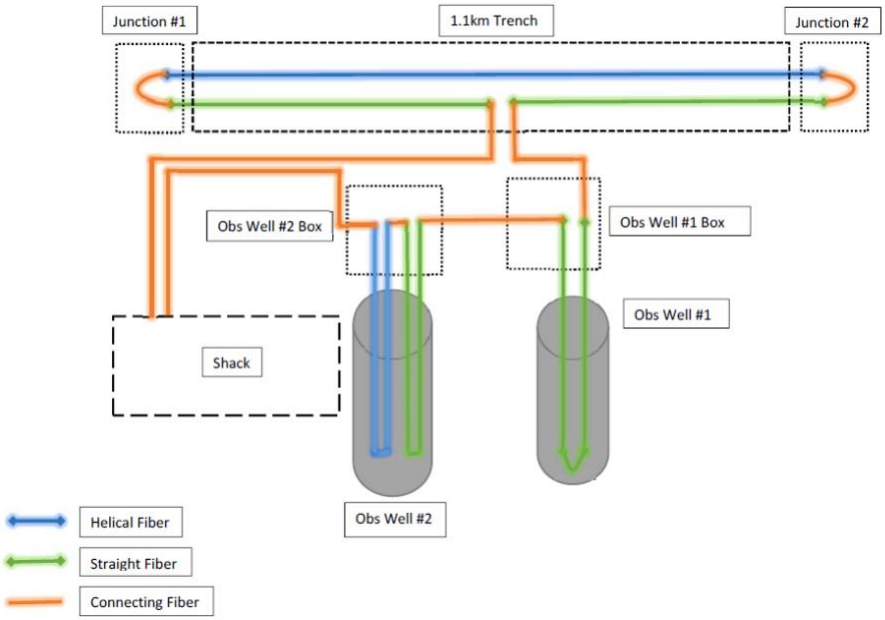

Figure 6.1 Schematic of DAS surface and borehole installation at CaMI.FRS, adapted from Lawton et al. (2017).

for the desired cable section must be cut-out for processing from a large 5-km long DAS seismic record. The 5km DAS datasets are large, on the order of 40MB to 160MB per shot and 1GB to 5GB per walk-away survey. Removal of the desired segment not only simplifies processing but also reduces burden on computer memory and computational intensity during processing and testing. Observations and results from the straight-DAS fiber sections in Obs 2 are discussed in the following sections, as the 1-component time-lapse workflow described in Chapter 4 could be applied directly, with minimal alterations to parameters. However, compared to geophone data, several additional steps were required to prepare the DAS VSP data for processing (Figure 6.2). Processing the straight fiber DAS data in Obs 2 posed fewer processing challenges for time-lapse than the helical-fiber and was the natural first step in transitioning from geophone to DAS.

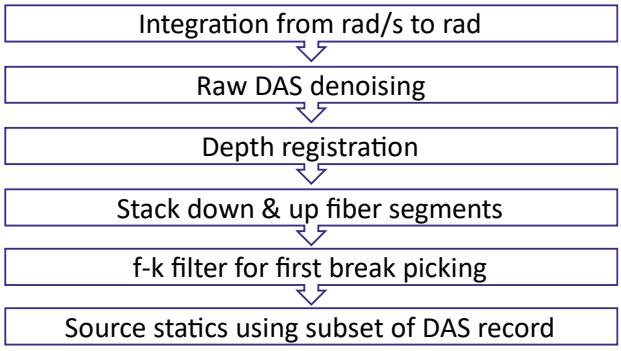

Figure 6.2 DAS-specific data preparation steps performed prior to VSP time lapse processing.

6.1.2 Time-integration

Two baseline and two monitor DAS surveys were processed for time-lapse analysis of Lines 7 and 13 in an attempt to replicate the geophone results. These datasets are listed in Table 5. While the Silixa interrogator used in 2017 output its data in radian-rate (rad/s), the OptaSense interrogator used in 2021 output in radians (rad). The data were made equivalent by integrating the Silixa data with respect to time. Rather than differentiate the OptaSense data, integrating the Silixa data was preferred. This rendered the data more comparable to geophone data (Daley et al., 2016) while also acting to reduce high-frequency-noise afflicting the 2017 datasets. Integration was applied to a 2018Sep MEMS accelerometer data as well, so that all geophone, DAS, and accelerometer datasets could be visually compared. Integration was performed in the frequency domain rather than in time, using VISTA software's integration function. This amounted to dividing each frequency component f by a factor of $(i2\pi f)$.

Table 5. DAS datasets processed for VSP time-lapse analysis

Line #	Orientation	Survey Date	Available shot offsets (m)	Channel spacing (m)	Gauge Length (m)	Output unit	Data quality assessment
13 (baseline)	SW-NE	2017May	+/-250	0.25	10	radians/s	Poor
13 (monitor)	SW-NE	2021Mar1	+/-250	1.003	7	radians	Good
7 (baseline)	N	2017Oct	+/- 160	0.25	10	radians/s	Good
7 (monitor)	N	2021Mar1	250 North only	1.003	7	radians	Good

6.1.3 Noise assessment

The various raw DAS datasets exhibited different levels of noise. Despite using the same Silixa interrogator with the same gauge length (10 m) and output trace spacing (0.25 m), the 2017May baseline from Line 13 had much poorer data quality than the 2017Oct baseline for Line 7. The 2021 monitor data used a gauge length of 7 m, output trace spacing

of 1 m, and was of good overall quality (Table 5). DAS data often contain correlated or coherent noise across multiple traces (Olofsson and Martinez, 2017). Figure 6.3 shows examples of DAS-specific noise present from four time-lapse DAS datasets from CaMI.FRS. The different noise levels and noise types were expected to be significant factors in the time-lapse analysis, particularly for the noisy 2017May Line 13 data.

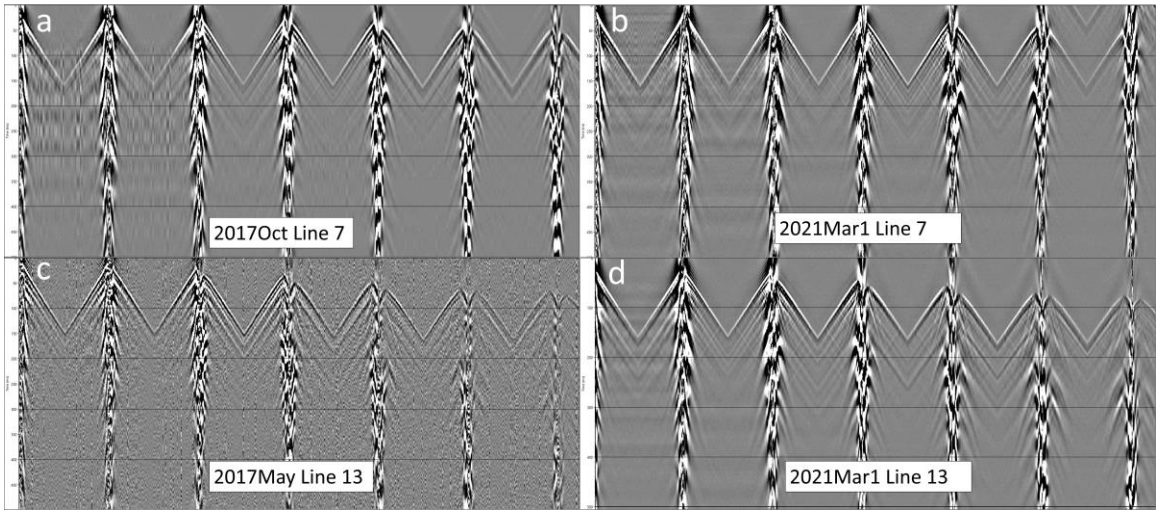

Figure 6.3 Series of 6 raw show gathers from Line 7 and 13 baseline and monitor DAS data. Line 7 had similarly moderate to low noise noise levels from different interrogators (panels a & b). Line 13's baseline had high noise levels across all shots. The 2021Mar1 Line 13 and 7 monitor data used the same interrogator and had the lowest noise levels overall, with clearly visible upgoing P-wave reflections.

Figure 6.4 zooms in to show 4 individual shot gathers, in the same order as Figure 6.3. Olofsson and Martinez (2017) provide a good overview of the common types of instrument noise typical for DAS data, some of which are evident in Figure 6.4. Panels a and b show checkerboard noise of low (a) and high (b) spatial and temporal frequency, respectively. Panel c shows a very noisy shot record, dominated by many high amplitude traces and a more widespread background noise across all traces. Panel d shows a relatively clean shot record with mainly low-amplitude horizontal banding. This "common noise" is caused by vibrations affecting the interrogator unit (Olofsson and Martinez, 2017). Close inspection shows some trace-to-trace noise and amplitude variation on all gathers, even in Figure 6.4d. The V-shape of the direct arrivals in Figures 6.3 and 6.4 are a result of the DAS fiber going down and then looping back up the wellbore (Figure 6.1). The downgoing and upgoing fiber segments were separated at the midpoint, and then stacked to improve SNR and simplify processing (Gordon, 2019). A de-noising process was applied prior to stacking

the two fiber segments. This was mainly done to avoid exacerbating the high noise levels in the 2017May dataset (Figure 6.4c), but benefitted the other DAS datasets as well. Stacking anomalously high-amplitude traces with their lower-amplitude counterparts effectively doubled the noise content in a shot gather. To avoid compounding the noise problems, both conservative and aggressive de-noising methods were tested.

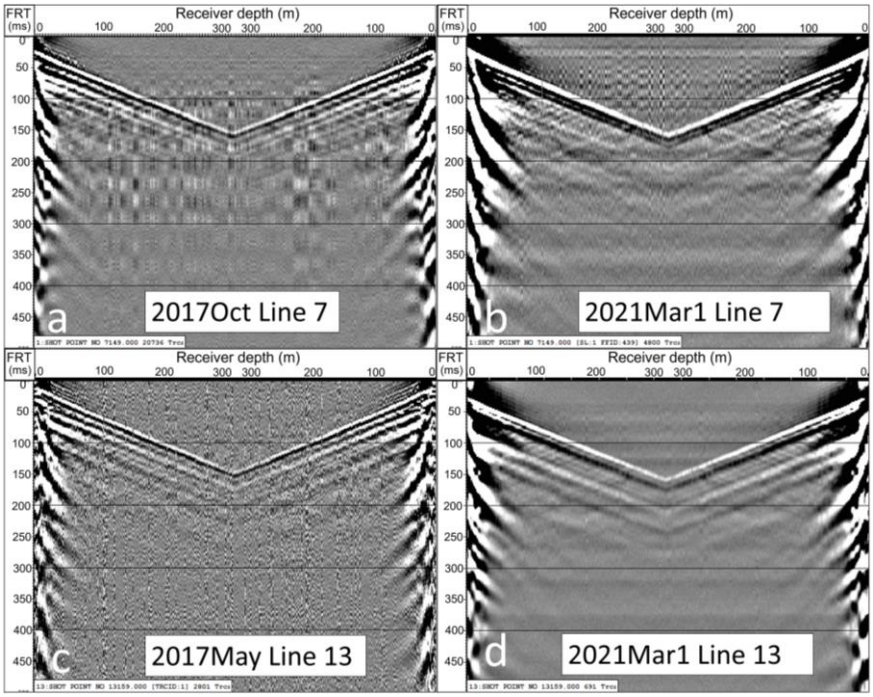

Figure 6.4 Examples of noise in raw DAS records. Panels a, b, and c show low to high spatial frequency noise and checkerboard noise affecting raw traces, while d is relatively clean. Panels b and d show low-amplitude horizontal striping across all traces.

6.1.4 Raw DAS de-noising: Conservative

Noise of high-spatial frequency, such as in Figure 6.4 b & c, can be partly mitigated by median filtering (Bakku, 2015; Li et al., 2015). An amplitude threshold step was also tested, in which traces above a threshold were set to zero prior to median filtering (Li et al., 2015). However, with the Line 13 2017May dataset in particular, an amplitude threshold step zeroed too many traces to be practical. Instead, the median filter was applied on its own.

After trial-and-error testing, a 3 m or 3.25 m median filter was chosen (Figure 6.5). For example, with trace spacing $\Delta z = 0.25$ m, a 13-point median filter was used. For 1 m trace spacing, a 3-point filter was used. This filter size visually appeared to provide the best trade-off between de-noising while avoiding unnecessary smoothing. A much wider median filter window would be needed to address the noise of low to medium spatial

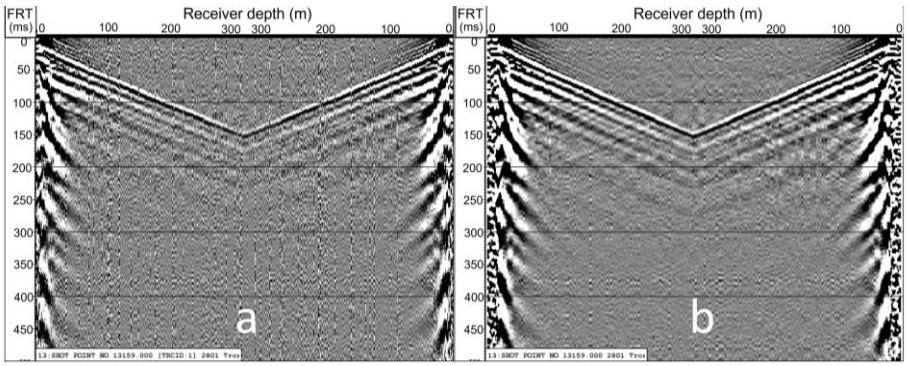

Figure 6.5 Noisy shot record from Line 13 2017May, before (a) and after (b) a 3.25m, 13 trace median filter intended to remove high frequency noise and anomalous trace amplitudes.

frequency, for example the checkerboard noise seen in Figure 6.4a & b. Keeping the median filter window under 5m was also intended to avoid spatially smoothing the data beyond the geophone data's 5m spatial sampling. This was thought to preserve comparison potential between DAS and geophone data. The remaining noise was expected to stack out or be removed by the existing bandpass and f-k filtering steps in the VSP processing workflow described in Chapter 4. It was originally expected that any remaining high amplitude traces would be adequately scaled down by the deconvolution step. However, unsatisfactory results motivated the development of a more aggressive de-noising process.

6.1.5 Raw DAS de-noising: Aggressive

To more fully remove the various types of low and high frequency instrument noise visible in Figure 6.4, the aggressive de-noising process first applied an f-k filter to remove the horizontal and vertical coherent noise (Figure 6.6). This also removed most of the random noise in the shot records. The f-k filter was followed by a 3 m median filter. A RMS trace amplitude normalization step was then applied to each trace with a 0 ms-1000 ms design window. Trace amplitude scaling had been specifically avoided when developing the time-lapse compliant workflow (Chapter 4). However, this trace normalization of the raw data was necessary to reduce the remaining low to medium spatial frequency variability in trace amplitude that survived the 3m median filter. The 1000 ms RMS amplitude design window gave confidence that the BBRS reservoir reflection would not significantly influence the trace amplitude normalization. The RMS normalization was, however, dominated by the first arrivals. Attempting to exclude the first arrivals and the BBRS interval, for example with a window of 300 ms-1000 ms, appeared to cause more harm than good. The RMS normalized trace amplitudes were too unstable when based

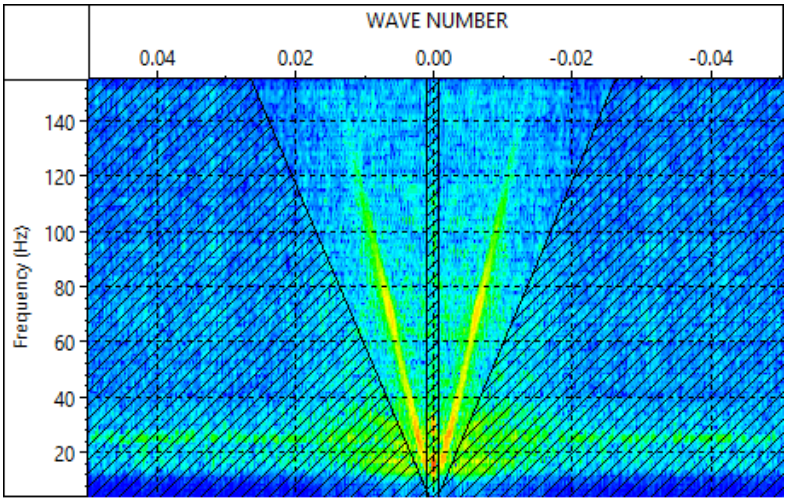

Figure 6.6 An aggressive f-k filter applied to remove much of the noise from the raw DAS record.

solely on noisier, deeper data. Figure 6.7 shows the effects of the more aggressive de-noising method. Most of the random and coherent noise has been removed, though some very low frequency checkerboard noise remains in panel b. The high amplitude traces have been mitigated to a large extent in panel d. In this case, most non-P-wave signal has also been removed, although S-waves could be preserved with a more precise f-k filter design.

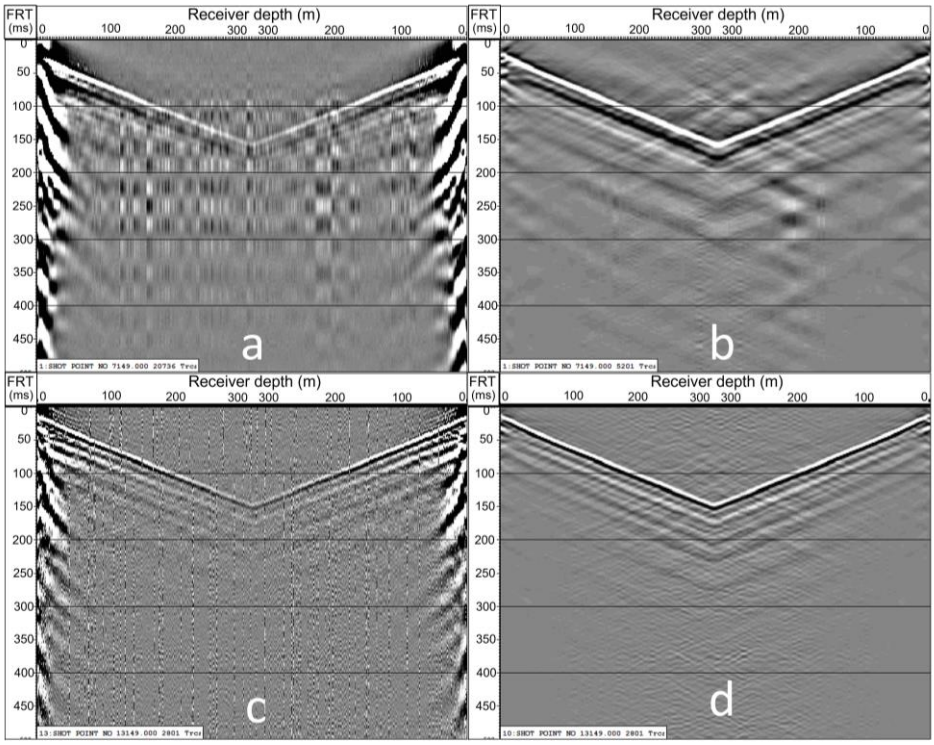

Figure 6.7 Aggressive de-noising of raw DAS data using f-k filter, median filter, and RMS trace normalization. Most random and coherent noise and high amplitude traces have been mitigated. The deeper first arrival amplitudes have been unavoidably scaled up in the process.

6.1.6 Comparison of de-noising methods

A calculation of signal-to-noise ratio (SNR) was performed on raw DAS shot gathers before and after de-noising, which was then compared to a geophone gather. For comparison purposes, the shot gather was limited to 190 m – 305 m. The signal RMS amplitude was calculated from a 20 ms window around the first arrivals, which had been flattened (-tt) to a datum of 100 ms (Figure 6.8). Noise RMS amplitude was calculated

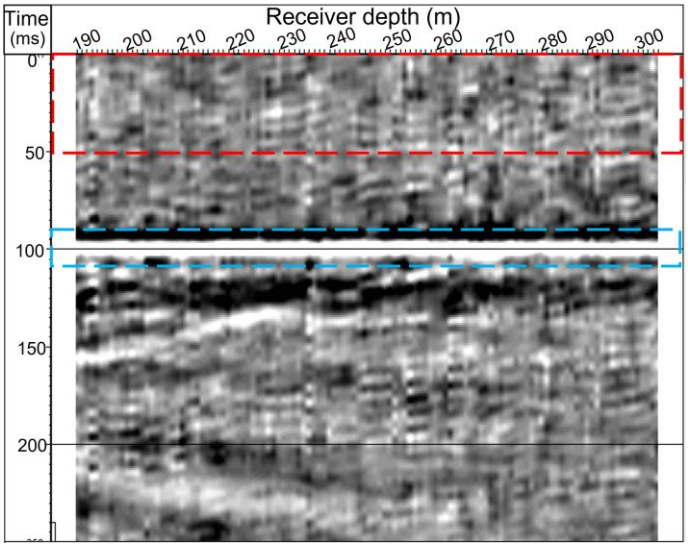

Figure 6.8 Shot 13165 gather, after conservative de-noising with a 3 m median filter, flattened on the direct arrivals (-tt) for calculation of SNR. A 20 ms window around the direct arrivals gave the RMS signal amplitude (blue box). A 50 ms window above the first arrivals gave the RMS noise amplitude (red box).

using a 50 ms window from before the first arrival times. Table 6 lists the resulting SNR values for 2017 baseline and 2021 monitor data for a mid-offset shot (160 m). The raw DAS gathers from the higher quality datasets had SNR values of 6.2 to 7.2, while the noisiest baseline shot from 2017May Line 13 produced a SNR of only 1.1 with this method of calculation. The SNR values improved progressively with the conservative and aggressive de-noising methods but did not reach the SNR of the geophone data.

Table 6. SNR of raw and de-noised DAS gathers compared to geophone equivalents.

	Shot 13165 SNR		Shot 7165 SNR	
Data	2017	2021	2017	2021
Raw DAS	1.1	7.2	6.2	6.8
Conservatively de-noised DAS	4.8	18	12	15
Aggressively de-noised DAS	15	34	20	25
Geophone	26	48	23	41

Figure 6.9 illustrates the motivation for the more aggressive method of de-noising by comparing DAS shot gathers limited to the same depth range as geophone gathers. The processed TWT pre-stack gathers in Figure 6.9 are arranged from left to right as: baseline, monitor, and the difference from direct subtraction. From top to bottom: de-noising method 1 (conservative), method 2 (aggressive), and a reference geophone gather are compared.

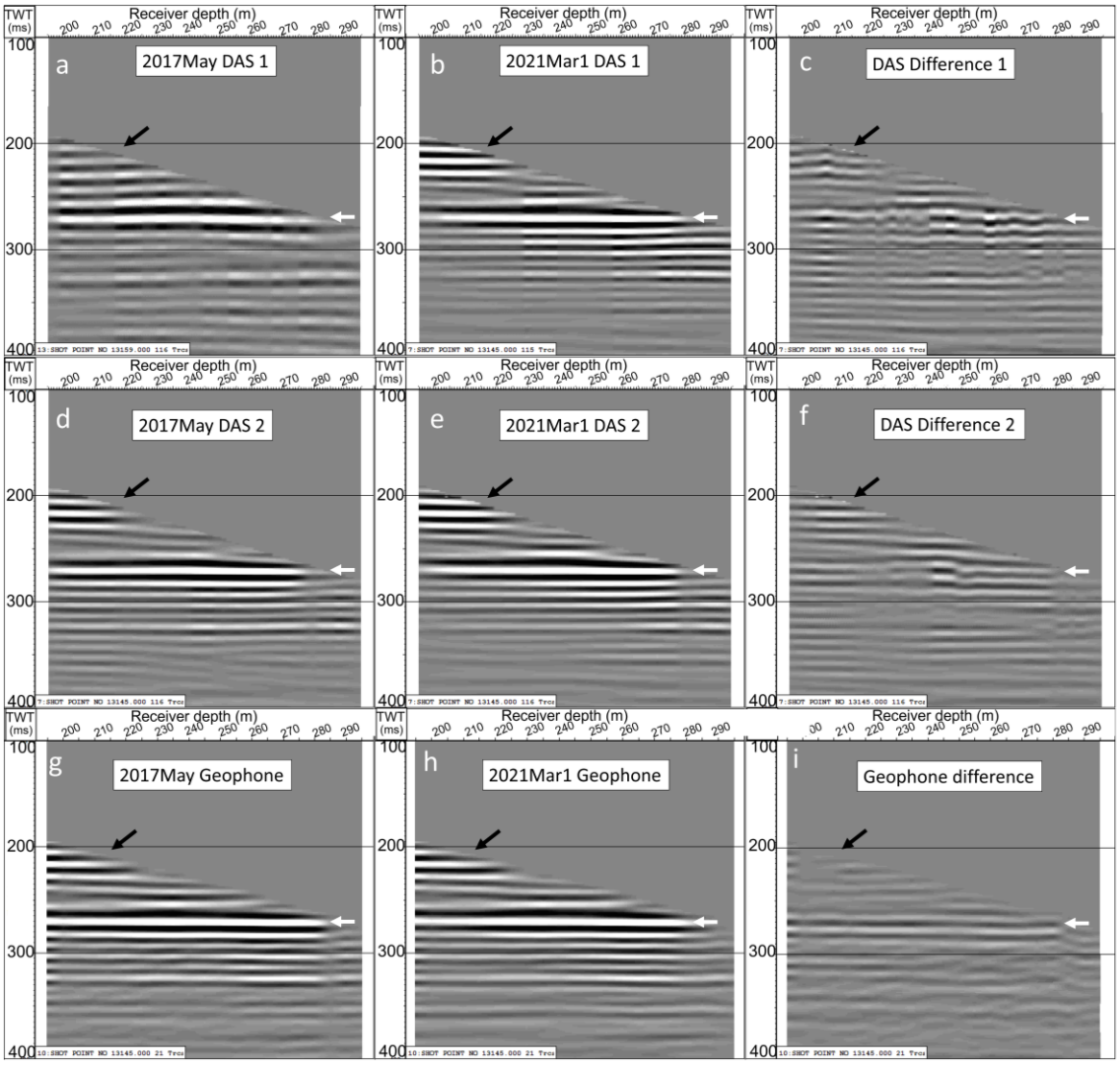

Figure 6.9 The downstream effects of de-noising on pre-stack shot gathers. From left to right: Baseline, Monitor, and difference. From top to bottom, conservative method 1 (a-c), aggressive method 2 (d-f), and reference shot gather from geophones (g-i). DAS trace depths have been limited for comparison to the geophone gathers. White arrow indicates BBRS interval, with the coherent low amplitude CO_2 residual evident in the geophone difference (i). The black arrow indicates shallower reflections sensitive to the de-noising method used for DAS data.

Of particular concern were the residual amplitude variations manifesting as vertical banding in panels a & b. These groups of traces originally contained checkerboard noise

which was relatively unaffected by the 3m median filter. The wavefield separation step's f-k filter and deconvolution's scaling effect did further reduce the noise level and partially balance amplitudes, but the imprint of the original noise can still be seen in groups of traces. These bands of variable amplitude cause differences between baseline and monitor surveys and produce relatively incoherent, high amplitude time-lapse residuals in a direct subtraction (panel c).

Some destructive interference of the noise footprint does occur in the full stacked section. However, wide enough bands of traces causing high amplitude residuals, as seen in Figure 6.9c, do not stack out sufficiently. Individual shot gathers can leave a visible footprint in a time-lapse difference, despite the stacking process. If one shot gather has significantly stronger residuals than its neighbours, it tends to dominate the difference between stacked data. Reducing the noise in the raw DAS data was therefore a critical step.

Less vertical striping is visible after aggressive de-noising in Figure 6.9d-f compared to panels a-c. The checkerboard noise of the type shown in Figures 6.4a and 6.7a exists across multiple traces, on varying spatial and temporal frequencies. The black arrow in Figure 6.9 indicates the end of a band of traces whose amplitudes appear too low relative to the rest of the shot gather. These amplitudes appear brighter after aggressive de-noising (panel d), similar to both the monitor gather (e) and the geophone gather (g). For this shot gather, the aggressive de-noising method appeared to have prevented the worst of the DAS noise from surviving the processing flow. Although some of the high-amplitude incoherent residuals have been avoided, the difference from the aggressive de-noising also shows high frequency, coherent, horizontal residuals from subtraction (panel f). This indicates that other sources of noise still exist, either from remaining SNR differences in the DAS data, or errors in depth registration. At this stage in the processing even originally random noise can produce semi-coherent residuals, due to wavefield separation and f-k filtering.

The aggressively de-noised DAS data in Figure 6.9d & e visually matched the geophone reference gathers better than the conservatively de-noised versions. For this reason, the aggressive de-noising method was employed for the DAS time-lapse differences. Figure 6.10 however shows a wider selection of shots which still show high amplitude incoherent residuals that survived the aggressive de-noising and VSP processing.

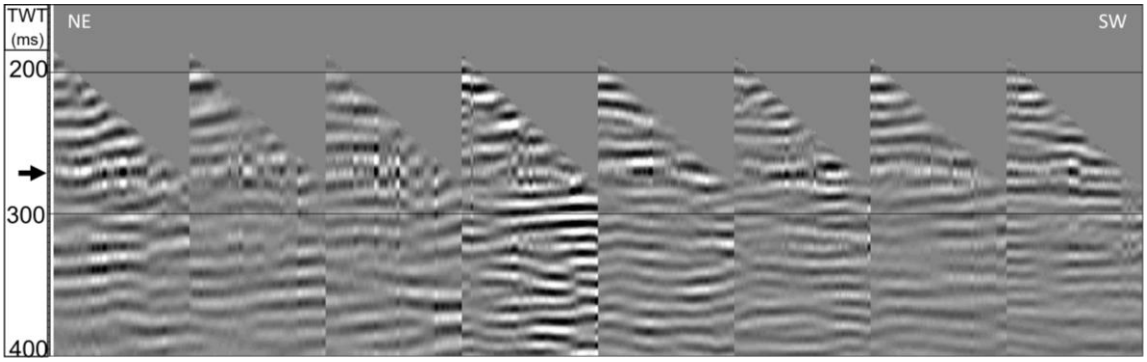

Figure 6.10 Difference between 8 baseline and monitor DAS shot gather pairs from Line 13. Arrow indicates BBRS. Despite aggressive de-noising of the raw data, vertical stripes of high-amplitude residuals remain in the difference. Coherent high frequency residuals are also evident, due to differences within the processed gathers' frequency spectra.

Although aggressive de-noising was ultimately applied for time-lapse purposes, the more conservative de-noising (median filter only) was sufficient for producing apparently high-quality VSP CDP stacks for individual datasets. Much of the coherent noise is removed simply by the standard f-k filter applied during wavefield separation. For a given survey, the dense spatial sampling and extensive vertical coverage of DAS VSP data produces very high stacking power which suppresses much of the noise. In the upcoming sections, Figures 6.11 and 6.12 will show VSP CDP stacks that were made using the conservative de-noising approach and still achieved a high degree of similarity. In later sections showing time-lapse results, the aggressive de-noising was applied instead.

6.1.7 Depth registration

Depth registration was accomplished by assigning a depth to the bottom-most direct arrival (the midpoint in the V-shapes in Figure 6.4). Initially, the assigned depth was 330.22 m MD, the bottom of the fiber array from the well schematics for Obs 2. The bottom-depth of 330.22 m MD was a placeholder value, assumed to be incorrect as additional length of fiber exists at the bottom to accommodate the point where the fiber turns to go back up the well. Depth registration was corrected iteratively by comparing the pre-stack and post-stack DAS data to a MEMS accelerometer survey performed in September, 2018. Similar to DAS, the accelerometer survey covered 0 m to 325 m in Observation well 2. This MEMS dataset is valuable for a variety of applications beyond the scope of this study, providing a high SNR ground-truth for comparison with DAS data. The MEMS data was integrated with respect to time to be comparable to geophone data and the integrated DAS datasets.

Figure 6.11 shows an example of mismatch between otherwise highly similar MEMS and DAS VSP CDP stacks. By comparing against the MEMS data, a value of 342 m MD was determined for the bottom trace. The 342 m value is not a true depth, but simply a best-fit starting point from which to assign depths to the remaining traces. Any error in the bottom depth value was expected to affect both baseline and monitor surveys equally, and therefore not contribute to time-lapse errors. Due to uncertainty about the true depth of the traces near the bottom, DAS traces registered deeper than 325 m were later excluded.

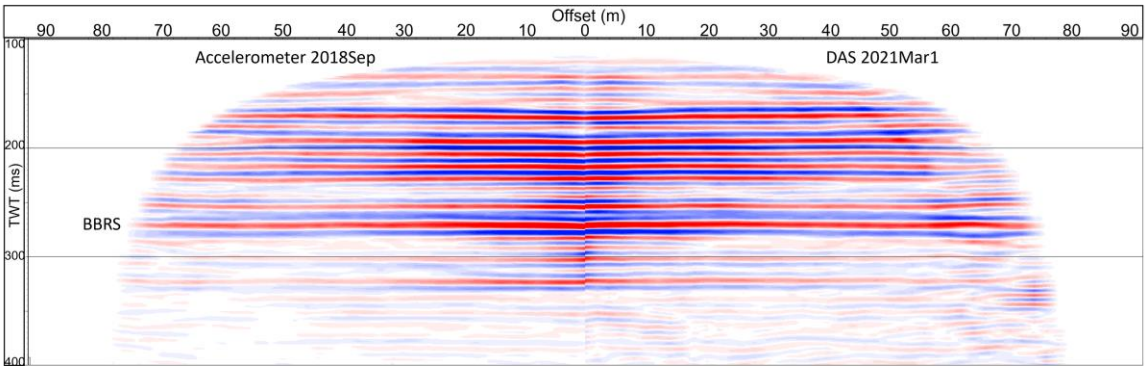

Figure 6.11 Accelerometer (left) and DAS (right) VSP CDP stacks. The DAS reflection times are too early due to incorrect depth registration, causing a discontinuity between the two stacks in the center of the display. This was corrected iteratively by trial-and-error. These examples are from Line 7 with the 2017 data in reverse CDP order for comparison.

Trace depths were assigned in the following manner: Starting from 342 m MD, each progressively shallower trace was assigned a depth incrementally, according to the trace spacing of the interrogator. The trace spacing of a given interrogator depends on the index of refraction of the fiber (Mateeva and Zwartjes, 2017). For convenience, an index of refraction of 1.5 was assumed for the DAS fiber. For example, the OptaSense interrogator used for the 2021Mar1 survey listed a trace spacing of $\Delta z = 1.021$ m for an index of refraction $n = 1.468$, equivalent to a trace spacing of $\Delta z = 0.9992$ m for $n = 1.5$. This was rounded up to $\Delta z = 1$m. A 1m trace spacing was more convenient under the $n = 1.5$ assumption. Similarly, a 0.25 m trace spacing was used for the Silixa iDAS interrogator used in the 2017 baseline surveys. Comparison of processed and stacked baseline and monitor data showed that the trace spacing assumptions required slight corrections. Initially, high frequency time-lapse residuals were generated in the time lapse difference between 2021Mar1 monitor (OptaSense) and 2017Oct and 2017May baseline (Silixa) VSP CDP stacks. Inspection of the stacks showed a slight mismatch between the stacked data

at shallower arrival times due to shallower traces being farther from the bottom depth assignment (Figure 6.12). The monitor survey trace spacing was then increased to 1.003 m after several rounds of trial-and-error testing between $\Delta z = 1.000$ m and $\Delta z = 1.010$ m. This demonstrated the need for trace spacing accuracy within 0.5% or better between two different interrogator units.

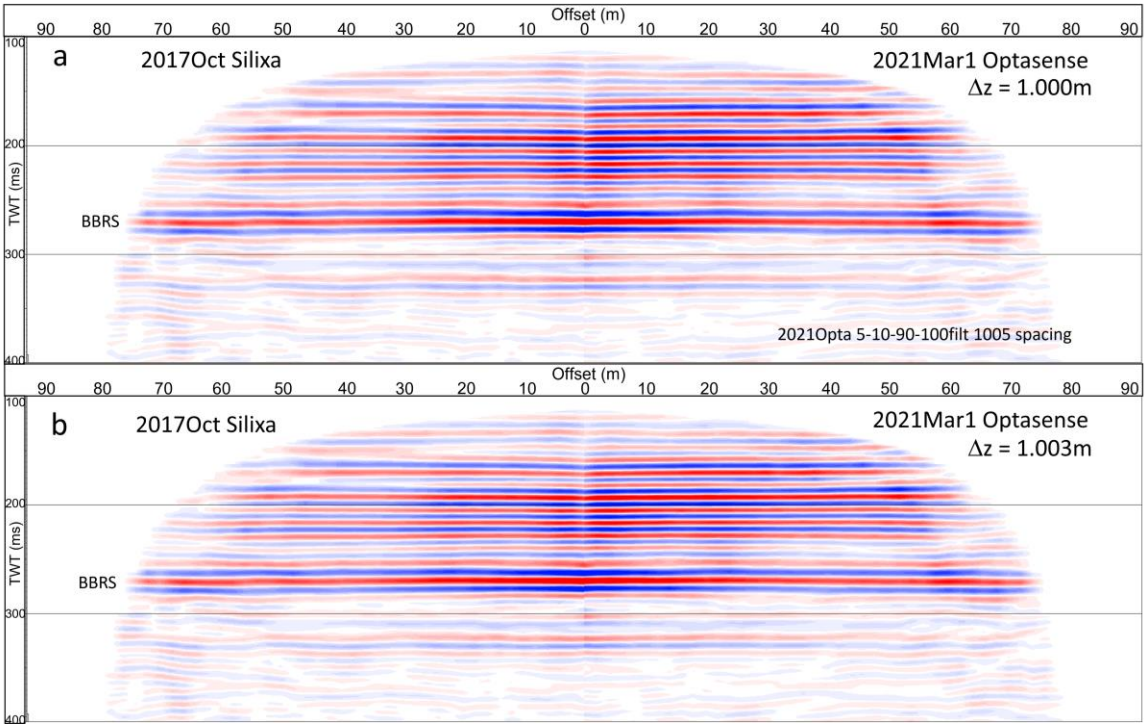

Figure 6.12 Comparison of VSP CDP stacks of (left) 2017Oct baseline and (right) 2021Mar1 DAS datasets to verify depth registration. Panel a shows progressively mismatched reflections in the center at shallower, earlier arrival times. Panel b shows more consistent depth registration between datasets. These examples are from Line 7 with the 2017 data in reverse CDP order for comparison.

The depth registration method described above was chosen for its simplicity and consistency, including consistency of any systematic error. A more analytical approach was attempted involving correlating DAS traces with 2018 MEMS traces of known depths, similar to the process described by Gordon (2019). However, this was found to be too error-prone for time-lapse purposes. The derived trace spacings from comparison with accelerometer and geophone receiver depths exhibited variability on the order of to 5%. Calibration of the depth registration had required error within 0.5%, or better yet 0.1%, in order to avoid introducing high-frequency, coherent time-lapse residuals. Work is ongoing to establish a more consistent analytical solution to depth registration along the 5 km fiber loop for repeated surveys at CaMI.FRS, particularly for the helically wound cables (Hall

et al., 2021). The trial-and-error approach to depth registration described here was expected to be adequate for this time-lapse exercise.

6.1.8 First breaks and source statics

Due to the noise present in DAS data, a loose f-k filter was temporarily applied prior to picking first breaks. The f-k filter offered a simple one-step process for addressing noisy first breaks without altering the trace-by-trace traveltime differences caused by interval velocities in the subsurface. This resulted in much more stable first break picks (Figure 6.13) and higher similarity between baseline and monitor data. Since the DAS data exhibited lower SNR than the geophone data, an Ormsby filter of 5-10-90-100 (Hz) was also applied to remove high frequency noise and ensure similar downgoing waveforms were picked on each dataset. After picking on the f-k filtered data, the stable first break picks were copied back to the original noisier data, and normal processing resumed from there. Although this step was less important if aggressive de-noising had been applied, it was nonetheless performed.

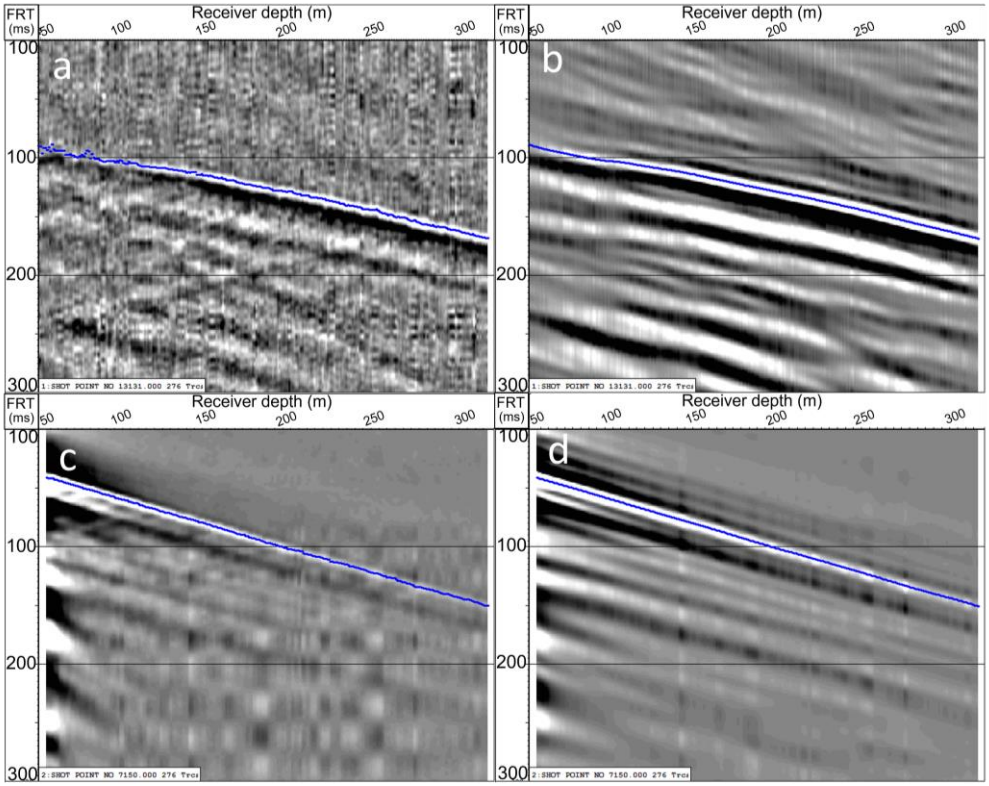

Figure 6.13 Example of a particularly noisy shot gather from Line 13 2017May (a). The first break picks are more stable after f-k filtering (b). A less noisy shot gather from Line 7 2021Mar1 (c) exhibits a lesser degree of first-break pick instability but is still improved by an f-k filter (d) which removes much of the checkerboard noise.

Horizontal raypaths, low SNR traces, and turning waves complicated the first break picking at shallower depths. To avoid error between baseline and monitor data, DAS data were trimmed to 190 m-305 m depth for the calculation of source statics. The 190 m-305 m depth range was chosen to be consistent with the geophone data, but any reasonably deep depth range would have worked similarly well. After determining source static corrections on the temporarily trimmed data, the corrections were applied to the original data which had been permanently trimmed to 50m-325m depth. To summarize, at this stage the data had undergone de-noising with either a a combination of f-k, median, and rms amplitude normalization. The trace depths had been assigned, first breaks had been picked and source static corrections applied, and shot gathers had been trimmed to 50m-325m depths. The time-lapse compliant workflow described in Chapter 4.2 was then applied, starting with wavefield separation and ending with the high-cut filter method of cross-equalization.

6.2 DAS time-lapse VSP results

6.2.1 DAS Line 13 SW-NE time-lapse

The 2021Mar1-2017May time-lapse was performed for the DAS straight fiber data with the equivalent geophone result available for comparison, seen previously in Figure 5.12b. As demonstrated with geophone data in Figure 4.9, the unresolved effects of seasonally variable near-surface filtering were also evident in the equivalent processed DAS gathers. Figure 6.14 shows the frequency spectra of DAS shots 13145, 13155, and 13163. The spectra were extracted from the geophone-equivalent depths of 190m-305m for comparison. The DAS spectra exhibited a noisier character than the geophone equivalents from Figure 4.9. As expected, the near-surface filtering effects appear equivalent between the two types of data. As with the geophone data, shots 13145 and 13163 show nearly the same bandwidth and amplitudes. The baseline shot 13155 exhibits a more strongly attenuated character compared to the monitor spectrum, which was also seen in the geophone data (Figure 4.9). The same set of high-cut filters applied to the geophone data in Chapter 5.4 was therefore used on the equivalent DAS pre-stack gathers. These high-cut filters did not address the noise and amplitude discrepancies within the remaining frequency bands. For example, in Figure 6.14 shot 13163, the high amplitude spike around 80Hz remained. This caused high frequency residuals in the time-lapse difference.

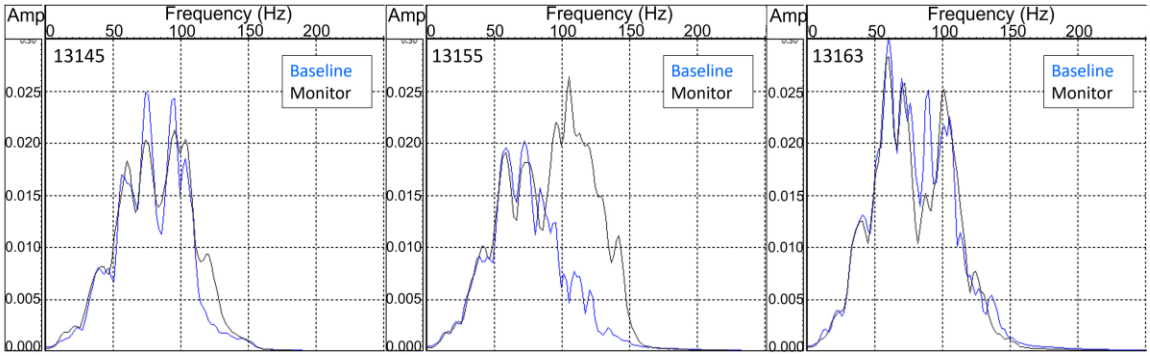

Figure 6.14 Shot gather spectra from 190m-305m DAS traces, equivalent to the geophone spectra in Figures 4.9 and 5.1. Though noisier than the geophone counterparts, these DAS spectra show the same unresolved near-surface filtering differences. Major attenuation differences are apparent for shot 13155.

Figure 6.15 shows the time-lapse difference of Line 13's VSP CDP stacked results from the 2021Mar1-2017May surveys. Trace depths were trimmed to 90m-325m to avoid the worst of the very low SNR data in the shallower traces. Between the high noise levels in the raw 2017May Line 13 dataset and the cumulative attenuation experienced by reflected waves, the receivers above 90m were more trouble than they were worth. Corridor and surgical mutes were tested, but simply trimming the trace depths was most effective at preventing residuals from the shallow traces. As mentioned in Chapter 5.5.1, high degrees of near-surface filtering affected the signal strength of the SW shots beyond 150 m offset in the 2017May survey. The low SNR motivated their removal. While these shots were left

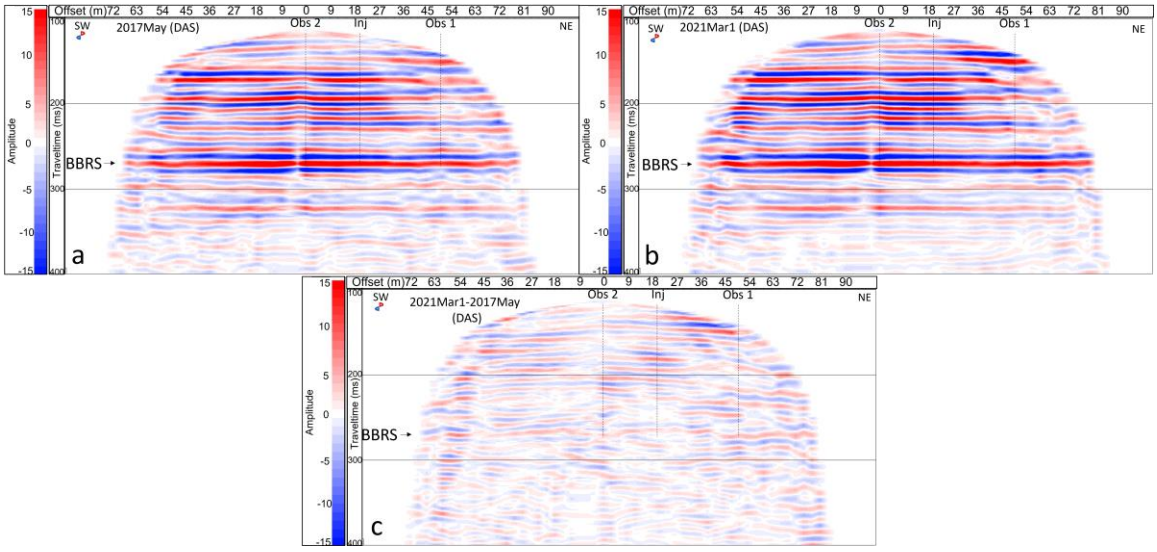

Figure 6.15 Line 13 DAS time-lapse VSP results. The baseline (a) and monitor (b) are similar overall but amplitude variations and reflection character differences can be seen. The difference (c) contains incoherent and coherent residuals and the CO_2 anomaly is not evident.

in for the geophone time-lapse analysis, those particular DAS shot gathers could not supply sufficient signal strength and similarity to warrant their inclusion. Removing them eliminated overwhelmingly high amplitude, low frequency residuals in the stack.

Overall the VSP CDP stacks look very similar. Amplitude differences can be seen however, mainly at farther offsets. The time-lapse difference has strong background time-lapse residuals and does not show the CO_2 anomaly observed in the geophone results from Figure 5.12. The background time-lapse residuals are relatively incoherent around the BBRS interval and below. This indicates that the principal source of error is more likely the noise-related residuals that survived de-noising (as seen in Figure 6.9), which fail to stack out sufficiently to allow the CO_2 anomaly to manifest. At shallower times, the residuals become stronger and more coherent. This indicates depth registration errors may still be occurring as the mismatch between datasets increases at shallower depths. These residuals are likely compounded by low SNR for farther offset reflections, which cause higher amplitude residuals at the extremities of the displays.

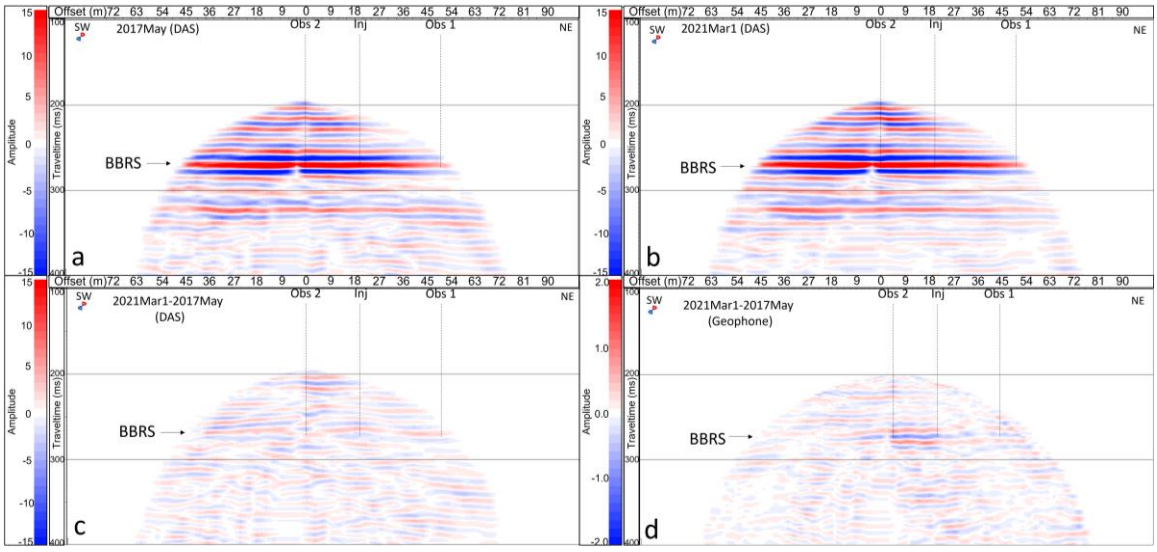

Figure 6.16 DAS time-lapse results from a 190m-305m depth range comparable to the geophone data. The VSP CDP stacked sections appear highly similar (a & b) but the CO_2 anomaly did not manifest in the stack amidst the background noise in panel c. Geophone result in panel d.

The VSP CDP stack and time lapse difference were performed for a 190m-305m selection of the DAS traces, for comparison with the geophone result. Figure 6.16 again shows no CO_2 anomaly standing out from the background time-lapse residuals. Comparing

Figure 6.16c & d, a peak exists in the DAS result where the trough-peak succession of the CO_2 anomaly should be.

6.2.2 DAS Line 7 North time-lapse

The Line 7 DAS baseline survey was from 2017Oct, as opposed to 2017Jul for the geophones. New high-cut filters were designed to accommodate the 2017Oct baseline DAS data, but otherwise the geophone and DAS results were treated as directly comparable. Figure 6.17 shows the Line 7 time-lapse. Unlike with Line 13, a shallower 70m-325m depth range seemed feasible due to the higher data quality of the 2017Oct Silixa interrogator baseline. As seen in other displays, the VSP CDP stacks look very similar with even the less coherent portions matching well between baseline and monitor. Despite the shallow far-offset residuals in Figure 6.17c, this time-lapse result showed promise. The BBRS interval showed a weak trough between offsets 0 m and 36 m CDP offset, amid relatively low amplitude background time-lapse residuals.

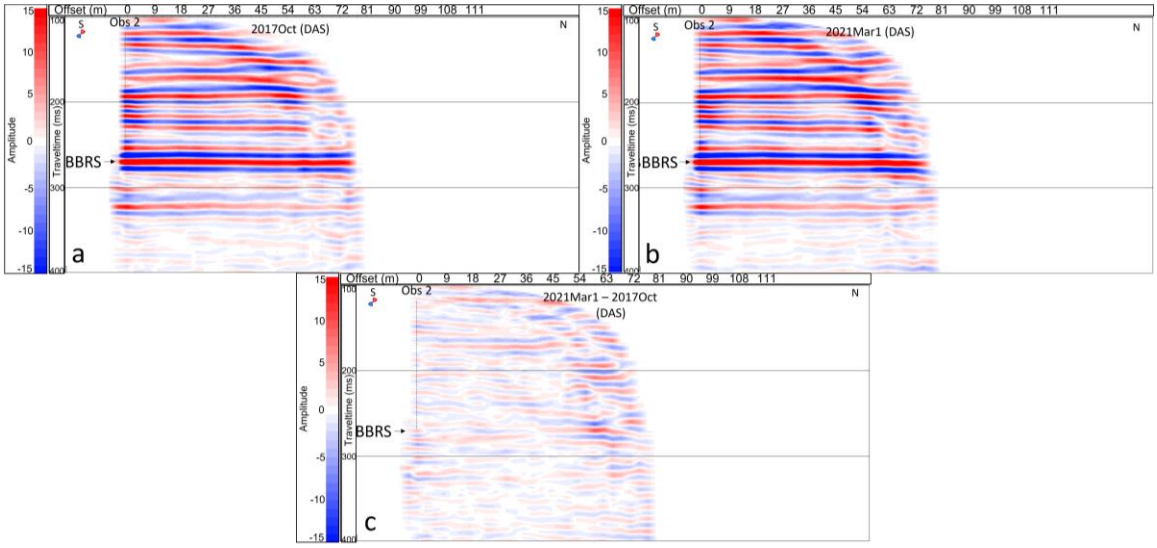

Figure 6.17 Line 7 DAS time-lapse results showing baseline (a), monitor (b), and difference (c) sections. A weak trough exists at the BBRS interval amid relatively low background residuals.

The 190m-305m depth version of the stack is shown in Figure 6.18. Note that the horizontal axes are scaled the same, but the DAS time-lapse only had shot offsets to 160 m. Therefore, fewer far offset reflections were recorded than with the geophone survey from 2017Jul, and the reduced horizontal coverage of the DAS time-lapse can be seen.

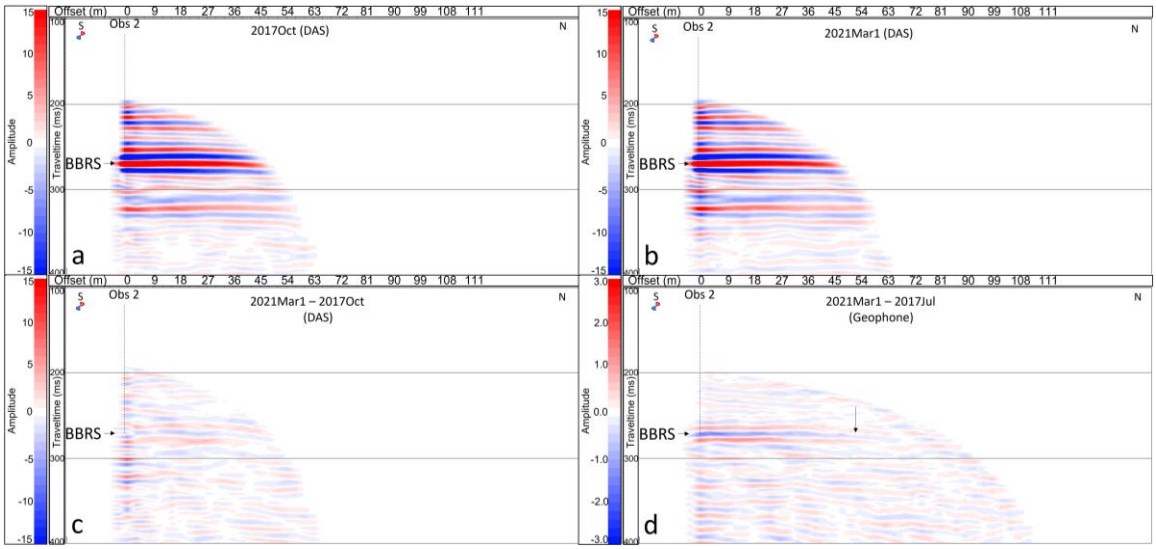

Figure 6.18 Line 7 DAS 190m-305m time-lapse with baseline (a), monitor (b), difference (c), and geophone time-lapse difference for comparison (d). A fainter, noisier, and lower frequency version of geophone's time-lapse anomaly appears to exist in the DAS time-lapse result in panel c.

After removing the noisier shallow data, the Line 7 DAS time-lapse shows a weak trough-peak anomaly at the BBRS interval in Figure 6.18c. This residual is lower amplitude, noisier, and lower frequency in appearance than the geophone time-lapse anomaly. While the result is ambiguous, it may indeed be the CO_2 anomaly barely showing through the time-lapse difference. Although the DAS data has fewer shot gathers stacking in than the geophone data in Figure 6.18 and thus lower fold at near offset, it is more likely that higher noise levels remain the principal factor preventing a strong CO_2 anomaly from showing through. The Line 7 DAS time-lapse result was the best yet achieved, and gave confidence that a more unequivocal detection of the CO_2 with the DAS data will occur soon. The less noisy 2017Oct baseline provided a VSP CDP stack with fewer obvious amplitude differences between baseline and monitor than were observed for Line 13. While the Line 13 2017May baseline seemed irrevocably contaminated with noise, the 2017Oct Line 7 baseline should be adequate to remain as a baseline for future time-lapse work.

6.2.3 DAS and geophone NRMS

Table 7 lists the NRMS values from the DAS time-lapse results and the equivalent geophone results. As expected, the larger DAS stacked sections yielded higher NRMS values due to the inclusion of more background time-lapse residuals at far offsets and shallower intervals. When comparing 190 m-305 m geophone equivalent stacks, the Line 13 DAS data maintain higher values (17%-28%) than their geophone counterpart (15%-

20%). This is despite the geophone NRMS value being inflated by the strong CO_2 anomaly. As was seen visually in Figure 6.16, the NRMS value is caused by strong background time-lapse residuals in the DAS Line 13 results, obscuring the effects of the CO_2.

Table 7. DAS and geophone NRMS

Data type	VSP line	Time-lapse	CO_2 effect	Window	NRMS
DAS 90m-325m	13	2021Mar1-2017May	Undetected	150ms-400ms	34%
				250ms-290ms	23%
DAS 190m-305m	13	2021Mar1-2017May	Undetected	150ms-400ms	28%
				250ms-290ms	17%
Geo 190m-305m	13	2021Mar1-2017May	Strong	150ms-400ms	20%
				250ms-290ms	15%
DAS 70m-325m	7	2021Mar1-2017Oct	Weak to none	150ms-400ms	30%
				250ms-290ms	21%
DAS 190m-305m	7	2021Mar1-2017Oct	Weak to none	150ms-400ms	22%
				250ms-290ms	14%
Geo 190m-305m	7	2021Mar1-2017Jul	Strong	150ms-400ms	25%
				250ms-290ms	18%

The Line 7 DAS data had lower NRMS values than Line 13 DAS data, which is consistent with the observed difference in noise levels and background time-lapse residuals. The 190 m-305 m version of the DAS results had a lower NRMS (14%-22%) than the Line 7 geophone (18%-25%). The background time-lapse residuals appeared comparable in Figure 6.18, so the difference in NRMS must be being caused by the strong CO_2 anomaly in the geophone data. This gives further indication that the Line 7 datasets are of adequate quality for shallow monitoring, but are not capable of achieving the same low detection threshold as the geophone data. Further monitoring data from late 2021 and from 2022 will be needed to confirm that assessment.

CHAPTER 7 - MAXIMIZING USABLE BANDWIDTH

7.1 Review of frequency limitations

The shot-dependent high-cut filtering method of cross-equalization, described in Chapter 5.4, was successful at reducing background time-lapse residuals while preserving the amplitude differences caused by the CO_2 plume. However, some of the higher frequency reflection data were lost in the process (Figure 5.8). Preserving more of the high frequency content in the time-lapse VSP data allows for better resolution of the CO_2 plume. To do so, a more finely tuned deconvolution operator was required. This allowed for independently balanced amplitude spectra up to a greater frequency cut-off than was achieved in Chapters 4 & 5. The upper frequency bands suffered higher attenuation and are lower SNR than the lower frequency bands preserved in the successful time-lapse results of Chapter 5. The following two sections describe the process of building trust in the data integrity of the restored higher frequency bands. A conceptual convolutional model was developed with the goal of validating the logic underpinning the scaling and normalization effect of the deconvolution operator, which was invoked in Chapter 4. A higher frequency time-lapse result for Line 13 geophone data is then presented. This is followed by examples of preserving higher frequency bandwidth by bypassing the static and variable near-surface filtering effects altogether, using a permanently installed helical pile and an impulsive source.

7.2 Convolutional model

A conceptual convolutional model describing how deterministic deconvolution addresses most scaling and attenuation needs begins with the Equation 2. The downgoing direct arrivals s_D,

$$s_D = w * f_{sv} * f_{ns} * f_{ssd}, \tag{2}$$

are produced by convolution of the wavelet w with the f terms representing various filtering effects: seasonally variable near surface-filtering (f_{sv}), static or unchanging near-surface filtering (f_{ns}) in the unconsolidated weathering layer, and static subsurface downgoing-wave filtering (f_{ssd}) below the weathering layer. Following from Equation 2, the upgoing reflected wavefield is represented by the convolution of the downgoing arrivals with the earth's reflectivity followed by additional attenuation,

$$s_U = w * f_{sv} * f_{ns} * f_{ssd} * f_{ssu} * r = s_D * f_{ssu} * r, \quad (3)$$

where s_U is the upgoing wave, and r is the earth's reflectivity. The term f_{ssu} represents the additional subsurface upgoing-wave filtering along the raypath between the reflection point and the receiver. After wavefield separation, deconvolving the upgoing data attempts to remove the effects of the filtering terms that make up the downgoing direct arrival term, s_D. The deconvolution operator d is the inverse of the downgoing direct arrival,

$$d = s_D^{-1} = (w * f_{sv} * f_{ns} * f_{ssd})^{-1}. \quad (4)$$

To proceed, some assumptions need to be made. The filtering terms f_{ns} and f_{ssd} represent unchanging subsurface effects that should be equal for both baseline and monitor data. Assuming that the subsurface attenuation is not severe enough in these shallow data to effectively zero any of the frequency bands, those two terms can be considered reversible effects. Some shot gathers maintain bandwidth up to 150Hz, supporting this assumption. For farther offset shots (e.g. beyond 100m) this assumption does break down. The wavelet term w could also be considered consistent between surveys, except that its band-limiting effects persist in the data. Assuming an identical source wavelet would require that the seasonally variable filtering term f_{sv} accounts for both the immediate impact of surface conditions on source signature, as well as subsequent variable near-surface filtering.

Proceeding under these assumptions, the deconvolved upgoing wavefield s_U^d would be obtained by applying the deconvolution operator d with most of the consistent filtering effects from Equation 4 treated as commutative, invertible filters. This allows them to cancel out with their inverse partner terms as

$$s_U^d = d * s_u = f_{sv}^{-1} * f_{sv} * w^{-1} * w * f_{ns}^{-1} * f_{ns} * f_{ssd}^{-1} * f_{ssd} * f_{ssu} * r,$$
$$s_U^d = {f_{sv}}^{-1} * f_{sv} * f_{ssu} * r = f_{sv}^R * f_{ssu} * r, \quad (5)$$

where

$$f_{sv}^R = {f_{sv}}^{-1} * f_{sv}.$$

The seasonally variable near-surface filtering term f_{sv} can not simply cancel out with its inverse. For some shots, the near surface filtering effect can be so drastic that it effectively band-limits the higher frequencies while severely attenuating the lower frequencies. These remaining filtering effects are grouped together in the f_{sv}^R term in Equation 5. This is in

addition to the band-limiting effect of the source wavelet, which was 10Hz-150Hz in the case of these CaMI.FRS data. This f_{sv}^{R} term would depend on shot location and be different for each baseline and monitor shot gather. It represents the primary source of dissimilarity between baseline and monitor data. The minor, yet unresolved, upgoing filter term f_{ssu} also remains in Equation 5. For a repeated raypath, the f_{ssu} term would be equal between baseline and monitor data. Keeping in mind the numerous assumptions and simplifications, Equation 5 indicates that in this scenario the deterministic deconvolution amounts to removing the effects of the wavelet and static near-surface and subsurface filtering, while only partially removing the seasonal near-surface filtering for any given shot gather. This process produces baseline and monitor gathers with reflection data of equivalent amplitude spectra, up to a point of divergence where the near-surface effects are imperfectly removed in upper frequency bands. This was seen earlier in Chapter 4, Figure 4.9.

7.3 Convolutional matrix model

The convolutional model described in the previous section offered a simplified conceptual description of the partial removal of the seasonal near-surface filtering effects. In addition to the numerous assumptions made, that description ignored the order in which the various filtering effects are resolved analytically. In matrix form, the downgoing and upgoing wavefield are described as

$$\boldsymbol{s}_U = F_{ssu}F_{ssd}F_{ns}F_{sv}W\boldsymbol{r} = F_{ssu}S_D\boldsymbol{r}, \tag{6}$$

in which the S_D, W, and the various F terms and are convolutional matrix equivalents to their lower-case counterparts in Equations 2 - 5. Equation 7 shows the corresponding inverse of the downgoing wavefield term,

$$S_D^{-1} = [S_D^T S_D + \lambda]^{-1} S_D^T, \tag{7}$$

where λ is a pre-whitening term for the matrix inversion, and the *T* superscript represents a transpose matrix. Therefore, rather than Equation 5, the deconvolved upgoing wavefield time-series $\boldsymbol{s}_U^D$ should be expressed as

$$\boldsymbol{s}_U^d = S_D^{-1}\boldsymbol{s}_U = [S_D^T S_D + \lambda]^{-1} S_D^T F_{ssu} S_D \boldsymbol{r}. \tag{8}$$

Equation 8 indicates the imperfect removal of the downgoing wavefield S_D due to both the pre-whitening term λ and the upgoing attenuation term F_{ssu} in between the

deconvolution operator and the downgoing wavefield term. This F_{ssu} term could be addressed by independently developing an attenuation model of the subsurface and applying a subsequent time-variant inverse Q filter (Hargreaves and Calvert, 1991; Wang, 2002). This would more correctly remove the F_{ssu} term after wavefield separation, but prior to deconvolution. A time-variant inverse Q filter was generated previously from the 2018 MEMS accelerometer data (Kolkman-Quinn and Lawton, 2020) and could be repeated in the future. However, that inverse Q filter was not applied to the results presented here for the following reasons: It was not expected to have a significant effect due to the application of high-cut filters to match bandwidths (Chapter 5.4), and the impact of the F_{ssu} attenuation term on deconvolution (Equation 8) was expected to be both minor and equal between baseline and monitor datasets. The focus was on establishing a simplified time-lapse compliant workflow to produce interpretable, high confidence results, and the inverse Q filter represented yet another possible source of error.

The conceptual convolutional model described above provided sufficient grounds to continue with the heavy reliance on the deconvolution operator to resolve all amplitude scaling needs between baseline and monitor data, without use of a shaping filter. A less conservative deconvolution design was therefore tested, as described in the next section.

7.4 Deconvolution pre-whitening

During development of the time-lapse VSP workflow, and the subsequent production of the results seen in Chapters 4 & 5, the pre-whitening term λ (Equation 8) had been left at a default value of 1% for the deconvolution step (Chapter 4.2.5). This was a conservative value which produced reliably stable deconvolution results. However, the high SNR of the CaMI.FRS geophone datasets allowed for a much smaller pre-whitening terms to be used. Figure 7.1 shows a comparison of the deconvolved spectrum of shot 13155 using λ = 1% and λ = 0.05% pre-whitening terms for the deconvolution operator design. Shot 13155 had shown very disparate amplitudes above 80Hz, due to significant near-surface filtering during 2017May acquisition (Figure 7.1a). The frequencies below that divergence point matched very well. Significantly reducing the pre-whitening term to 0.05% allowed for more of the high frequency band to be scaled up (Figure 7.1b). The λ = 0.05% version of the deterministic deconvolution appeared to properly scale the highly attenuated 80Hz-120Hz band of shot 13155 to the same level as the monitor data. The much-less attenuated

monitor data's spectrum was itself scaled up considerably to the 150Hz limit of the sweep. Note that a 5-10-140-150 (Hz) bandpass filter was applied after deconvolution, as was standard with all the vibroseis datasets.

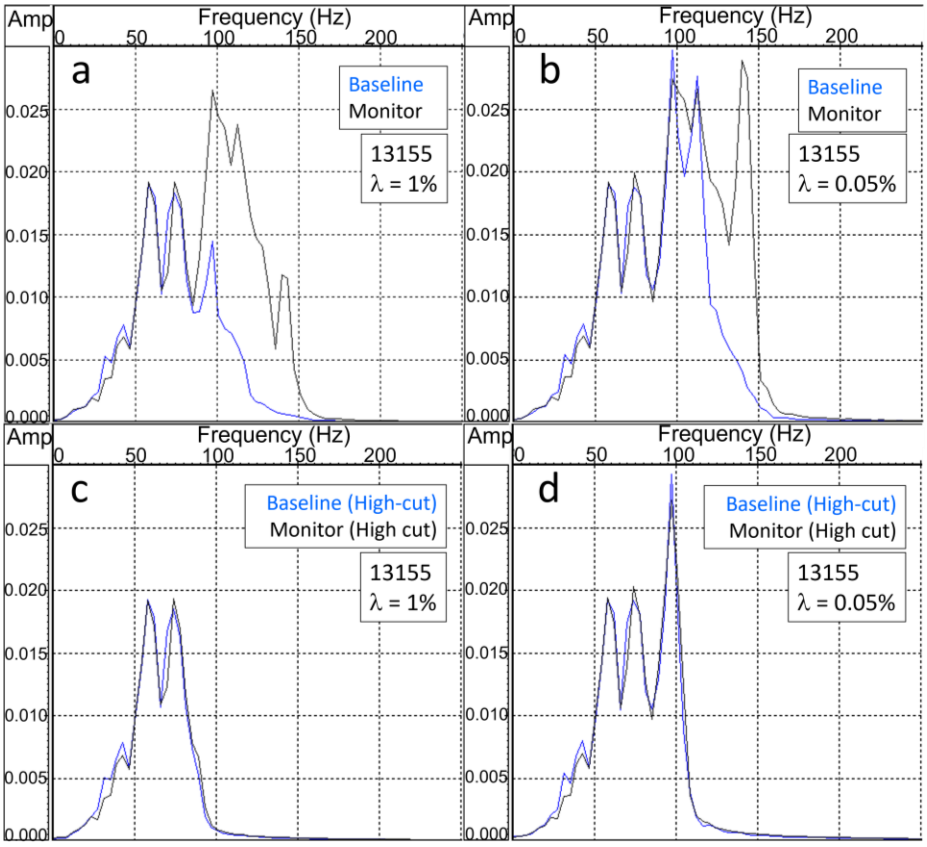

Figure 7.1 Baseline and monitor spectra for shot 13155 using (a) 1% and (b) 0.05% pre-whitening during deconvolution. Comparable additional frequency content was restored (b) with the smaller pre-whitening terms, and a higher frequency cut-off could be used (panel d vs panel c).

Seasonal near-surface filtering effects were still not completely reversed by the less conservative deconvolution, as can be seen by the remaining bandwidth difference for shot 13155. Rather, the available bandwidth was simply increased. A high-cut filter was still required to avoid high frequency residuals. Although the baseline and monitor amplitudes were relatively similar up to 120Hz, the difference seen in in the 100Hz-120Hz band of panel b caused significant time-lapse residuals. These were eliminated by high-cut filtering to 105Hz (panel d). Shot 13155's usable frequency content had increased by 15Hz. This amount of increase was generally possible with the other shots, though not all. More severely attenuated shots rapidly became too noisy in the upper frequencies with this deconvolution design, and only gained 5Hz-10Hz of usable bandwidth. Some moderately-

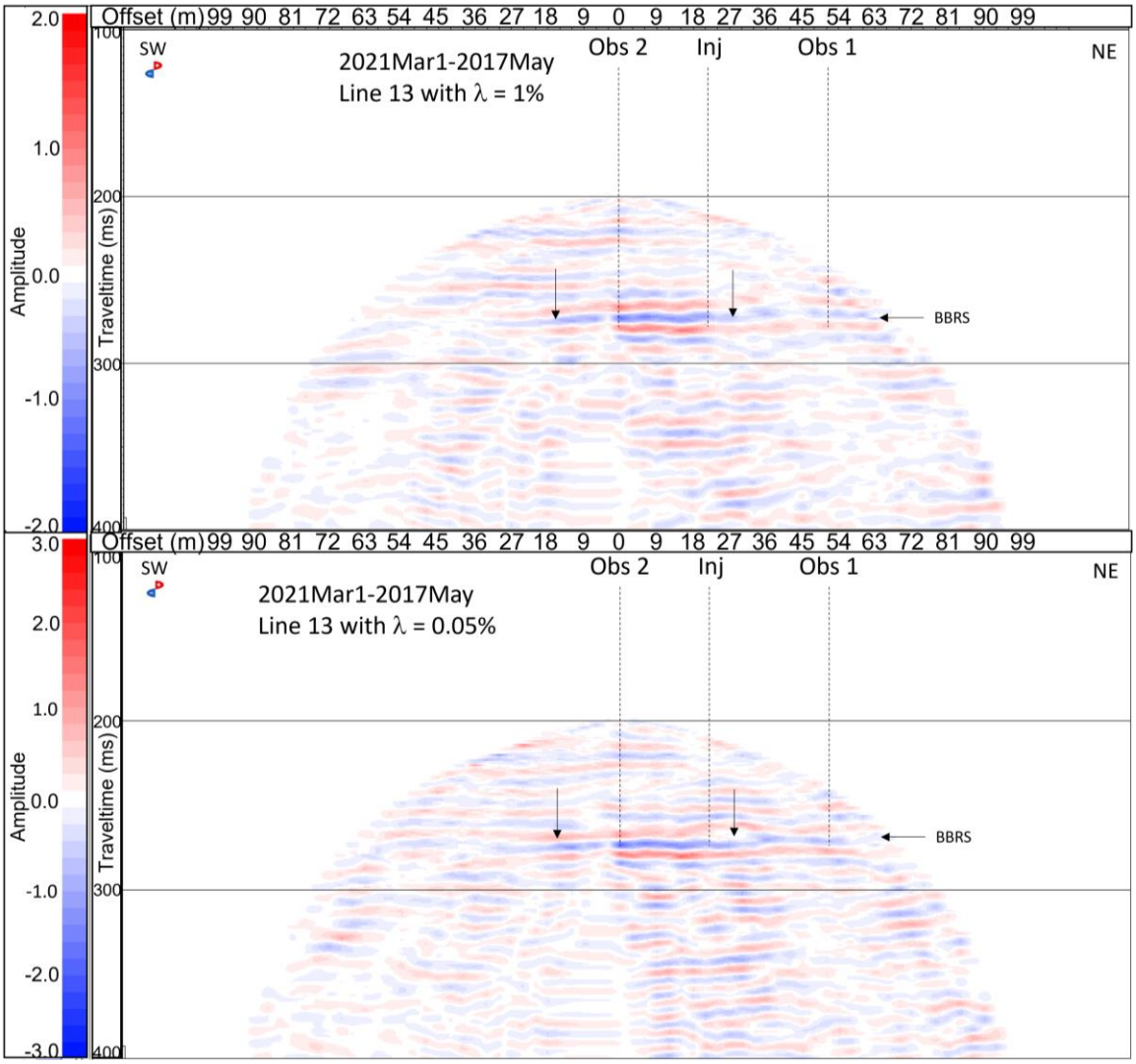

Figure 7.2 VSP time-lapse comparison between original (a) and higher-frequency (b) Line 13 results. The increased frequency content has correspondingly improved resolution with a similar level of background time-lapse residuals. The plume edge interpretation remains the same.

attenuated shot gathers, such as 13145 and 13163 (Figure 4.9), also had modest gains. Those had already been scaled up to near the limit of what was possible during the 1% pre-whitened deconvolution and had little to gain beyond ~120Hz. An updated set of high-cut filters was designed for Line 13 leading to a higher resolution stacked time-lapse result.

Figure 7.2 compares the original and improved BBRS CO_2 anomaly from Line 13, after recovering more high frequency content. Though subtle, the improved resolution from the preserved higher frequency content can be observed. The improved resolution and similar level of background time-lapse residuals in Figure 7.2a & b lends further confidence to the

existing time-lapse workflow. The plume edges are better defined and easier to interpret in the broader-band result in Figure 7.2b.

Further experimentation with deconvolution design parameters, such as of pre-whitening, design window, and operator length, may allow for slightly more frequency content to be preserved. The amplitude scale for panel b was adjusted from +/-2.0 to +/-3.0 to provide a similar display brightness while accommodating the increased amplitudes from the additional frequency content.

7.5 By-passing near-surface filtering

A steel helical pile is installed at CaMI.FRS, 62 m south-west of the Obs 2 well along Line 13. The steel pile extends into the subsurface to 24.7 m depth. In 2020 and 2021, impulsive seismic sources developed by 3P Technology Corp. were tested after being mounted on a steel pedestal on top of the helical pile (Lawton et al., 2020). The helical pile transmits the source wavelet down to its base, where it acts as a point source at 24.7 m depth (Figure 7.3). This allows for the near-surface filtering effects to be bypassed.

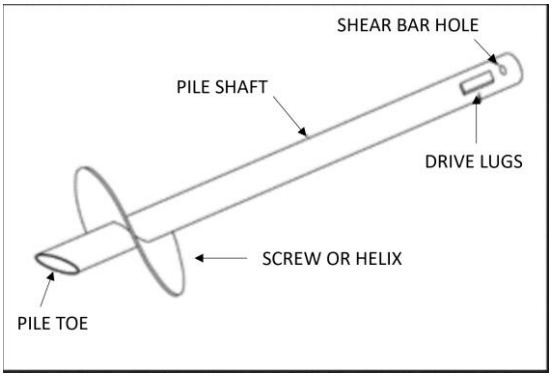

Figure 7.3 Schematic of the helical pile design from Lawton et al. (2020). The pile transmits the seismic source energy down towards the toe, which acts as a point source 24.7 m below the surface.

Borehole geophone data from three phases of testing sources mounted on the helical pile showed broad frequency content in the downgoing arrivals and upgoing reflection data. Shot gathers from this single location were processed using the same processing workflow described in Chapter 4, with a λ = 0.05% pre-whitening term for the deconvolution. As demonstrated with the geophone data in the previous section, this was intended to preserve as much frequency bandwidth as possible. Figure 7.4 shows the deconvolved reflectivity spectra from each of the three phases of testing, compared to a vibe shot on the surface

adjacent to the helical pile. The vibe sweep covered the standard 10 Hz – 150 Hz bandwidth and was therefore more band-limited even before the effects of near-surface filtering.

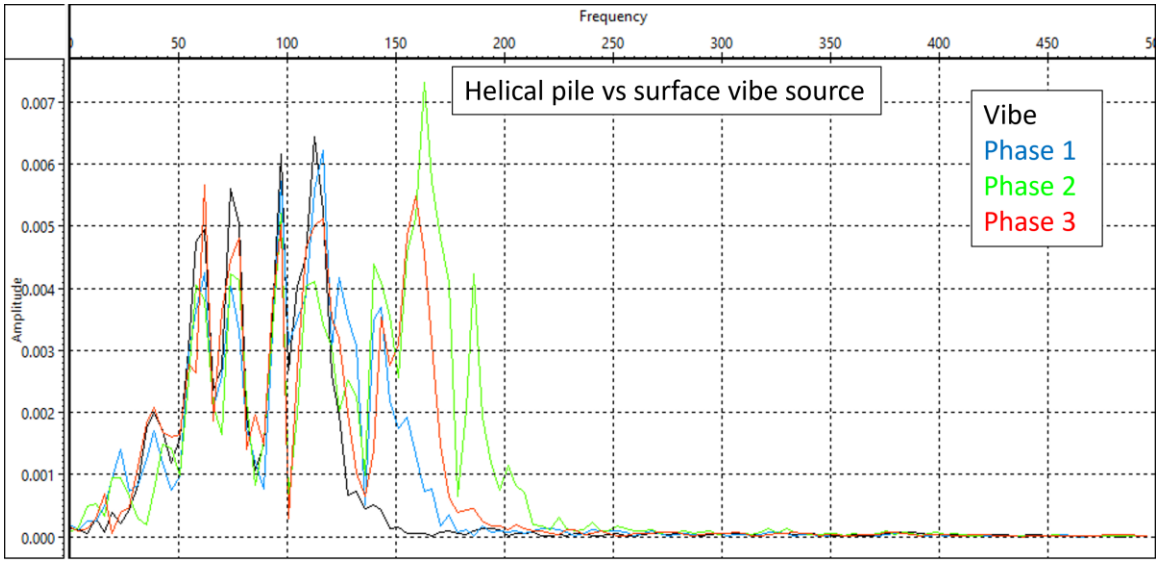

Figure 7.4 Frequency spectra of deconvolved and stacked reflection data collected from an impulsive seismic source on a permanetly installed helical pile at the CaMI.FRS. The three phases refer to three iterations of the seismic source being tested. A reference vibroseis shot (black spectrum) is also shown, from a surface location adjacent to the helical pile.

The four spectra match very closely up to 125Hz, indicating the major peaks and valleys in the spectra are caused by consistent subsurface effects, as opposed to noise. The shapes of the spectra are consistent with those seen in other geophone records of vibe sweeps, such as Figures 4.9 and 7.1. However, different noise levels do cause relative differences in the various spectra from the four sources. Beyond 125Hz, instrument differences in the sources caused differences in bandwidth. The sources mounted on the helical pile were able to transmit recoverable seismic frequencies of up to 200Hz down to the borehole geophones. While the vibe sweep did not extend to this range, the near-surface attenuation likely band-limited the vibe spectrum at 125Hz regardless. This indicates that a higher frequency sweep would likely not have survived the filtering effects of the near-surface at that particular shot location. Although the sources mounted on the helical pile produced individual shots of lower energy than the vibe, repeated shots could be stacked to improve SNR.

Figure 7.5 shows seismic traces from the vibe and 3P Technology Corp's sources generated by stacking the 24-traces of the shot gathers. In this regard, the shots were treated as zero offset, despite being 62m offset from the observation well. The effects of increasing frequency content can be seen, particularly in the Phase 2 and Phase 3 traces and the high

frequency synthetic on the right. Phase 2 was repeated and stacked fewer times and exhibited more noise in the stacked trace, most evident below 300 ms. However, the phase 2 reflections down to the BBRS injection interval appear to represent true physical seismic reflectivity without significant noise contamination.

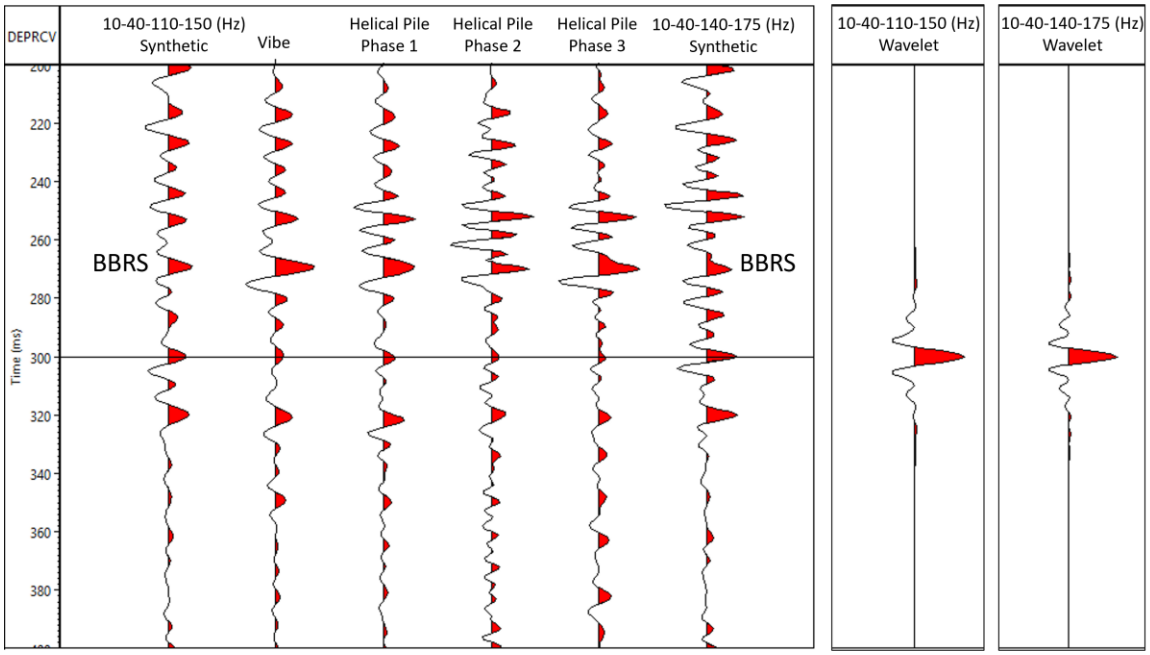

Figure 7.5 Stacked traces from the three helical-pile mounted sources, compared to vibe. A low frequency synthetic seismogram, matching the vibe, and a high frequency synthetic, matching Phase 3, are provided for reference.

With the 150 Hz – 200 Hz frequency band available, the high amplitude peak at the BBRS becomes a doublet, as seen in Phase 2 and in the high-frequency synthetic. The phase 3 trace is just beginning to show the BBRS doublet. Figure 7.6 shows the same traces filtered down to 5-10-140-150 Hz. A very high degree of similarity between each of the field data traces as well as the synthetic seismograms can be seen when the 150 Hz – 200 Hz frequency band has been removed. The similarity between 4 different sources and the synthetic seismograms shows just how effective the VSP data and deterministic deconvolution can be at returning the true (band-limited) reflectivity of the subsurface.

The improved resolution of the BBRS interval and the broad frequency content observed in Figure 7.4 demonstrate the value of bypassing the variable and static filtering effects of the near-surface. A sparse array of helical piles with permanently or periodically installed seismic sources would likely be capable of providing high repeatability, high quality

shallow monitoring data between more densely shot monitoring surveys. Chapter 9 lists suggestions of future analysis that could be performed with the helical pile at CaMI.FRS.

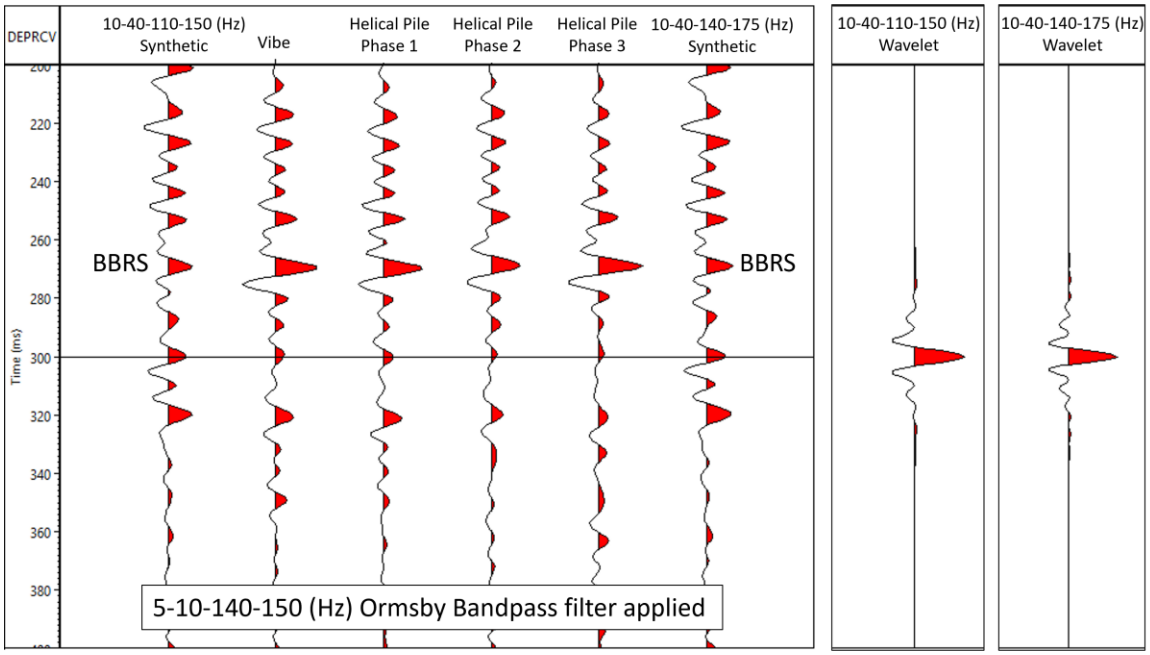

Figure 7.6 The traces from Figure 7.5 filtered down to 5-10-140-150 Hz. The traces match each other and the synthetic seismograms very well, indicating that deterministic deconvolution successfully removed four different source signatures to yield the band-limited reflectivity of the subsurface.

CHAPTER 8 - DISCUSSION

8.1 Geophones: Detection threshold

The time-lapse compliant processing workflow (Chapter 4) and pre-stack high-cut filter method of cross-equalization (Chapter 5) produced time-lapse results showing CO_2 plume amplitude anomalies, without the application of a shaping filter for cross-equalization. In the 2019Aug-2017May time-lapse VSP results for Line 13 (Figure 5.12a), the possible reflection anomaly from the 15 t CO_2 plume was relatively weak compared to the background time-lapse residuals. By March 2021, the increased saturation and lateral extent of the 33t CO_2 plume caused a more pronounced time-lapse anomaly, clearly standing out from the background residual amplitudes (Figure 5.12b & c). Figure 5.14 also showed the pronounced anomaly in the 4-year time-lapse on Line 7. Similar to the 2019Aug-2017May time lapse, a shorter 1.5 year time lapse on Line 15 did not surpass the detection threshold (Figure 5.13). Combined, these results indicate the detection threshold for the plume was reached between 15 t and 33 t of injected CO_2. The ability to confidently identify the CO_2 plume depends on a combination of sufficiently high CO_2 saturation to cause a strong enough amplitude anomaly, and sufficient lateral plume extent on the seismic section to be able to identify a consistent anomaly amid background time-lapse residuals.

The detection threshold can be compared to the SW Hub project in Australia. At 400 m depth, that field research site is the most comparable in depth to CaMI.FRS' 300 m depth of injeciton. An injection amount of 40 t was positively identified in DAS time-lapse VSPs at the SW Hub (Michael et al., 2020). This is similar in scale to the 33 t injection volume detected at CaMI.FRS, but on DAS rather than geophone data. Both projects provide rare field data from shallow CO_2 injection experiments, and each contributes unique information to ongoing research into CO_2 storage and MMV capabilities. In terms of reservoir properties and seismic response, significant differences exist between the SW Hub and CaMI.FRS geological settings. The SW Hub reservoir at 400 m depth has high porosity (28%) and features a prominent fault, whose effect on CO_2 migration was a key research question (Michael et al., 2020). At CaMI.FRS, the BBRS reservoir at 300 m depth has a much lower porosity (10%) and lower amplitude response, with no expectation of significant faults or fractures in the reservoir (Dongas, 2016). The 33 t detection threshold

achieved at CaMI.FRS serves as a new independent result from a different geological setting. The high repeatability monitoring capabilities and cautious processing required to produce these results provides valuable information upon which to base expectations for MMV capabilities for future CO_2 sequestration projects and for enhanced oil recovery operations.

8.2 Geophones: CO_2 plume delineation

Based on the VSP results, the delineation of the CO_2 plume is presented in Figure 8.1. The black outline is based off the interpreted edges of the plume on Lines 7 and 13. Uncertainty remains as to the precise plume edges, due to its diffuse saturation and the decreasing fold with CDP offset.

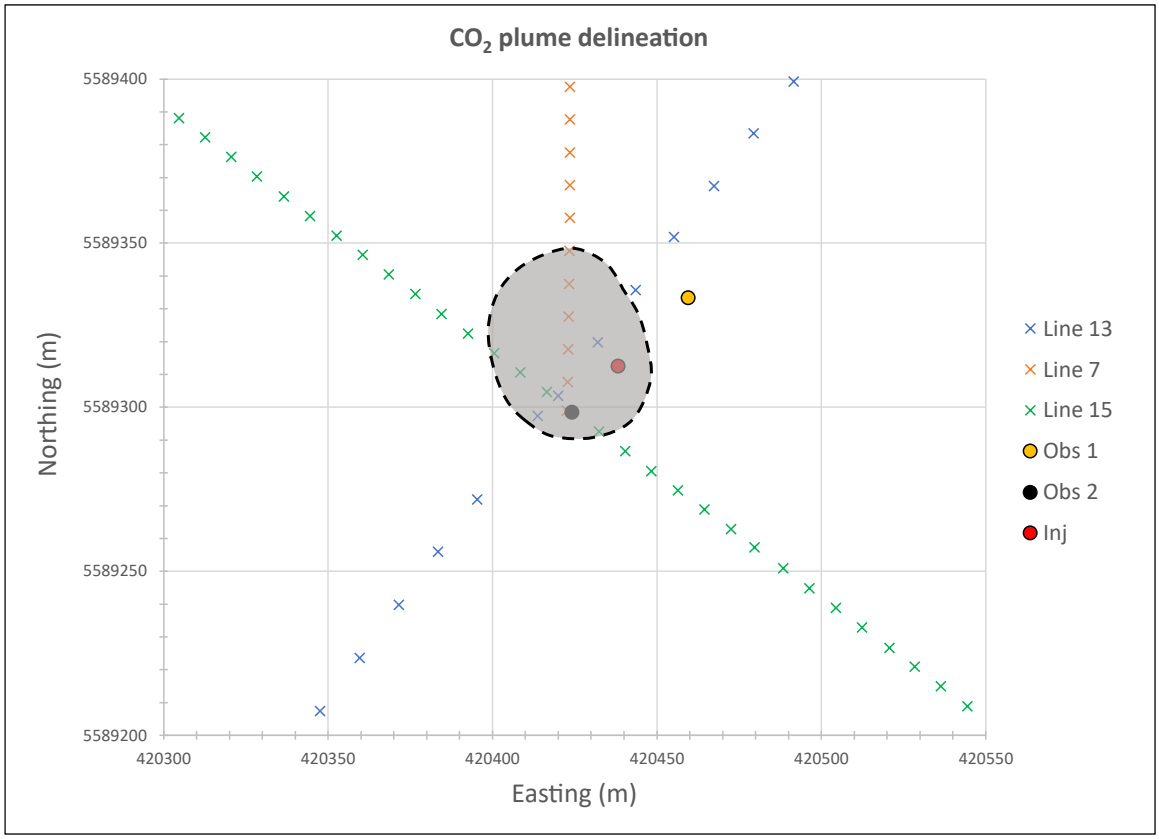

Figure 8.1 Probable extent of the CO_2 plume based off time-lapse results of Lines 7 and 13. The extent to the SW is based on Line 13 alone. This was not confirmed by the inadequate time-lapse period available on Line 15.

The south-west extent of the plume in Figure 8.1 is based solely off the Line 13 time-lapse interpretation which indicated the plume extended beyond Obs 2 and therefore across Line 15. This is neither supported nor disproven by Line 15, whose 1.5 year time-lapse period

was considered too short to achieve detection. Thus, the plume edges at Line 15 were simply extrapolated by assuming a rounded shape. The higher-frequency time-lapse result achieved for Line 13 (Figure 7.2) strengthened the confidence of the plume extent, but did not alter the interpretation. Time-lapse ERT data from CaMI.FRS has also shown the presence of CO_2 in the BBRS extending to Obs 2, and most likely beyond, by 2021 (Macquet et al., 2021). Geochemical sampling at the Obs 1 well had not detected the CO_2 plume in the north-east by March 2021, nor has the CO_2 been detected there by January 2022 at the time of writing. Those independent subsurface monitoring data agree with the time-lapse VSP results presented here. Finally, the approximate 45 m - 51 m lateral extent of the plume on Lines 13 and 7 broadly agrees with the 50 m diameter expectation from reservoir modeling (Figure 3.4), albeit with an asymmetric distribution around the injection well. Further monitoring results from late 2021 and early 2022 are expected to improve the delineation on all three monitoring Lines (7, 13, 15). This will allow for a hypothesis to be made regarding the asymmetric distribution of the plume seen in the time-lapse VSP data. Characterizing the detection threshold in terms of CO_2 saturation will require a seismic inversion to be performed in the future.

8.3 Time-lapse compliant workflow

With the geophone data, consistent time-lapse results were achieved using multiple baseline and monitor datasets across 3 monitoring lines. This indicates high-confidence can be placed in the time-lapse compliant processing workflow described in Chapters 4 and 5. Of the numerous steps taken to reduce sources of processing error, the most impactful were ensuring consistent first break picks, removing 3-C data rotation and associated dead trace interpolation errors, and removing trace amplitude normalization based on direct arrival amplitudes. Relying heavily on deterministic deconvolution to properly scale the traces was a critical step in the time-lapse workflow. With sources of error controlled, the error-prone 3-component data processing steps can be carefully re-introduced in the future, with the goal of retaining the horizontal trace data while assessing the impacts of any resulting errors. This should further improve signal strength and allow for better preservation of S-wave data. Shear wave velocity is independent of fluid effects and provides additional information about shear modulus and therefore lithology (Hampson et al., 2006), helping to constrain seismic inversions for baseline reservoir

characterization. Converted shear wave reflection amplitudes provide more complete information about P-P and P-S mode conversion which will aid with future inversion attempts based off amplitude varying with angle (AVA) methods.

A major repeatability obstacle avoided by the time-lapse workflow was the seasonal variability in near-surface filtering affecting each shot gather. Baseline and monitor amplitudes were successfully balanced by deterministic deconvolution without need for further cross-equalization, save for shot-location-dependent high-cut filtering of the pre-stack gathers. CO_2 related differences in amplitude were preserved over most of the available frequency bands. Shot 13155 from Figure 4.9 showed the different degrees of attenuation suffered by the baseline and monitor data. While shot 13155 was originally high-cut filtered to 85Hz, decreasing the pre-whitening term in the deconvolution as low as 0.05% allowed for shot 13155's usable spectrum to be increased to 105Hz. This less conservative deconvolution operator design allows for higher resolution time-lapse results.

8.4 DAS time-lapse challenges

Individual DAS datasets, without high-cut filtering, achieved a high degree of visual similarity when compared with geophone and accelerometer datasets, particularly post-stack. This speaks to the high stacking power of DAS in general, and its value as a seismic sensor technology. However, time-lapse differences exhibited greater background residual amplitudes interfering with the detection of the CO_2 anomaly. Higher noise levels were apparent both in the time domain (Figure 6.9) and frequency domain (Figure 6.14) of the processed pre-stack data, some of which persisted through the stacks. The high-confidence geophone time-lapse VSP results in Chapter 5 were not successfully replicated with the DAS on Line 13. Line 7, with less-noisy baseline DAS data, did appear to show a weak CO_2 anomaly. However, it was not strong enough to reasonably call it above the detection threshold. With the strong results from the geophone Line 7 time-lapse and the relatively high SNR baseline DAS data for Line 7, the first clear detection of CO_2 by DAS is expected to occur on Line 7.

Compared to geophone processing, DAS data acquisition involved factors requiring additional data processing steps. Each of these factors were potential sources of error:

1. Differences in noise levels and noise types in raw DAS data.

2. Interrogator differences in optical signal emission, detection, and output data format (Lindsey et al., 2020).
3. Differences in output trace spacing.

These factors were addressed with several additional data preparation and processing steps:

1. Aggressive de-noising of raw data by a combination of f-k filter, median filter, and RMS trace normalization.
2. Integrating DAS amplitude units from radians/s to radians (in frequency domain), as needed.
3. Depth registration: Manually picking the DAS fiber bottom, assigning a bottom-depth to the lowest trace, and extrapolating trace depths based on interrogator spatial sampling rate.

Despite the QC process for the de-noising and depth registration steps, all three factors listed above remain possible sources of error in the DAS time-lapse results. Depth registration errors are the most likely to produce high frequency, coherent time-lapse residuals. Depth calibration between baseline and monitor data was performed iteratively by increments of 0.1% (1 mm) on the 1 m sampled monitor data. Shallow high-frequency residuals in the time-lapse differences may have been caused by remaining error in depth registration. A second, independent, validation of depth registration using DAS channel scalars computed from well logs (Mateeva and Zwartjes, 2017) would complement the existing process. This may help reduce time-lapse errors in the future. However, in Figures 6.14 and 6.16, coherent time-lapse residuals from depth registration did not appear to be a dominant source of error around the BBRS interval. In the CaMI.FRS setting, the injection interval was close enough to the bottom of the DAS fiber array that the accumulation of depth-registration errors did not significantly affect the time-lapse result. In a more general context of reservoir monitoring and leak detection, small depth registration differences between interrogators could easily mask a subtle time-lapse anomaly.

The integration of the Silixa DAS baseline data from units of radians/s to radians, in order to match the OptaSense data, was not an obvious source of error. Comparison in the time domain (Figure 6.9) and frequency domain (Figure 6.14) did not indicate any unexpected discrepancies in the data, beyond the general noise present in the DAS gathers. The DAS baseline and monitor shot spectra were very similar in frequency content to the

geophone data and showed the same variable near-surface filtering effects. Integration therefore was assumed to have correctly converted the DAS baseline data to be comparable to the monitor data. Overall differences in noise levels, particularly checkerboard noise and anomalous trace amplitudes, were likely the most significant cause of dissimilarity between baseline and monitor datasets.

The aggressive de-noising described in Chapter 6 appeared to remove much of the DAS instrument noise from the raw data (Figure 6.7). Yet, the difference between shot gathers showed remaining high amplitude time-lapse residuals (Figure 6.9). Instrument noise from either the interrogators or the fiber optic cable appeared to be the main barrier to success for the DAS time-lapse at the BBRS interval.

Time-lapse VSP monitoring with DAS arrays has proven successful at other CO_2 injection operations (Bacci et al., 2017; Michael et al., 2020; Pevzner et al., 2021). The main difference between those projects and the BBRS reservoir at CaMI.FRS is the higher porosities of those reservoirs and thus greater seismic response in the presence of CO_2 saturation. At CaMI.FRS, the time-lapse results achieved for a 33t CO_2 plume are pushing the limits of detectability for a small injection volume in a 10% porosity reservoir. While the CO_2 plume has been unequivocally detected with geophone data, a greater saturation and plume extent will be needed before the DAS data can detect and delineate the plume. Achieving a clear detection threshold on the DAS data will help set expectations between the capabilities of DAS and geophones in terms of reservoir monitoring and leak detection.

8.5 Improving DAS repeatability

The relative impact of interrogator design, depth registration errors, and instrument noise can be further evaluated by acquiring a new monitoring survey using the exact DAS interrogator unit from the 2021Mar1 survey. That OptaSense interrogator is jointly owned by CaMI and University of Calgary research groups and is available for repeated surveys. The same optical signal and instrumentation in the interrogator would be at play, with the same output trace spacing and data format. Trace depths would need to be registered, but the spatial sampling would be identical between surveys. The same trace would be chosen as the bottom or midpoint of the raw DAS record, eliminating another possible source of error. This would simplify the DAS data preparation outlined in Chapter 6.

The only differences then would be instrument noise during acquisition, such as checkerboard and common noise, and seasonal variability of near-surface filtering. Those noise types were present but were not particularly strong in the 2021Mar1 survey. While the ability to mitigate variable near-surface filtering has been demonstrated, these could be minimized as well. Ideally, such a repeated survey would be performed in winter 2022 under frozen-ground conditions similar to the 2021Mar1 survey. This should result in similarly low levels of near-surface filtering, and a direct comparison of most of the frequency band would be possible. Using 2021Mar1 as a baseline, a pronounced CO_2 anomaly may not be detectable in such a short 1-year time-lapse interval. However, if depth-registration and interrogator differences are the main obstacle to time-lapse analysis, using the 2021Mar1 survey as a baseline should produce a much cleaner time-lapse difference and act as proof of concept, returning low background time-lapse residuals and correspondingly low NRMS values. If unsuccessful, a more sophisticated de-noising process could be tested by modeling and removing noise by adaptive subtraction (Olofsson and Martinez, 2017) or with trained convolutional neural networks (Zhao et al., 2022). Testing and comparison of different DAS interrogators is an important area of research area at CaMI.FRS. A repeated survey, under nearly identical conditions to the 2021Mar1 survey, will act as a good control dataset for both time-lapse studies such as this, and a broader DAS interrogator comparison project.

8.6 Line 13 DAS baseline substitution

Due to high noise levels in the 2017May DAS baseline, it may be necessary to substitute the 2021Mar1 survey as the main baseline for Line 13, and likely Line 15 as well. The coverage of the DAS data allows it to sample a much wider range of reflection CDP offsets. As the CO_2 plume grows, DAS will become the principal VSP monitoring technology in future years at CaMI.FRS. Therefore, the presence of the 33 t, ~50 m wide CO_2 plume in the 2021Mar1 DAS dataset will not significantly affect its ability to act as a baseline survey. Combining the Obs 1 and Obs 2 DAS data will allow for the monitoring range to be further extended, while improving fold across much of the subsurface around the injection well.

CHAPTER 9 - CONCLUSION

9.1 Time-lapse VSP processing

A time-lapse compliant 1-C VSP workflow was developed to detect the subtle effects of a small 33 t CO_2 plume in a 300 m depth sandstone reservoir of 10% porosity. 1D and 2D forward modeling set expectations of the plume's effects on the seismic data. Modeling indicated that the CO_2 plume should be detectable with existing 2021 geophone data, with sufficient care and consistency in the processing. Of the numerous VSPs acquired at the CaMI Field Research Station between 2017 and 2021, time-lapse datasets from monitoring lines 7, 13, and 15 had been acquired most frequently. With highly repeatable acquisition using nearly identical shot locations and the same vibroseis source, the principal cause of dissimilarity between baseline and monitor data was seasonal variability of surface conditions and near-surface filtering. This was mitigated by relying on deterministic deconvolution to properly scale trace amplitudes, followed by high-cut filters to remove baseline and monitor spectral differences for each source location. The reliable processing workflow produced directly comparable baseline and monitor amplitudes and high-confidence time-lapse results without the application of shaping filters. The detected CO_2 plume matched expectations from forward modeling. The 1-C workflow was directly applicable to straight fiber DAS data. The simple, high-confidence geophone workflow can now serve as a basis to develop a more complex time-lapse compliant VSP workflow at CaMI.FRS, incorporating 3-C data, helically-wound fiber DAS data, and depth migration.

9.2 Detection threshold

The detection of the 33 t CO_2 plume with time-lapse walk-away VSP data, on multiple geophone datasets across two of the three standard monitoring lines, confidently establishes a detection threshold between 15 t and 33 t of injected CO_2. A combination of CO_2 saturation and lateral plume extent, the detection threshold was determined by interpreting reflection amplitude differences in the baseline and monitor pre-stack and post-stack data. This 33 t detection threshold in a 10% sandstone reservoir indicates that in reservoirs of higher porosity, even smaller CO_2 volumes could be detectable at shallow and intermediate depths. The detection of this known CO_2 plume proved challenging, requiring a customized workflow and cautious processing even with highly repeatable, high frequency data with a 10 Hz – 150 Hz bandwidth. Successful detection and delineation of

the plume with VSP data will allow for expanded analysis of the various active and passive monitoring technologies employed at the CaMI.FRS.

The detection threshold for DAS data has not yet been determined, due principally to higher levels of noise present in the raw baseline data. An ambiguous time-lapse residual at the BBRS interval observed on Line 7 data was not evident on Line 13 which had a lower quality baseline survey. DAS time-lapse results required depth registration precision on the order of 0.1% or better when extrapolating trace depths using the output trace spacing from the interrogator unit. Depth registration errors were also minimized by comparison with accelerometer data with known receiver depths.

Reservoir monitoring and early leak detection are key components of MMV requirements for geological CO_2 sequestration operations. Detection of unknown leaks from a CO_2 storage reservoir with VSPs is not a trivial matter, particularly with shallow broadband data that is highly sensitive to variability in surface and near-surface conditions. The results from this study demonstrate that for VSP monitoring of future CO_2 storage projects, acquisition parameters should not only be designed for direct reservoir monitoring of a typically high-porosity storage reservoir. Seismic arrays and processing workflows should also account for detection of unexpected leaks into shallower formations causing subtle amplitude effects outside the reservoir interval, as simulated by the field experiment at CaMI.FRS. The ability to detect CO_2 leaks orders of magnitude smaller than typical Mt/year injection rates helps demonstrate containment and will improve confidence in MMV capabilities as the CCS industry expands. These findings are relevant to future CO_2 permanent-storage and EOR projects, whether at deep, intermediate, or shallow depths.

9.3 Future work at CaMI.FRS

9.3.1 Walk-away VSP monitoring

- New higher-frequency time-lapse results can be produced for Line 13, 7, and 15 data, as demonstrated with the 2021Mar1-2017May time-lapse from Chapter 7. This will require additional testing of deconvolution parameters and new sets of high-cut filters to optimize the high-frequency bandwidth-matching.
- While monitor surveys should still be acquired opportunistically throughout the year, frozen-conditions will minimize the seasonal variability of near-surface filtering and simplify the high-cut filtering process, as with the 2021Mar1 data.

- The CO_2 had evidently not progressed south-west far beyond the Obs 2 well by 2019. On Line 13, this will allow for some of the highly-attenuated south-western baseline shots from 2017May to be replaced with higher quality 2019 equivalents. In addition, 10 m spacing from 2019 could be restored to at least the south-west portion of Line 13. This hybrid baseline for Line 13 should prove more useful as the plume grows.
- The 2017May baseline was shot with 20m shot spacing yet still provided adequate fold to detect the CO_2, when compared with Line 7's 10 m spacing. Monitor acquisition should continue with 10 m shot spacing. However, a resolution test could be performed by later decimating the datasets to increase shot spacing to 30 m or 40 m. This would determine how sparse the spacing could get before sacrificing resolution and detection ability. This analysis would inform minimum spacing requirements for permanent source monitoring.
- The error-prone processing steps of 3-C rotation and time-invariant rotation can now be re-introduced to the VSP workflow and evaluated. Doing so would allow for shear-wave data to be more easily processed.
- The VSP forward model can be updated from an acoustic to an elastic model. AVO effects could be better characterized in the time-lapse datasets, and a normalization process for asymmetric fold distribution could be developed to help with VSP interpretation and inversion.
- Primary and converted-wave S-waves could be processed for time-lapse purposes. This could first be achieved with 3-C geophone data prior to an attempt with DAS. The 3-C 2018Sep MEMS accelerometer data could be used to calibrate any DAS S-wave processing attempt.
- Pre-stack inversion of P-wave and S-wave data, and subsequent time-lapse would help characterize the reservoir interval and the CO_2 plume with the relatively high resolution of time-lapse data. Success with geophones could then be extended to the 2018Sep MEMS accelerometer survey and eventually to DAS. The 2018Sep MEMS accelerometer VSP data would provide a very high SNR inversion result, with extensive coverage, against which to verify geophone and DAS inversions.

- Acoustic and elastic baseline and monitor models derived from these field data results could replace synthetic reservoir models developed by Macquet et al. (2019) which are currently used for FWI research by Amundaray and Innanen (2021). Time-lapse VSP monitoring results achieved through conventional processing and shot-specific filtering can act as a ground-truth for ongoing research into Full Waveform Inversion (FWI) of CaMI.FRS VSP field data (Keating et al., 2021b). Near-surface velocities and filtering pose additional challenge for FWI (Keating et al., 2021a). The downgoing arrivals recorded by the geophone array contains the highest-SNR information about near-surface filtering which may aid future FWI models by constraining bandwidth to field data levels.
- As described in Chapter 8.3, a repeat of the 2021Mar1 survey using the U of C OptaSense interrogator should be performed. This should eliminate depth registration errors and establish a best-case repeatability scenario for DAS datasets.
- The DAS fibers in the two observation wells extend below the reservoir by 30 m – 40 m. DAS could be used to directly detect travel-time delays and attenuation in the downgoing arrivals, expected to be on the order of 0.1 ms to 0.2 ms. This would require error-free depth registration to be achieved, most likely by using the U of C OptaSense interrogator repeatedly. The 1 ms sampling of the 2021Mar1 Optasense survey may be sufficient as a baseline. Finer time-sampling such as 0.5 ms or lower may be necessary, however. A comparison between travel-time delay around the Obs 2 and Obs 1 wells could be performed.
- The Obs 1 straight-fiber DAS data can be combined with Obs 2 to double the fold across much of Line 13. This will increase the stacking power, increase the lateral coverage, and speed up the detection of CO_2 on Line 13.

9.3.2 3D VSP monitoring

- A 3D VSP survey was acquired in 2021May as result of a larger 3D seismic survey acquired with Explor. A high resolution 3D volume could be generated from the borehole data and compared with the 3D surface data from that survey.

This should allow for a high-resolution 3D seismic characterization of the injection interval.

- A 3D VSP time-lapse could be attempted using the extensive 2018Sep walk-away and walk-around VSP data. A selection of the vibe shot points from the 2021May 3D could be repeated for a dense 3D VSP time-lapse, e.g. offsets to 200 m or 250 m. This could then be expanded as the plume grows.
- Borehole data from Vibroseis and pinpoint sources from the 2021May 3D survey scan be compared for pre-stack and post-stack SNR and frequency content.

9.3.3 Permanent source monitoring

- Now that the CO_2 has been detected SW of Obs 2, a shot-gather time-lapse could be performed using either the 3P Technology Corp. impulsive source (Lawton et al., 2020), or with an orbital vibrator source (Spackman, 2019). This would test the ability to detect CO_2 saturation changes with a single broadband shot from a permanent or semi-permanent source.
- Primary S-wave data from a source mounted on the helical pile could be compared to the S-wave data from a standard Vibroseis shot and from shear surface sources previously used at CaMI.FRS. The signal strength of S-wave energy generated by the helical pile could be determined.
- With CO_2 now detected south-west of Obs 2, geophone borehole data could be acquired during injection, from a source mounted on the helical pile. This type of data has been previously acquired on the surface with the IVI Envirovibe (Innanen et al., 2019). Using either 3P Technology's impulsive source (Lawton et al., 2020), or an orbital vibrator source (Spackman, 2019), that experiment could be adapted to the helical pile with which frequency content up to 200 Hz could be obtained.
- In order for the high frequency synthetic seismogram to match the high frequency Phase 2 and 3 data seen in Figure 7.5, a more finely detailed drift-correction was performed on the well logs. The previous drift correction had been a coarser best-fit approach which was adequate for the lower frequency vibe data. The updated drift-correction could be applied to generate new velocity

and density models for the VSP forward model in Chapter 3. This would allow for forward modeling of broader-band shot gathers, such as from the helical pile. Doing so would set expectations for maximum possible resolution of the BBRS interval, and the overlying and underlying formations.

- Broader-band data from a source on the helical pile may aid the interpretation of borehole ERT data at the FRS, which has a fine spatial resolution around the well that decays below seismic resolution at farther offsets. VSP shot gathers from the helical pile may help bridge the ERT - VSP resolution gap around the geophysics observation well.

9.3.4 Surface seismic monitoring

- With confident VSP results achieved on Line 13, 2D surface seismic monitoring along Line 13 is the next logical step. As with VSP data, 2D monitoring data using surface geophone arrays has been recorded over the years. Compared to 3D data, 2D surface data offers a low level of complexity to allow for a time-lapse compliant processing workflow to be carefully designed. This will help set expectations for 3D surface seismic monitoring capability at the FRS, and inform 3D time-lapse processing.
- Simultaneously acquired 2D surface and 2D walk-away VSP datasets exist. The downgoing arrivals of the VSP data can be used to inform 2D processing and deconvolution in order to optimize the 2D surface time-lapse. As discussed in Chapter 7, those downgoing arrivals contain information about not only the subsurface filtering effects, but also the variable and static near-surface filtering effects of each shot location. For surface geophones near those shot locations, the known near-surface filtering effects may also be accounted for. Speculatively, it should be possible to incorporate these surface-consistent and "near-surface consistent" filtering effects into the 2D seismic deconvolution process. If successful, this process could then be expanded to the 3D VSP and 3D surface seismic data from May, 2021.

REFERENCES

Al Hosni, M., Caspari, E., Pevzner, R., Daley, T.M., Gurevich, B., 2016, Case History: Using time-lapse vertical seismic profiling data to constrain velocity–saturation relations: the Frio brine pilot CO_2 injection: Geophysical Prospecting, **64**, 987–1000.

Al Mutlaq, M., and Margrave, G., 2011, Short note: Shaping / Matching filters: *CREWES Research Report*, **23**, 2, 11.

Al Jabri, 2011, Land seismic repeatability prediction from near-surface investigations at Naylor field, Otway: Ph.D. Thesis, Curtin University of Technology.

Amundaray, N., and Innanen, K. A., 2021, Time-lapse elastic full waveform inversion of CO_2 injection at CaMI FRS using VSP: a feasibility study: *CREWES Research Report*, **33**, 1, 17.

Bacci, V., O'Brien, S., Frank, J., and Anderson, M., 2017, Using a walk-away DAS time-lapse VSP for CO_2 plume monitoring at the Quest CCS project: CSEG Recorder, **42**, no. 3, 18-22.

Bachu, S., 2003, Screening and ranking of sedimentary basins for sequestration of CO_2 in geological media in response to climate change: Environmental Geology, **44**, 277-289.

Bakku, S., 2015, Fracture characterization from seismic measurements in a borehole: Ph.D. Thesis, Massachusetts Institute of Technology.

Brie, A., Pampuri, F., Marsala, A.F. & Meazza, O. 1995, Shear sonic interpretation in gas-bearing sands. SPE Annual Technical Conference: Society of Petroleum Engineers, **30595**, 701–710.

Chadwick, R., Marchant, B., Williams, G., 2014, CO_2 storage monitoring: leakage detection and measurement in subsurface volumes from 3D seismic data at Sleipner: Energy Procedia, **63**, 4224-4239.

Cheng, A., Huang, L., and Rutledge, K., 2010, Time-lapse VSP data processing for monitoring CO_2 injection: The Leading Edge, **29**, 196-199.

Daley, T., Miller, D., Dodds, K., Cook, P., and Freifeld, B., 2016, Field testing of modular borehole monitoring with simultaneous distributed acoustic sensing and geophone vertical seismic profiles at Citronelle, Alabama: Geophysical Prospecting, **64**, 1318-1334.

Dongas, J., 2016, Development and characterization of a geostatic model for monitoring shallow CO_2 injection: M.Sc. Thesis, University of Calgary.

Gassmann, F., Maggiorini, M., Städler, E. & Winkler, W. 1951. Über die Elastizität poröser Medien. Verteljahrsschrift der Naturforschenden Gesellschaft in Zurich, **96**, 1–23.

Gordon, A., 2019, Processing of DAS and geophone VSP data from the CaMI Field Research Station: M.Sc. Thesis, University of Calgary.

Gutierrez, M., Katsuki, D., Almrabat, A., 2012, Effects of CO_2 injection on the seismic velocity of sandstone saturated with saline water: International Journal of Geosciences, 2012, **3**, 908-917.

Hall, K., Lawton, D., Innanen, K., 2021, Fiber trace registration by cross-correlation – can we successfully predict helically wound fiber pitch angle from recorded data?: CREWES Research Report, **33**, 14. 18.

Hartog, A., 2017, An introduction to distributed optical fiber sensors: CRC Press.

Hargreaves, N.D., and Calvert, A.J., 1991, Inverse Q filtering by fourier transform: Geophysics, **56**, 519-527.

Hinds, R.C., Anderson, N.L., and Kuzmiski, R.D., 1996, VSP Interpretive Processing: Theory and Practice: Society of Exploration Geophysics.

Innanen, K., Nakata, R., Kato, A., Lawton, D., Bertram, M., 2019, Seismic evidence for transient elastic bracing in microbubble water and CO_2 injection zones: Paper presented at the SEG International Exposition and Annual Meeting, San Antonio, Texas, USA, September 2019.

International Energy Agency, 2021, Energy technology perspectives 2020: Special report on Carbon Capture Utilisation and Storage.

International Panel on Climate Change, 2005, IPCC Special Report on Carbon Dioxide Capture and Storage. Prepared by Working Group III of the Intergovernmental Panel on Climate Change. (B. Metz, O. Davidson, H. de Coninck, M. Loos, & L. Meyer, Eds.) Cambridge, United Kingdom and New York, NY, USA: Cambridge University Press.

IPCC, 2014, Summary for Policymakers. Climate Change 2014: Synthesis Report. Contribution of Working Groups I, II and III to the Fifth Assessment Report of the Intergovernmental Panel on Climate Change.

Keating, S., Eaid, M., and Innanen, K. A., 2021a, Effective sources: removing the near surface from the VSP FWI problem: *CREWES Research Report*, **33**, 27, 10.

Keating, S., Eaid, M., and Innanen, K. A., 2021b, Full waveform inversion of VSP accelerometer data from the CaMI field site: *CREWES Research Report*, **33**, 28, 8.

Kolkman-Quinn, B., and Lawton, D. C., 2020, Time-lapse VSP results from the CaMI Field Research Station: CREWES Research Report, **32**, 34, 14.

Kragh, E., and Christie, P., 2002, Seismic repeatability, normalized rms, and predictability: The Leading Edge, **21**, 640-647.

Lawton, D., Bertram, M., Hunter, T., Maidment, G., and Kolkman-Quinn, B., 2020, Squid: An innovative new ground-coupled electric seismic source for seismic monitoring: *CREWES Research Report*, **32**, 37, 11.

Lawton, D., Bertram, M., Saeedfar, A., Macquet, M., Hall, K., Bertram, K., Innanen, K., Isaac, H., 2017, DAS and seismic installations at the CaMI Field Research Station, Newell County, Alberta: CREWES Research Report, **29**, 51, 10.

Lawton, D., Gordon, A., Bidikhova, S., Hall, K., and Bertram, M., 2019, Update on DAS and geophone VSP surveys at the CaMI Field Research Station, Newell County, Alberta: CREWES Research Report, **31**, 39, 14.

Li, M., Wang, H., Tao, G., 2015, Current and future applications of distributed acoustic sensing as a new reservoir geophysics tool: The Open Petroleum Engineering Journal, 2015, **8**, 272-281.

Lindsey, N., Rademacher, H., Ajo-Franklin, J., 2020, On the broadband instrument response of fiber-optic DAS arrays: Journal of Geophysical Research: Solid Earth, **125**, e2019JB018145.

Luo, Q., Wang, Y., Wang, Y., Wang, Y., Chen, M., Zheng, Y., Wu, S., Chang, X., Zeng, R., 2018, Time-lapse VSP monitoring for CO_2 injection: A case study in Ordos, China: International Journal of Greenhouse Gas Control, **75**, 41-51.

Macquet, M., Lawton, D., 2017, Reservoir simulations and feasibility study for seismic monitoring at CaMI.FRS: CREWES Research Report, **29**, 56.1-56.26.

Macquet, M., Lawton, D., Kolkman-Quinn, B., 2022, Carbon Management Canada CaMI Field Research Station: Advancing Monitoring Technologies for CCS: EAGE Geotech 2022 abstract.

Macquet, M., Lawton, D., Rippe, D., Schmidt-Hattenberger, C., 2021, Semi-continuous electrical resistivity tomography monitoring for CO_2 injection at the CaMI Field Research Station, Newell County, Alberta, Canada: First International Meeting for Applied Geoscience and Energy Conference Abstract.

Macquet, M., Lawton, D., Saeedfar, A., Osadetz, K., 2019, A feasibility study for detection thresholds of CO_2 at shallow depths at the CaMI Field Research Station, Newell County, Alberta, Canada: Petroleum Geoscience, **25**, 509-518.

Mateeva, A., Lopez, J., Potters, H., Mestayer, J., Cox, B., Kiyaschchenko, D., Wills, P., Grandi, S., Hornman, K., Kuvshinov, B., Berlang, W., Yang, Z., Detomo, R., 2014, Distributed acoustic sensing for reservoir monitoring with vertical seismic profiling: Geophysical Prospecting, **62**, 679-692.

Mateeva, A., Zwartjes, P., 2017, Depth calibration of DAS VSP channels: a new data-driven method: 79th EAGE Conference and Exhibition Abstract.

Michael, K., Arsham, A., Ricard, L., Myers, M., Tertyshnikovm K., Pevzner, R., Strand, J., Hortle, A., Stalker, L., Pervukhina, M., Harris, B., Feitz, A., Pejcic, B., Larcher, A., Rachakonda, P., Freifeld, B., Woitt, M., Langhi, L., Dance, T., Myers, J., Roberts, J., Saygin, E., White, C., Seyyedi, M., 2020, A controlled CO_2 release experiment in a fault zone at the In-Situ Laboratory in Western Australia: International Journal of Greenhouse Gas Control, **99**, 103100.

Olofsson, B., and Martinez, A., 2017, Validation of DAS integrity against standard geophones – DAS field test at Aquistore site: The Leading Edge, **36**, 981-986.

Pevzner, R., Isaenkov, R., Yavuz, S., Yurikov, A., Tertyshnikov, K., Shashkin, P., Gurevich, B., Correa, J., Glubokovskikh, S., Wood, T., Freifeld, B., Barraclough, P., 2021, Seismic monitoring of a small CO_2 injection using a multi-well DAS array: Operations and initial results of stage 3 of the CO2CRC Otway Project: International Journal of Greenhouse Gas Control, **110**, 103437.

Pevzner, R., Urosevic, M., Tertyshnikov, K., Al Nasser, H., Caspari, E., Correa, J., Daley, T., Dance, T., Freifeld, B., Glubokovskikh, S., Greenwood, A., Kepic, A., Popik, D., Popik, S., Raab, M., Robertson, M., Shulakova, V., Singh, R., Watson, M., Yavuz, S., Ziramov, S., Gurevich, B., 2020, Active Surface and borehole seismic monitoring of a small supercritical CO_2 injection into the

subsurface: experience from the CO2CRC Otway Project: Active Geophysical Monitoring (Second Edition), 597-522.

Russel, B., Hampson, D., Bankhead, B., 2006, An inversion primer: CSEG Recorder, **31**, Special edition.

Spackman, T., 2019, Novel orbital seismic sources at a CO_2 storage monitoring site, Newell County, Alberta: M.Sc. Thesis, University of Calgary.

Wang, Y., 2002, A stable and efficient approach of inverse Q filtering: Geophysics, **67**, 657-663.

Zhao, Y., Li, Y., Wu, N., 2022, Data augmentation and its application in distributed acoustic sensing data denoising: Geophysical Journal International, **228**, 119-133.

Liu, Z., Deng, Z., Davis, S., Giron, C., Ciais, P., 2022, Monitoring global carbon emissions in 2021: Nature Reviews Earth & Environment, Comment